EPFL

High sensitivity, incoherent differential imaging

Chiara BONATI

■ École
polytechnique
fédérale
de Lausanne

2022

Acknowledgements

Abstract

Microscopic visualisation of optically transparent samples has been a topic of great interest for several decades. While mostly invisible to standard brightfield microscopy, features such as density or chemical composition can influence the optical phase of transmitted light, and phase contrast can reveal these structures. A multitude of methods of phase contrast have been developed, which can be broadly categorised as either interferometric or non-interferometric, based on the type of interaction and coherence properties of the light used, with some exceptions. In this work, the attention is focused on the use of incoherent light to generate phase contrast, in particular via Differential Phase Contrast (DPC). The choice of incoherent sources brings a series of benefits such as the absence of distortions like speckle patterns and ringing patterns, as well as increased spatial resolution, and a simpler setup that can be used for in-vivo biological applications. Moreover, DPC allows precise reconstruction of quantitative phase maps of the imaged samples. On the other hand, coherent-based techniques typically demonstrate superior performance in terms of phase sensitivity.

The first part of the work presented here consists in a quantitative analysis of the phase sensitivity of DPC and investigates the influence of optical parameters and sample characteristics. Employing both simulations and experiments, a relation between numerical aperture and phase sensitivity is demonstrated, and the concept of spectral matching is introduced to enhance sample-specific contrast. The methods used can be generalised to any DPC setup, and allow a-priori investigation of the phase sensitivity of a DPC microscope at the design stage rather than through later experimental testing.

Nevertheless, a comparison between the best sensitivity that can be achieved in DPC and state-of-the-art interferometric techniques, shows that despite careful optimisation, it is not possible to reach comparable single-shot performances. In this thesis, it is demonstrated that the reason for this limitation lies in the presence of a strong background in DPC images, which degrades the dynamic range of this technique. Typically, DPC images are obtained with mirrored illuminations, for which the background is identical and the phase term switches in sign. The difference between these pairs of images is computed digitally, but this does not improve the limited dynamic range.

Here, a lock-in DPC technique is proposed as a solution to this issue: instead of separately sampling different pairs of illumination states, lock-in DPC directly demodulates the amplitude of the phase signal when the illumination is switched, and the background is never encoded. This is enabled by periodical switching of mirrored sources coupled with the use of a smart pixel detector, the so-called "lock-in camera". Part of this work is dedicated to the

theoretical description of this new method, as well as the analysis of the expected benefit over standard DPC. Experiments are also described, that demonstrate a factor of 8 improvement in single-shot sensitivity compared to standard DPC.

DPC is not the only imaging technique to suffer from high intensity background: it is easy to see how the use of a lock-in camera for differential imaging can be generalised to any situation where weak, periodic modulations can be induced over a strong background. In the last part of this work, an example of this concept of generalised differential imaging is presented with lock-in Shifted Excitation Raman Spectroscopy (SERDS). SERDS is an established Raman spectroscopy technique, that takes advantage of the Raman emission spectrum being relative to the excitation wavelength to remove unwanted fluorescence emission. Two spectra with slightly shifted excitation wavelengths are measured, their difference is computed, and the fluorescence is thus digitally removed. The parallel with DPC is immediately apparent. Both simulations and experiments are used to demonstrate the advantage of analog demodulation of the differential spectrum compared to digital computation.

Keywords: Phase imaging, phase contrast, lock-in, demodulation, microscopy, imaging, Raman, spectroscopy.

Sommario

La microscopia di campioni trasparenti nello spettro visibile è un argomento di grande interesse da diversi decenni. Nonostante siano quasi completamente invisibili nella classica microscopia in campo chiaro, caratteristiche come la densità o la composizione chimica possono influire sulla fase ottica della luce trasmessa dal campione, e il contrast di fase può rivelare queste strutture.

Diversi metodi di contrasto di fase sono stati sviluppati, e possono essere generalmente categorizzati come interferometrici o non-interferometrici a seconda del tipo di interazione e del grado di coerenza della sorgente utilizzata, con alcune eccezioni. In questo lavoro l'attenzione è posta sull'uso di sorgenti incoerenti per generare contrasto di fase, in particolare attraverso il contrasto di fase differenziale (Differential Phase Contrast, DPC). La scelta di sorgenti incoerenti porta una serie di benefici, come l'assenza di distorsioni quali lo "speckle pattern" e i "ringing patterns", oltre a una migliore risoluzione spaziale, una configurazione più semplice, e la possibilità di sviluppare applicazioni biologiche in-vivo. Inoltre, il DPC permette di ricostruire una precisa mappa quantitativa della fase del campione sotto osservazione. D'altro canto, le tecniche basate su illuminazione coerente presentano una performance superiore in termini di sensibilità.

La prima parte del lavoro presentato qui consiste in una analisi quantitativa della sensibilità del DPC, che coinvolge l'influenza di parametri ottici e delle caratteristiche del campione. Tramite simulazioni ed esperimenti, si dimostra una relazione tra l'apertura numerica e la sensibilità alla fase ottica, ed è introdotto il concetto di sovrapposizione dello spettro per ottimizzare il contrasto per uno specifico campione. I metodi usati possono essere generalizzati per qualunque configurazione DPC, e dunque permettono un'analisi a-priori della sensibilità del DPC già al momento della progettazione del sistema, invece che dopo la costruzione tramite caratterizzazione sperimentale.

Nonostante ciò, un confronto tra la migliore sensibilità che può essere raggiunta con il DPC e con le tecniche interferometriche allo stato dell'arte, mostra che anche dopo aver accuratamente ottimizzato il sistema non è possibile raggiungere una performance comparabile in una singola misura. In questa tesi viene dimostrato che il motivo di questa limitazione è la presenza di un forte fondo nelle immagini DPC, che degrada la gamma dinamica di questa tecnica. Tipicamente, le immagini DPC sono ottenute con illuminazioni specchiate per le quali il fondo è identico e il contributo della fase cambia semplicemente di segno. La differenza tra queste coppie di immagini viene poi calcolata digitalmente, ma questo non migliora la gamma dinamica.

Sommario

Si propone quindi il lock-in DPC come soluzione a questo problema: invece di campionare separatamente i diversi stati di illuminazione, il lock-in DPC demodula direttamente l'ampiezza del segnale della fase quando l'illuminazione cambia, e il fondo non viene mai registrato. Per fare questo, le sorgenti sono accese alternatamente, e la misura viene fatta con un detettore con pixel intelligenti, la cosiddetta "lock-in camera". Parte di questo lavoro è dedicata alla descrizione teorica di questo nuovo metodo, e all'analisi dei benifici attesi rispetto al DPC classico. Viene proposta anche una sezione sperimentale, che dimostra un miglioramento della sensibilità di un fattore 8, in una singola misura, rispetto al DPC classico.

Il DPC non è l'unica tecnica di microscopia penalizzata da un fondo ad alta intensità: la lock-in camera può essere dunque utilizzata in generale per qualunque metodo di misura differenziale, dove un debole segnale periodico può essere indotto sopra un forte fondo luminoso. Nell'ultima parte di questo lavoro, viene proposto un esempio di questo concetto di misura differenziale generalizzata, la spettroscopia Raman con lunghezza d'onda d'eccitazione spostata (Shifted Excitation Raman Spectroscopy, SERDS). La SERDS è una tecnica di spettroscopia Raman già comunemente utilizzata, che trae vantaggio dal fatto che lo spettro Raman emesso dal campione è relativo alla lunghezza d'onda della luce usata per l'eccitazione, per rimuovere il fondo di fluorescenza. Due spettri ottenuti con lunghezza d'onda d'eccitazione diversa vengono misurati, e siccome la fluorescenza è indipendente dalla lunghezza d'onda, nel calcolare la differenza tra i due spettri viene eliminata digitalmente. Il parallelo con il DPC è immediatamente chiaro. Con simulazioni ed esperimenti, viene dimostrato il vantaggio dato dalla demodulazione analogica dello spettro differenziale in confronto al calcolo digitale.

Parole chiave: Imaging di fase, contrasto di fase, lock-in, demodulazione, microscopia, imaging, Raman, spettroscopia.

Contents

Contents

Acronyms

AFM Atomic Force Microscopy

ATF Amplitude Transfer Function

BFP Back Focal Plane

CNR Contrast to Noise Ratio

DPC Differential Phase Contrast

HDR High Dynamic Range

IP Image Plane

KE Knife Edge mirror

LED Light Emitting Diode

NA Numerical Aperture

OPD Optical Path Difference

OPL Optical Path Length

OTF Optical Transfer Function

RDS Raman Difference Spectroscopy

ROI Region of Interest

SERDS Shifted Excitation Raman Difference Spectroscopy

SNR Signal to Noise Ratio

USAF U.S. Air Force

List of Figures

List of Figures

List of Tables

1 Introduction

1.1 Motivation and structure

Real time and three dimensional imaging of biological phenomena has been a topic of great interest in the past decades. The ability to observe dynamic changes within an in-vitro or in-vivo sample can provide valuable insight about the mechanisms that govern different functions, and how they are affected by diseases. Moreover, using light as a probe does not require direct contact with the region of interest, and in recent years an increasing number of label-free methods have been developed, meaning that minimal to no interference takes place during observation. Several challenges are associated with biological imaging, both on a general level and on an application-specific level. For example, events related to neuronal activity can be quite fast, in the order of milliseconds [1], requiring frame rates in the order of kHz. Another issue is the magnitude of changes that can be detected, which can be quantified with the sensitivity. In general, an appropriate technique to observe dynamic biological events should be:

- **Fast** enough to accurately follow changes;

- **Specific** to the quantity of interest;

- **Sensitive** to the smallest changes expected;

- **Bit-efficient**, allocating the maximum amount of data to encode the quantity of interest over irrelevant information.

A group of techniques that can be fast and highly specific are differential imaging methods. The idea is to use a certain characteristic of the source light as a probe, and to observe how the detected signal changes following changes in the source. Only certain features of the sample will respond to these changes, allowing to differentiate them from what is considered as background. Of course, it is necessary to choose the correct type of light modulation, such that only the features of interest give rise to changes in the detected signal. Differential imaging methods can be based, for example, on wavelength modulation (Shifted Excitation Raman Difference Spectroscopy (SERDS)), angular modulation (Differential Phase Contrast (DPC)) or polarisation (differential polarisation imaging). In many instances though, these techniques

1

can only be either sensitive, or bit-efficient. This is due to the fact that the specificity of differential imaging arises from the temporal differentiation between parts of the signal that change according to the excitation, and parts of the signal that do not, meaning that both elements are being recorded. Typically, two or more frames are collected at different stages of the illumination modulation, and their difference is computed digitally off-line. This means that part of the bit-depth available has to be spent to encode multiple times the portion of signal that is considered as background, and is subsequently removed. In many instances, the actual signal of interest takes up a modest portion of the total collected power, severely impacting the Signal to Noise Ratio (SNR).

The most effective way to improve the SNR is typically to average multiple frames. On the other hand, this means that significantly more data needs to be recorded and stored, especially if recording for a long time, or over large volumes. It becomes clear how, optimising bit-efficiency is fundamental in order to obtain high sensitivity without compromising the actual bit-rate or data storage limits of an experiment setup. In this thesis, I explore how analog lock-in techniques can be used to perform differential imaging in a bit-efficient way, meaning that only the relevant modulated part of the signal is actually encoded and detected. This method is enabled by the use of a lock-in camera, which features pixel-level circuitry to perform lock-in demodulation. In particular, two applications are demonstrated: lock-in Differential Phase Contrast (DPC), and lock-in Raman Difference Spectroscopy (RDS).

DPC is a phase imaging technique that employs multiple asymmetric sources of illumination to generate phase contrast in intensity images. This is particularly of interest for microscopic imaging of transparent samples: numerous ex-vivo biological applications have been demonstrated over the years [2–10]. Moreover, its use has been proven in applications such as in-vivo imaging of the human retina [11], where interferometric techniques have limited capabilities in detecting structures with low reflectivity [12]. On the other hand, standard DPC suffers from low sensitivity, and for this reason it has not been applied in scenarios such as the detection of action potentials. Chapter 2 describes the basics of phase imaging and DPC, from the theory of image formation to the methods of reconstruction. Chapter 3 is dedicated to the study of the parameters affecting sensitivity of DPC both theoretically and validated by experiments. In Chapter 4, lock-in DPC is presented, both from a theoretical and experimental point of view.

Raman spectroscopy is a widely used spectroscopic technique that enables label-free detection of chemicals as well as their quantification. One well known challenge in Raman spectroscopy is the presence of a strong fluorescence background when visible light is used as the excitation wavelength [13, 14], particularly when compared to typical Raman efficiency, that can be as low as 10^{-8} of the incident excitation power [15, 16]. Fluorescence light can be emitted by the molecules of interest themselves, as well as the surrounding medium, and is particularly problematic for biological investigation [13], which is also one of the main drivers for research and further development of the technique [17]. One way to reduce the fluorescence signal is to use two or more wavelengths of excitation to produce multiple spectra. The fluorescence component is largely independent on the wavelength of excitation. Computing the difference between spectra generated by two closely spaced excitation wavelengths

generates background free differential spectra that can be analysed more effectively [18, 19]. Chapter 5 is dedicated to lock-in RDS, and presents theory and experiments showing the expected improvements.

1.2   Contributions

The results presented in Chapter 3 have been published in C. Bonati, T. Laforest, M. Kunzi, and C. Moser, "Phase sensitivity in differential phase contrast microscopy: limits and strategies to improve it," *Opt. Express*, vol. 28, pp. 33767-33783 (2020). For this study, I designed and built the optical setup, and carried out all the experiments and analysis. I designed the photolithography masks for the U.S. Air Force (USAF) targets used for some of the experiments, and I carried out all the processes for their fabrication. I also adapted the DPC open source codes from L. Tian, L. Waller, Quantitative differential phase contrast imaging in an LED array microscope, Opt. Express 23, 11394-11403 (2015) for the sensitivity estimation. I am the main contributor of the manuscript.

The paper C. Bonati, D. Loterie, T. Laforest, and C. Moser, "Lock-in incoherent differential phase contrast imaging," *Photon. Res.*, vol. 10, 237-247, (2022) contains all the results described in Chapter 4. For this study, I designed and built the setup, as well as managed the integration of the lock-in camera within the system. I programmed the whole hardware control and signals for triggering of the different parts of the system. I also carried out all the experiments and analysis. I am the main contributor of this manuscript.

Finally, the results presented in Chapter 5 are currently being prepared for submission. I supervised and assisted two students in the design and development of the Raman setup. I then carried out all the experiments and analysis, and I am writing the manuscript for submission.

2 Phase imaging: from the basics to Differential Phase Contrast

Seeing beyond the limits of human vision has long been a goal in the optics community, and microscopy addresses the objective of looking at what is too small for us to see. In the broader sense, this can be reduced to the question of how to effectively magnify objects of interest. This simplification does not describe the multitude of characteristics of light-matter interaction that we could magnify, such as absorption, phase, polarization, to name a few. Each of these characteristics tell us something about the nature of the sample, and different techniques are used to explore them. This chapter discusses the theory and instrumentation used to investigate optical phase, and how this can be related to the physical properties of a sample.

2.1 Optical phase

Light, according to the classical description, is an electromagnetic field, and is governed by Maxwell's equations [20]. Assuming a homogeneous medium free of charges and currents, that is also linear, nonmagnetic and isotropic, the propagation of the electric or magnetic field, can be reduced to the Helmholtz equation [21]:

$$\left(\nabla^2 - \frac{n^2}{c^2} \frac{\partial^2}{\partial t^2} \right) E = 0 \,, \tag{2.1}$$

where n is the refractive index of the medium, c is speed of propagation in vacuum, and E is the electric field. The simplest solution to this equation is given by the monochromatic plane wave, which can be expressed with the complex expression:

$$E(\vec{r}, t) = \Re\left\{ E_0 \, e^{i\omega t - i\vec{k}\cdot\vec{r}} \right\} \,, \tag{2.2}$$

where E_0 is the amplitude, $\Re\{\cdot\}$ is the real part of a complex function, ω is the angular frequency, $\vec{r}$ is the position vector and $\vec{k}$ is the wavenumber vector, whose modulus is given by:

$$k = \frac{2\pi n}{\lambda} \,, \tag{2.3}$$

where λ is the wavelength. This solution represents an oscillating field, propagating in
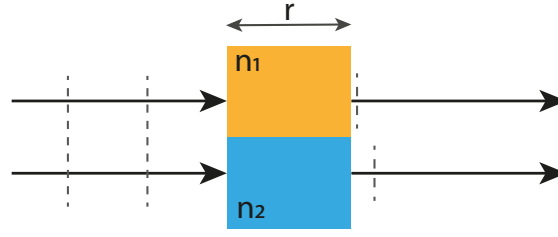
Figure 2.1: Schematic of a plane wave propagating through two different materials of thickness r, described by their refractive indexes n_1 and n_2. The dashed lines indicate the planes with equal phase.

the direction given by $\vec{k}$. The phase of the complex phasor is also called optical phase, and it determines which part of the oscillation cycle is present at a certain time and position.

The optical phase is a property of light, and it can be influenced by the interaction with different materials. As a simple example, let us consider a plane wave propagating along the z direction, in vacuum. Part of this wave crosses a material with refractive index n_1, while another part crosses a material with refractive index n_2, as shown in Fig. 2.1. In this figure, the arrows highlight two beams within the plane wave, while the perpendicular dashed lines indicate planes with equal phase. On the left, before entering the material, the beams are in phase with each other. Upon exiting the materials, the two beams will have accumulated different phases:

$$\phi_1 = \frac{2\pi n_1}{\lambda} r \,,$$
$$\phi_2 = \frac{2\pi n_2}{\lambda} r \,. \tag{2.4}$$

The quantity $n \cdot r$ is referred to as Optical Path Length (OPL). In a more generic context, the OPL can be defined as the integral of the refractive index $n(\vec{r})$ along the geometrical path C:

$$\text{OPL} = \int_C n(\vec{r}) d\vec{r} \,. \tag{2.5}$$

The phase shift between two previously coherent beams can be then linked directly to the Optical Path Difference (OPD):

$$\Delta\phi = \frac{2\pi}{\lambda} \text{OPD} = \frac{2\pi}{\lambda} \left(\text{OPL}_1 - \text{OPL}_2 \right) \,. \tag{2.6}$$

The ability to measure phase differences across a sample allows us to infer changes in its morphology and composition; this is an extremely useful tool for those samples that lack in other properties, like absorption, which is the case for many biological samples.

2.2 Phase imaging

Having established the case for studying phase, the question is then how to measure it. Let us consider a two-dimensional sample described by its complex transmittance $o(x, y)$:

$$o(x, y) = e^{-\mu(x,y)+i\phi(x,y)}, \tag{2.7}$$

where $\mu(x, y)$ defines the absorption of the sample at the coordinates x, y, and $\phi(x, y)$ describes the phase. The sample is illuminated with a plane wave e^{ikz}, thus the field after the interaction with the sample is given by the product [22]:

$$U_o(x, y) = o(x, y) \cdot e^{ikz} = e^{-\mu(x,y)+i(\phi(x,y)+kz)}. \tag{2.8}$$

This field may then be measured by a microscope setup relaying it onto a photodetector. For example, we may consider a simple telecentric imaging system made up of two lenses, as shown in Fig. 2.2. Assuming that the lenses are ideal and that the system satisfies paraxial approximation, it is possible to show that the field at the Image Plane (IP) is a scaled and attenuated version of the object field [21, 23]. The effect of this optical system on the object field can be described simply as a scaling operator $V[-1/M]$ [23]:

$$U_i(x_i, y_i) = \frac{1}{|M|} V\left[-\frac{1}{M}\right] U_o(x_i, y_i) = \frac{1}{|M|} U_o\left(-\frac{x_i}{M}, -\frac{y_i}{M}\right), \tag{2.9}$$

where x_i, y_i are the transverse spatial coordinates in the image plane. Finally, the photodetector will measure the intensity of the image field:

$$I(x_i, y_i) = \left|\frac{1}{|M|} V\left[-\frac{1}{M}\right] U_o(x_i, y_i)\right|^2 = \frac{1}{M^2} V\left[-\frac{1}{M}\right] e^{-2\mu(x,y)}. \tag{2.10}$$

The phase term of the sample does not appear in Eq. 2.10, which means that we are
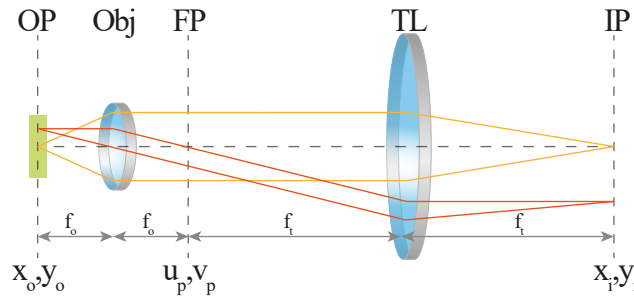
Figure 2.2: Schematic of a telecentric microscope setup. A sample is located in the Object Plane (OP), and the light going through it is collected by an Objective (Obj), at a focal distance f_o from the OP. A second lens, called Tube Lens (TL), at a distance $f_o + f_t$, and focuses an image in the Image Plane (IP). At the bottom of the scheme, the coordinates of each plane are labelled.

not able to directly measure it from intensity measurements, using a simple microscope and photodetector. This is a consequence of the fact that the phase is described by an imaginary exponential, which is inevitably removed by the modulus square since no other complex terms are present in the equation. Indeed, in this example, the effect of the optical system is summarised by the scaling operator, whereas an optical system described by a complex operator would translate the phase term into an intensity pattern [24].

Several methods to introduce a complex term have been developed over the years, such as Zernike phase contrast [25, 26], defocus [27], asymmetric detection and asymmetric illumination [28–30]. In this work, we focus our attention on the use of asymmetric illumination, also referred to as DPC. Among the various phase contrast techniques that were mentioned, asymmetric illumination is particularly simple to implement and doesn't require the use of phase plates. Moreover, image formation in DPC can be described through linear equations, which simplifies the reconstruction of quantitative phase images.

The theory and instrumentation behind this technique are described in the remainder of this chapter.

2.3   Differential phase contrast

Differential Phase Contrast (DPC) refers to a group of imaging methods that employ an asymmetry, either on the illumination or on the detection side, or by introducing offset apertures, such that the resulting amplitude on the detector is related to the phase gradient of the sample [31]. A first detailed analysis of the theory behind this technique was demonstrated for the case of scanning microscopy with a split detector [28], which, under simple conditions, is equivalent to using an asymmetric source with full-field illumination [31]. A more recent version of such system was proposed by Tian et al. [24, 32], using an LED array that can be controlled in such a way to obtain an illumination profile apt for different types of imaging, among which DPC. The following theoretical treatment is based on Tian et al. [24].

2.3.1   Forward model

The typical DPC setup is shown schematically in Fig. 2.3. A spatially partially coherent source, such as a set of Light Emitting Diodes (LEDs), illuminates a transparent sample, described by its complex transmittance function $o(\vec{r}_o) = e^{(-\mu(\vec{r}_o) + i\phi(\vec{r}_o))}$, where $\vec{r}_o$ is the transverse spatial coordinate vector in the object plane, μ is the sample's absorption profile and ϕ is the sample's phase profile. The light field going through the sample is then given by the product between the sample's transmittance and the source's illumination $q(\vec{r}_o)$. If the source is placed far enough from the sample, it is possible to describe its contribution as the incoherent superposition of plane waves, whose intensities are weighted by the source profile $S(\vec{r}_s)$:

$$q(\vec{r}_o) = \sqrt{S(\vec{r}_s)}\, e^{i2\pi \frac{\vec{r}_o \cdot \vec{r}_s}{\lambda z}}\,, \tag{2.11}$$

where λ is the wavelength of the source and z is the distance between the source and the object. The sample is located in the focal plane of an objective lens with focal distance
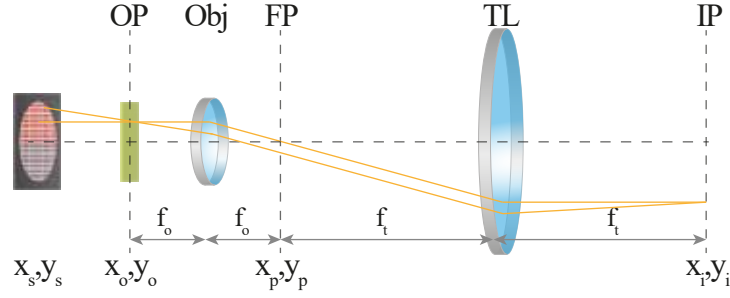
Figure 2.3: Schematic of a DPC microscope setup. A spatially partially coherent source illuminates the phase sample, located in the focal plane of an objective lens (Obj). A Tube Lens (TL) located at a distance f_t from the back focal plane of the Obj focuses an image of the sample at the Image Plane (IP). At the bottom of the scheme the coordinates of each relevant plane are reported.

f_o, which produces a Fourier transform of the transmitted field in the objective lens' Back Focal Plane (BFP). This is low-pass filtered by the system's pupil $P(\vec{r}_p)$, and finally the tube lens focuses an image at the image plane, where a camera detects the field's intensity. This system can thus be described, for a single point illumination, with the following equation:

$$I(\vec{r}_i, \vec{r}_s) \propto \left| \iint \left[\iint q(\vec{r}_o) o(\vec{r}_o) e^{-i2\pi \frac{\vec{r}_o \cdot \vec{r}_p}{\lambda f_o}} d^2\vec{r}_o \right] P(\vec{r}_p) e^{-i2\pi \frac{(\vec{r}_p \cdot \vec{r}_i)}{\lambda f_t}} d^2\vec{r}_p \right|^2. \tag{2.12}$$

The combined effect from the multiple sources can be obtained through an integral over the extension of the source:

$$I(\vec{r}_i) \propto$$
$$\iint \left| \iint \left[\iint \sqrt{S(\vec{r}_s)} e^{i2\pi \frac{\vec{r}_o \cdot \vec{r}_s}{\lambda z}} o(\vec{r}_o) e^{-i2\pi \frac{\vec{r}_o \cdot \vec{r}_p}{\lambda f_o}} d^2\vec{r}_o \right] P(\vec{r}_p) e^{-i2\pi \frac{(\vec{r}_p \cdot \vec{r}_i)}{\lambda f_t}} d^2\vec{r}_p \right|^2 d^2\vec{r}_s. \tag{2.13}$$

With this equation it is possible to calculate the image formed at the camera, with the sole knowledge of the source profile and pupil. On the other hand, the relation is not linear, and it is not possible to easily extract an expression for $\phi(\vec{r}_o)$. In order to simplify Eq. 2.13, we now assume that the object is "weak", meaning that its absorption and phase are low enough that the transmittance can be linearised:

$$o(\vec{r}_o) \approx 1 - \mu(\vec{r}_o) + i\phi(\vec{r}_o). \tag{2.14}$$

Moreover, we discard second order terms appearing in the modulus square, effectively applying the Born approximation [33]. As a consequence, it is possible to demonstrate that the Fourier transform of the image can be expressed as a sum of three linear terms [24, 32]:

$$\tilde{I}(\vec{u}_i) = B\delta(\vec{u}_i) + H_{\text{abs}}(\vec{u}_i)\tilde{\mu}\left(-\frac{f_t}{f_o}\vec{u}_i\right) + H_{\text{ph}}(\vec{u}_i)\tilde{\phi}\left(-\frac{f_t}{f_o}\vec{u}_i\right), \tag{2.15}$$

where $\vec{u}_i$ represents the spatial frequency coordinate at the detector, δ is a Dirac delta, B is the zero frequency component, H_{abs} and H_{ph} are the absorption and phase transfer functions respectively, and $\tilde{\circ}$ represents the Fourier transform of a function. The background and transfer functions are written as:

$$B = \left(\frac{f_o}{f_t}\right)^2 \iint S(\vec{r}_s) \left| P\left(\frac{f_o}{z}\vec{r}_s\right)\right| d^2\vec{r}_s, \tag{2.16}$$

$$H_{\mathrm{abs}}(\vec{u}_i) =$$
$$= -\iint S(\vec{r}_s)\left[P\left(\frac{f_o}{z}\vec{r}_s\right)P^*\left(\frac{f_o}{z}\vec{r}_s + \lambda f_t\vec{u}_i\right) + P^*\left(\frac{f_o}{z}\vec{r}_s\right)P\left(\frac{f_o}{z}\vec{r}_s - \lambda f_t\vec{u}_i\right)\right]d^2\vec{r}_s, \tag{2.17}$$

$$H_{\mathrm{ph}}(\vec{u}_i) =$$
$$= i\iint S(\vec{r}_s)\left[-P\left(\frac{f_o}{z}\vec{r}_s\right)P^*\left(\frac{f_o}{z}\vec{r}_s + \lambda f_t\vec{u}_i\right) + P^*\left(\frac{f_o}{z}\vec{r}_s\right)P\left(\frac{f_o}{z}\vec{r}_s - \lambda f_t\vec{u}_i\right)\right]d^2\vec{r}_s. \tag{2.18}$$

Notice that f_t/f_o corresponds to the magnification M of the microscope. Complete derivation of these equations is provided in Appendix A.

2.3.2   Properties of the transfer functions

Given the equations for the transfer functions, it is useful to take a look at their typical appearance and properties. Let us assume that the microscope setup of Fig. 2.3 is free of aberrations. This means that the pupil function $P(\vec{r}_p)$ can be modelled as a circle whose radius is defined by the Numerical Aperture (NA) of the objective. The system only transmits spatial frequencies within the NA, thus the pupil is zero outside the radius and unitary inside, as shown in Fig. 2.4(a): such pupil function is real and even.

As a consequence, the term in square brackets in Eq. 2.17 is even in $\vec{r}_s$, whereas the term in square brackets in Eq. 2.18 is odd in $\vec{r}_s$.

In order to remove the absorption term and enhance the phase term, it is then sufficient to find an odd illumination profile $S(\vec{r}_s)$: in Eq. 2.17, the product between an odd source and the even term in the square brackets would make the integral null over the whole domain of $\vec{u}_i$, thus leaving only the phase term to contribute to the image at the detector. Of course it is not possible to generate an odd illumination profile, since it would require negative intensity. On the other hand, it is possible to use two mirrored illuminations to simulate such an effect.

For example, the source profile depicted in Fig. 2.4(b) is asymmetric with respect to the origin, and it would generate the following image:

$$\tilde{I}_T(\vec{u}_i) = B_T\delta(\vec{u}_i) + H_{T,\mathrm{abs}}(\vec{u}_i)\tilde{\mu}(-M\vec{u}_i) + H_{T,\mathrm{ph}}(\vec{u}_i)\tilde{\phi}(-M\vec{u}_i), \tag{2.19}$$

where the subscript T indicates we are using the top half circle illumination. If we now

illuminate the sample with the bottom half circle, we obtain:

$$\tilde{I}_B(\vec{u}_i) = B_B \delta(\vec{u}_i) + H_{B,\text{abs}}(\vec{u}_i)\tilde{\mu}(-M\vec{u}_i) + H_{B,\text{ph}}(\vec{u}_i)\tilde{\phi}(-M\vec{u}_i) =$$
$$= B_T \delta(\vec{u}_i) + H_{T,\text{abs}}(\vec{u}_i)\tilde{\mu}(-M\vec{u}_i) - H_{T,\text{ph}}(\vec{u}_i)\tilde{\phi}(-M\vec{u}_i) .$$
(2.20)

Finally, the DPC image is obtained as:

$$\tilde{I}_{\text{DPC}}(\vec{u}_i) = \frac{\tilde{I}_T - \tilde{I}_B}{\tilde{I}_T + \tilde{I}_B} \approx \frac{H_{T,\text{ph}}(\vec{u}_i)\tilde{\phi}(-M\vec{u}_i)}{B_T} = H_{\text{DPC,ph}}(\vec{u}_i)\tilde{\phi}(-M\vec{u}_i) ,$$
(2.21)

where, at the denominator, we approximated $H_{T,\text{abs}}(\vec{u}_i)\tilde{\mu}(-M\vec{u}_i) \ll B_T$ [24]. The DPC phase transfer function is given by:
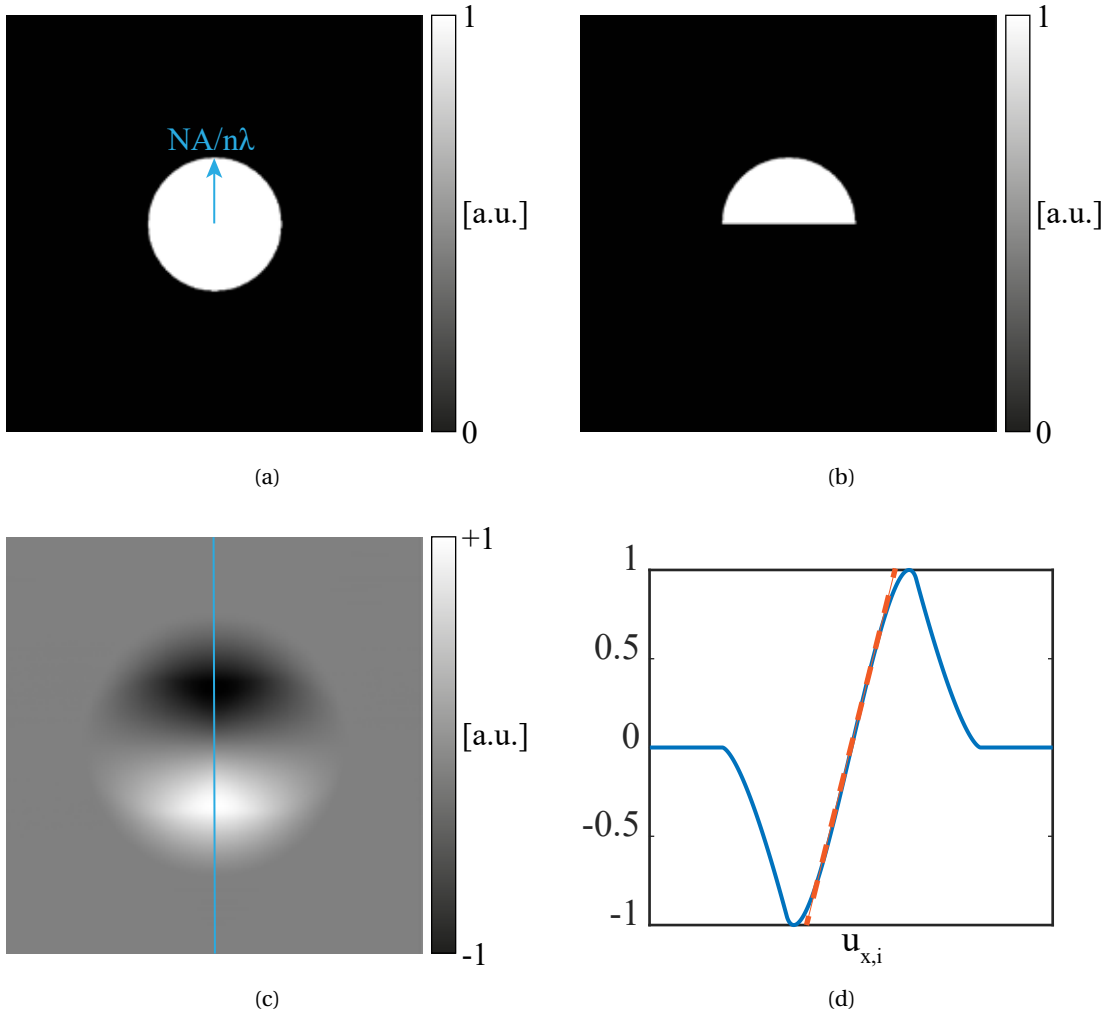
Figure 2.4: (a) Pupil function $P(\vec{r}_p)$; (b) source profile $S(\vec{r}_s)$; (c) normalised phase transfer function $H_{\text{ph}}(\vec{u}_i)$; (d) cross section of the phase transfer function; in orange, linear interpolation around the zero spatial frequency.

11

$$H_{\mathrm{DPC,ph}} = \frac{H_{T,\mathrm{ph}}(\vec{u}_i)}{B_T}. \qquad (2.22)$$

An example of a phase transfer function is shown in Fig. 2.4(c), and the vertical cross section is shown in Fig. 2.4(d). First, we observe that the cutoff frequency of the transfer function is twice than that allowed by the NA. This is a direct consequence of the incoherent nature of the source [21, 24].

The cross section in Fig. 2.4(d) shows that, around the zero spatial frequency, the transfer function can be approximated by a linear interpolation $\alpha u_{x,i}$, where $u_{x,i}$ is the vertical spatial frequency coordinate and α is a constant. In other words, since this transfer function is imaginary, the image can be written as:

$$\tilde{I}_{\mathrm{DPC}}(\vec{u}_i) \approx i\alpha u_{x,i}\tilde{\phi}(-M\vec{u}_i). \qquad (2.23)$$

This expression in the Fourier domain corresponds to the derivative in the real domain. This means that the DPC images are expected to look somewhat proportional to the phase gradient in the direction perpendicular to the axis of asymmetry. An example of a phase object and corresponding DPC image are shown in Fig. 2.5.

The magnitude of the transfer in generally poor for low spatial frequencies, and in particular it is null in the direction of the axis of illumination asymmetry. As a consequence, some distortions due to missing information are to be expected. A way to mitigate this issue is to record multiple images from different illuminations. For example, a second axis of illumination can be used, perpendicular to the first, so that a total of four images are recorded. The more illuminations are used, the better the coverage of the spatial frequencies is.

(a)

(b)
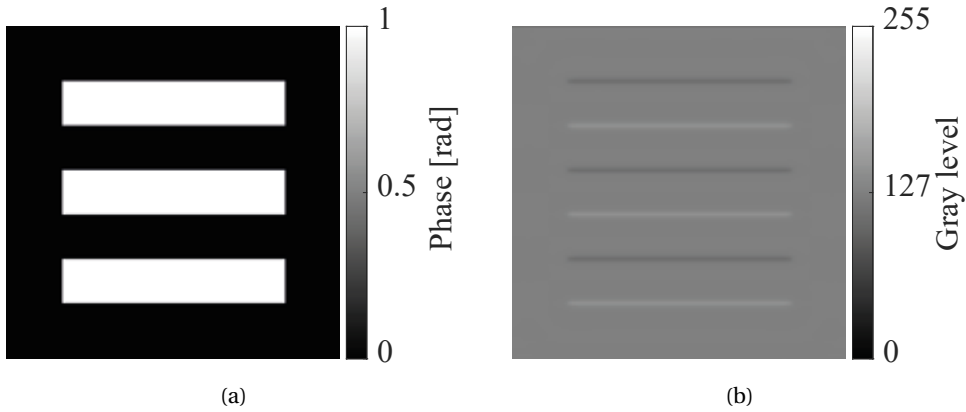
Figure 2.5: (a) Simulated phase object; (b) simulated phase image obtained from vertical half circle illumination.

12

2.3.3   Reconstruction of quantitative phase

As seen in the previous section, the DPC images are similar to the gradient of the phase of the object. On the other hand, we are interested in obtaining a quantitative map of the actual phase of the sample. From Eq. 2.21, we can see that, in the Fourier domain, the DPC image and the phase object are related by a linear equation, through the phase transfer function $H_{\mathrm{DPC,ph}}$. It is relatively simple to invert this equation, though some care is required: as was mentioned previously, the transfer function is null for several spatial frequency values. This means that inversion by division is not immediately possible, as this would blow up the noise present at all spatial frequencies.

In order to solve this issue, a better approach is to set a minimization problem which includes a regularization parameter [24]:

$$\min \sum_j \left| \tilde{I}_{\mathrm{DPC},j}(\vec{u}_i) - H_{\mathrm{DPC},j}(\vec{u}_i)\tilde{\phi}(-M\vec{u}_i) \right|^2 + \alpha \left| \tilde{\phi}(-M\vec{u}_i) \right|^2, \tag{2.24}$$

where the j is the index for the DPC images taken with different illuminations. The solution to this problem is expressed as a Tikhonov regularisation:

$$\phi_{\mathrm{inv}}(\vec{r}_i) = \mathfrak{F}^{-1} \left\{ \frac{\sum_j H_{\mathrm{DPC},j}^*(\vec{u}_i)\tilde{I}_{\mathrm{DPC},j}(\vec{u}_i)}{\sum_j |H_{\mathrm{DPC},j}|^2(\vec{u}_i) + \alpha} \right\}, \tag{2.25}$$

where $\mathfrak{F}$ is the Fourier transform operator and $\mathfrak{F}^{-1}$ is the inverse Fourier transform. The role of the regularisation parameter is to avoid fitting the noise: if the regularization parameter is too small, the inversion process will fit the noise and the reconstruction will suffer from excessive oscillations; if the regularization parameter is too big, the data will be under-fitted and errors will arise. It is a good approach to look for the smallest parameter that suppresses oscillations [34], but the optimal value depends on the quality of the data. Several approaches to automatically select the best parameter have been proposed [34–36], but often a manual approach is employed.

Alternatively, iterative methods can also be used to reconstruct the phase object.

2.4   Interferometric and non-interferometric phase imaging: a comparison

Techniques based on incoherent illumination are not the only available option when it comes to phase imaging. Another broad category of phase imaging techniques is that of interferometry. The idea behind interferometric imaging is to use a reference field to mix with the field that interacted with the sample. As a consequence, the phase of the object can be retrieved from an intensity measurement, provided that some information regarding the reference field is known. A variety of interferometric techniques exist, such as off-axis holography [37–39], phase-shifting interferometry [40, 41], common path interferometry [42, 43], as well as many combinations and variations over these [22]. A detailed analysis of these phase imaging methods is beyond the scope of this work, but it is worth discussing what are the differences

between using coherent or incoherent light, and which should be chosen based on the specific application.

In this context, we will consider the imaging system of DPC to be perfectly incoherent. While the light source used is incoherent, the resulting image can still be partially coherent [21, 44]. It is possible to express a sufficient condition for the imaging system to behave as perfectly incoherent, in terms of the projected size of the illumination source onto the imaging system pupil [44]. While this condition doesn't necessarily apply in the case of DPC, it still shows that an incoherent image is a good approximation, and as such we will consider the properties of incoherent imaging to belong to DPC as well.

2.4.1 Cutoff frequency

Let us consider an imaging system whose amplitude impulse response is described by $h(x, y)$. In a perfectly coherent imaging system with no aberration, the amplitude at the image plane $U_i(x, y)$ is related to the input amplitude $U_o(x, y)$ through a convolution:

$$U_i(x, y) = \iint h(x - \xi, y - \eta) U_o(\xi, \eta) d\xi d\eta. \tag{2.26}$$

This equation can be transformed to the Fourier domain, where a linear relation between input and output is obtained:

$$\tilde{U}_i(u, v) = H(u, v) \tilde{U}_o(u, v). \tag{2.27}$$

The function $H(u, v)$ is called Amplitude Transfer Function (ATF), and relates the spatial frequency content of the object to the image plane. A perfectly incoherent imaging system is linear in intensity rather than amplitude [21], so that we can write:

$$I_i(x, y) \propto \iint \left| h(x - \xi, y - \eta) \right|^2 I_o(\xi, \eta) d\xi d\eta. \tag{2.28}$$

In this case, we obtain a linear relation for the Fourier transforms of the object and image intensities:

$$\tilde{I}_i(u, v) = \mathfrak{H}(u, v) \tilde{I}_o(u, v), \tag{2.29}$$

where $\mathfrak{H}$ is the Optical Transfer Function (OTF):

$$\mathfrak{H}(\mathfrak{u}, \mathfrak{v}) = \mathfrak{F}\left\{ \left| h(x, y) \right|^2 \right\}. \tag{2.30}$$

Let us now consider the case of a circular pupil with radius w and with no aberration:

$$P(x, y) = \text{circ}\left(\frac{\sqrt{(x^2 + y^2)}}{w} \right). \tag{2.31}$$

In the coherent case, the ATF turns out to be:

$$H(u, v) = \text{circ}\left(\frac{\sqrt{u^2 + v^2}}{w/\lambda z_i}\right),\tag{2.32}$$

where z_i is the distance of the image plane from the exit pupil of the optical system.

This transfer function is unity within a circle of radius $f_0 = w/\lambda z_i$, which we call cutoff frequency. Spatial frequencies above this value are not transferred to the image, so the cutoff frequency can be regarded as a measure of the resolution given by the optical system.

The calculation for the incoherent case is not as intuitive, but it is possible to demonstrate that the OTF is non-zero within a circle of radius $2f_0$ [21]. On the other hand, the spatial frequency transfer is not constant to unity in this case, but it gradually decreases to zero at $2f_0$. While this means that we cannot exactly claim that the resolution of incoherent systems is twice as that of a coherent system, it is still possible to see that more high-frequency components are retained in the image formed by an incoherent system.

2.4.2 Ringing patterns

Another feature that differentiates coherent and incoherent systems is their response to steep edges.

Coherent system have a transfer function with a sharp transition to zero at the cutoff frequency, which results in typical ringing patterns of over-and under-shoots around steep edges. This type of distortion can be an issue when quantifying sizes of objects, and it doesn't appear in incoherent systems thanks to their smooth OTF.

2.4.3 Speckle patterns

Speckle patterns are also a feature affecting only coherent systems. They arise from the coherent interference of light reflected by multiple interfaces such as lenses, beam splitters or by scatterers on those surfaces, which generate a granular looking patch with intensity discontinuities. The intensity contrast of these speckles can vary based on the degree of coherence of the source, and the only solution to remove it is by introducing some random time perturbation of the speckle pattern that is faster than the exposure time for one image, such that different speckle patterns are averaged. A moving or rotating diffuser serves that purpose for example. This is not a convenient solution in many cases, and it requires mechanical motion of elements such as diffusers.

Due to the very nature of speckle patterns, incoherent optical system are not affected by them.

2.4.4 Setup complexity and sensitivity

One last factor that needs to be mentioned is related to the differences in coherent and incoherent based imaging setups. Interferometric systems typically require a higher degree of stability of optical components, for example in terms of vibrations, especially for the configurations with separate paths for sample and reference light. Common path configurations also require

high precision in the positioning of elements such as spatial filters. These requirements are markedly not as strict for incoherent imaging. Moreover, coherent sources are highly sensitive to disturbances such as optical imperfections, which can introduce significant distortions of the diffraction patterns.

Overall, several advantages of incoherent based imaging have been mentioned here. The use of simple LEDs as incoherent sources in DPC gives multiple advantages over interferometric techniques, which motivates their use over lasers and interferometry. As will be shown in Chapter 3, a major limitation of DPC is its low phase sensitivity compared to interferometry. Chapter 4 will demonstrate a novel approach to DPC that circumvents the sensitivity limitation and allows a comparable performance to the state of the art interferometric techniques.

3 Phase sensitivity in Differential Phase Contrast

The content of this chapter is largely based on the paper: C. Bonati, T. Laforest, M. Kunzi, and C. Moser, "Phase sensitivity in differential phase contrast microscopy: limits and strategies to improve it," *Opt. Express*, vol. 28, pp. 33767-33783(2020).

3.1 Introduction

As discussed in Chapter 2, DPC refers to a group of phase imaging methods that employ an asymmetry, either on the illumination or on the detection side, or by introducing offset apertures, such that the resulting intensity on the detector bears information regarding the phase gradient of the sample [28]. In this chapter, the attention is focused on a DPC configuration that employs multiple asymmetric sources of illumination (such as LEDs). This approach to DPC is of interest for microscopic imaging of transparent samples: numerous ex-vivo biological applications have been demonstrated over the years [2–10]. Moreover, its use has been proven in cases such as in-vivo imaging of human retina [11], where interferometric techniques have limited capabilities in detecting structures with low reflectivity [12].

While several publications have explored the spatial resolution of this technique [24, 45], not much attention has been given to the phase sensitivity performance that can be achieved, as well as the parameters affecting it and the fundamental limit. A few experimental, setup-specific phase sensitivity values can be found in the literature [46–48], but a complete study of the parameters that dictate the limit of phase sensitivity is still missing. Moreover, the widespread use of standard test-targets for setup characterisation does not provide insight regarding samples with different spatial-frequency content. Indeed, biological samples tend to have more low-frequency components compared to standard targets.

Ideally, any phase structure in the object generates a pattern of a certain intensity, whose minimum value could be a single photon. On the other hand, any source of noise limits detection only to the intensity values greater than the overall noise. The sensitivity limit of the DPC technique is thus given by the phase value that generates an intensity pattern whose amplitude equals that of the noise.

In this chapter, I analyse the main factors that determine phase sensitivity in DPC detection. First, contrast trends are shown and discussed for different types of samples. Simulations of several DPC configurations are used to give a guideline as to how the contrast

can be optimized for specific sample features. A simple approach is then described to evaluate the sensitivity performance of a DPC setup. The information required for this estimation are simply the illumination profile, the sample shape and an experimental model of Poissonian-Gaussian noise [49, 50]. This simulation can be performed before the DPC setup is actually built, so it represents a powerful tool to explore the possible DPC configurations and choose the most suited to the specific user needs in terms of sensitivity and resolution. Experimental verification complements the simulations.

Finally, the sensitivity limit for common DPC configurations is discussed and compared to other phase imaging techniques.

3.2 Theory

As seen in Chapter 2, image formation in DPC is governed by approximated linear equations in the spatial frequency domain, where the object's phase and absorption terms are related to the image through transfer functions. The equation is recalled here for convenience:

$$\tilde{I}(\vec{u}_i) = B\delta(\vec{u}_i) + H_{\mathrm{abs}}(\vec{u}_i)\tilde{\mu}\left(-\frac{f_t}{f_o}\vec{u}_i\right) + H_{\mathrm{ph}}(\vec{u}_i)\tilde{\phi}\left(-\frac{f_t}{f_o}\vec{u}_i\right), \tag{3.1}$$

where H_{ph} is given by:

$$\begin{aligned} H_{\mathrm{ph}}(\vec{u}_i) &= \\ &= i \iint S(\vec{r}_s)\left[-P\left(\frac{f_o}{z}\vec{r}_s\right)P^*\left(\frac{f_o}{z}\vec{r}_s + \lambda f_t \vec{u}_i\right) + P^*\left(\frac{f_o}{z}\vec{r}_s\right)P\left(\frac{f_o}{z}\vec{r}_s - \lambda f_t \vec{u}_i\right)\right]d^2\vec{r}_s. \end{aligned} \tag{3.2}$$

Therefore, the two critical parameters are the source profile S and the pupil function P. For a non aberrated setup, the pupil is a circular function of radius $\mathrm{NA}_{\mathrm{obj}}/(n\lambda)$ in the spatial frequency space, where $\mathrm{NA}_{\mathrm{obj}}$ is the objective's numerical aperture, λ is the illumination wavelength and n is the refractive index of the medium in which the objective is immersed. The source profile can vary as long as it is asymmetric, in order to correctly perform DPC [24]. It has been shown that optimal results are obtained with a half ring illumination [45], whose external radius matches $\alpha_{\mathrm{outer}}\mathrm{NA}_{\mathrm{obj}}/(n\lambda)$ and the internal radius is $\alpha_{\mathrm{inner}}\mathrm{NA}_{\mathrm{obj}}/(n\lambda)$, with $\alpha_{\mathrm{outer}} = 1$ and $\alpha_{\mathrm{inner}} < 1$. Throughout this chapter, I will assume the half ring illumination. An example of source, pupil, and resulting phase transfer function are shown in Fig. 3.1.

The spatial resolution will be mostly limited by the frequency cutoff of this transfer function, while the contrast depends on the total overlap between the spatial spectrum of the sample and the shape of the transfer function [29]: to obtain the real space image, it is necessary to inverse Fourier transform Eq. 3.1, obtaining a modulated integral of the product between H_{ph} and $\tilde{\phi}$. Indeed, for a phase-only object:

$$I(\vec{r}_i) = B + \mathfrak{F}^{-1}\left[H_{\mathrm{ph}}(\vec{u}_i)\tilde{\phi}\left(-\frac{f_t}{f_o}\vec{u}_i\right)\right]. \tag{3.3}$$
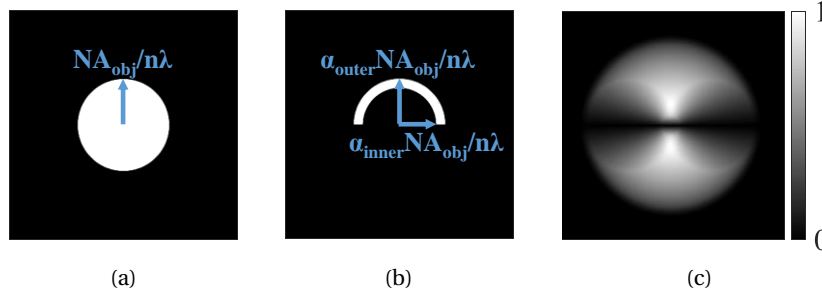
Figure 3.1: (a) Pupil function: circle of radius $\text{NA}_{\text{obj}}/(n\lambda)$; (b) Source function: half ring with external radius $\alpha_{\text{outer}}\text{NA}_{\text{obj}}/(n\lambda)$ and internal radius $\alpha_{\text{inner}}\text{NA}_{\text{obj}}/(n\lambda)$, with $\alpha_{\text{outer}} = 1$ and $\alpha_{\text{inner}} < 1$; (c) Normalized phase transfer function obtained with the pupil of Fig. 3.1 (a) and the source of Fig. 3.1 (b).

The contrast is then given by the difference between the maximum and minimum pixel values in the region of interest:

$$c = \max\left\{\mathfrak{F}^{-1}\left[H_{\text{ph}}(\vec{u}_i)\tilde{\phi}\left(-\frac{f_t}{f_o}\vec{u}_i\right)\right]\right\} - \min\left\{\mathfrak{F}^{-1}\left[H_{\text{ph}}(\vec{u}_i)\tilde{\phi}\left(-\frac{f_t}{f_o}\vec{u}_i\right)\right]\right\}, \qquad (3.4)$$

while the normalized contrast is obtained as:

$$c = \frac{\max\left\{\mathfrak{F}^{-1}\left[H_{\text{ph}}(\vec{u}_i)\tilde{\phi}\left(-\frac{f_t}{f_o}\vec{u}_i\right)\right]\right\} - \min\left\{\mathfrak{F}^{-1}\left[H_{\text{ph}}(\vec{u}_i)\tilde{\phi}\left(-\frac{f_t}{f_o}\vec{u}_i\right)\right]\right\}}{\max\left\{\mathfrak{F}^{-1}\left[H_{\text{ph}}(\vec{u}_i)\tilde{\phi}\left(-\frac{f_t}{f_o}\vec{u}_i\right)\right]\right\} + \min\left\{\mathfrak{F}^{-1}\left[H_{\text{ph}}(\vec{u}_i)\tilde{\phi}\left(-\frac{f_t}{f_o}\vec{u}_i\right)\right]\right\}}. \qquad (3.5)$$

For this reason, an analysis of the sensitivity requires careful consideration of the sample's shape. In most cases, simulations and experiments are performed using standard samples such as the USAF target, which contains repeated rectangular patterns of varying size. These sharp-edged shapes are characterised by significant high-frequency content in the spatial frequency domain. This is not the case for most biological structures, which tend to be smoother and thus present more low-frequency content. In the following, I will explore how different spatial frequency spectra interact with the phase transfer function of DPC, and how their overlap can be optimised to increase contrast.

3.2.1 Real samples: a frequency domain analysis of transfer function matching

The main characteristic that dictates the sample's spectrum is its sharpness, i.e. the magnitude of its derivative. For example, a sharp object like a rectangle has a broad frequency spectrum, while a smoother object has a spectrum more localized around low frequencies. To show the effect of the smoothness of the sample on the contrast, one can use two example shapes in the simulations. In this chapter, I will use a sharp circle and a truncated sinusoid, as shown in 3.2 (a) and (d). A cross section of their normalized spectra is shown in Fig. 3.2 (c) and (f); the
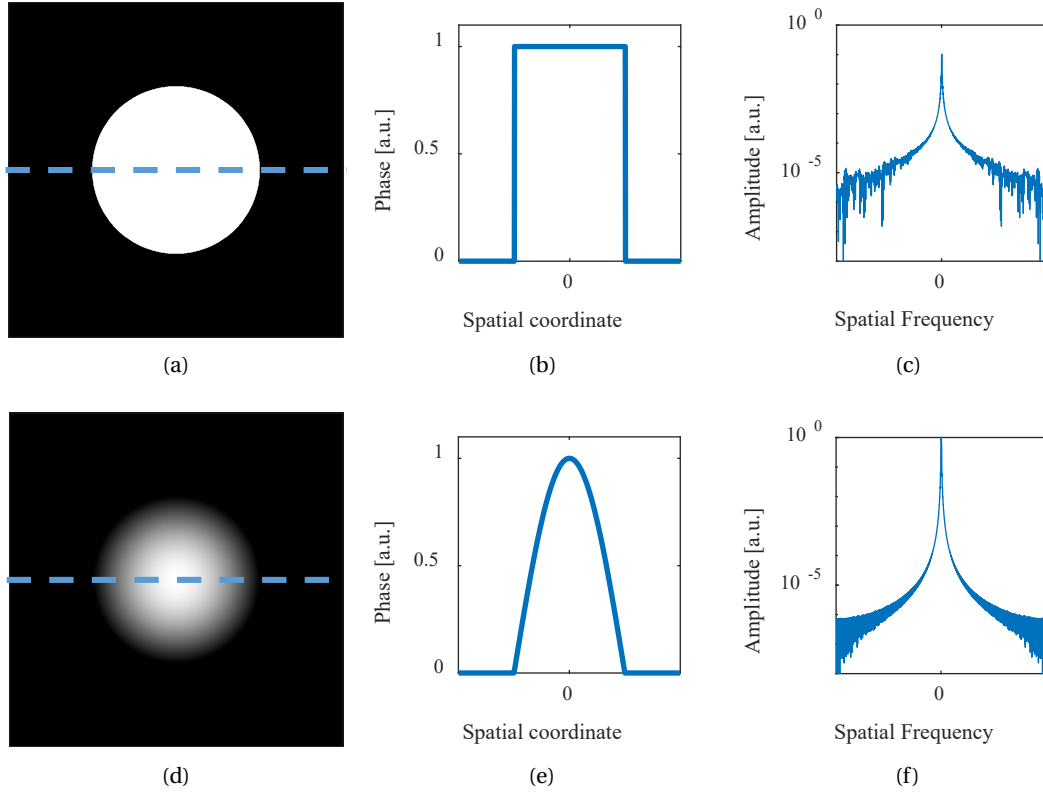
Figure 3.2: (a) Sharp circular object, (b) a cross-section along the blue line, and (c) a cross section of its spectrum in log scale; (d) smooth circular object, (e) a cross-section along the blue line, and (f) a cross section of its spectrum in log scale.

sharp object has higher amplitude in the high frequency tails, compared to the smooth object. This fact influences contrast via the transfer function, as shown in Eq. 3.4.

As depicted in Fig. 3.1 (a), the two main parameters that change the shape of the transfer function are NA_{obj} and α_{inner}. The false colour maps of Fig. 3.3 (a) and (b) show how the normalized contrast changes for the two classes of objects. The contrast is normalized to 1 for the maximum contrast obtained with each object. To better understand the effect of the two parameters NA_{obj} and α_{inner}, one can look at the plots of Fig. 3.3 (c) and (d). In Fig. 3.3 (c) the normalized contrast is plotted against NA_{obj} varying between 0.1 and 0.9 for $\alpha_{inner} = 0.6$; in the maps of Fig. 3.3 (a) and (b) this is shown as a blue line with circular markers for the sharp object and cross markers for the smooth object. Comparing the trend of contrast for the sharp and smooth objects as a function of NA_{obj}, one can notice that for the sharp object, the contrast is nearly unchanged, while with the smooth object, increasing the NA_{obj} reduces contrast by almost 40%. Fig. 3.3 (d) shows the contrast trends for $NA_{obj} = 0.6$ and α_{inner} varying between 0 and 0.9. In this case, while the absolute values of contrast change, the trend is the same for both objects.

As suggested previously in this chapter, the differences in contrast for smooth and sharp objects are easily explained in Fourier space. This is best illustrated in Fig. 3.4, where cross-
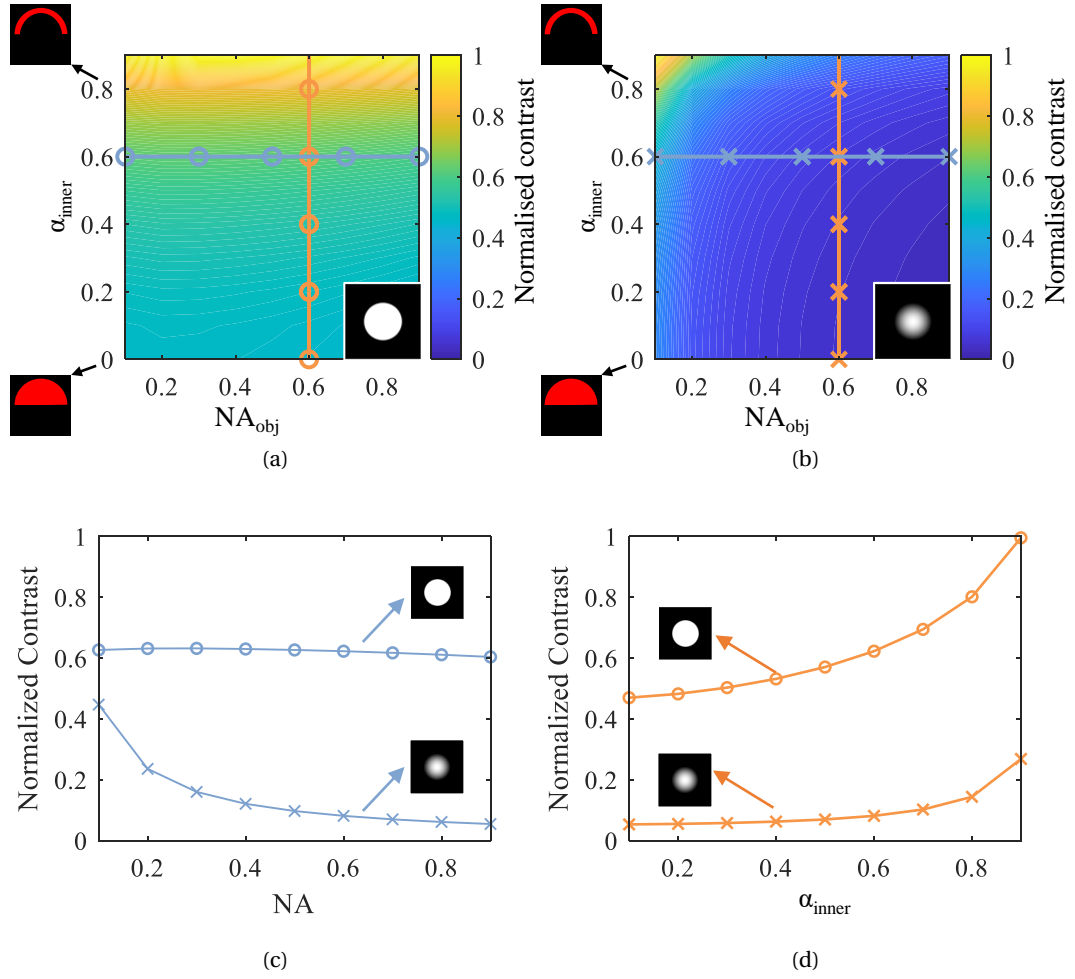
Figure 3.3: (a) Normalized contrast vs. NA$_{obj}$ and α_{inner} for the object of Fig. 3.2 (a) (shown in the inset). The insets on the left show the illumination profile for two α_{inner} values. (b) Normalized contrast vs. NA$_{obj}$ and α_{inner} for the object of Fig. 3.2 (d) (shown in the inset). The insets on the left show the illumination profile for two α_{inner} values. (c) Normalized contrast for $\alpha_{inner} = 0.6$. The line with circle markers refers to the sharp object, while the cross markers refer to the smooth object. (c) Normalized contrast for NA$_{obj} = 0.6$. The line with circle markers refers to the sharp object, while the cross markers refer to the smooth object. The lines in (a) and (b) show where the plots of (c) and (d) have been obtained.

(a)

(b)
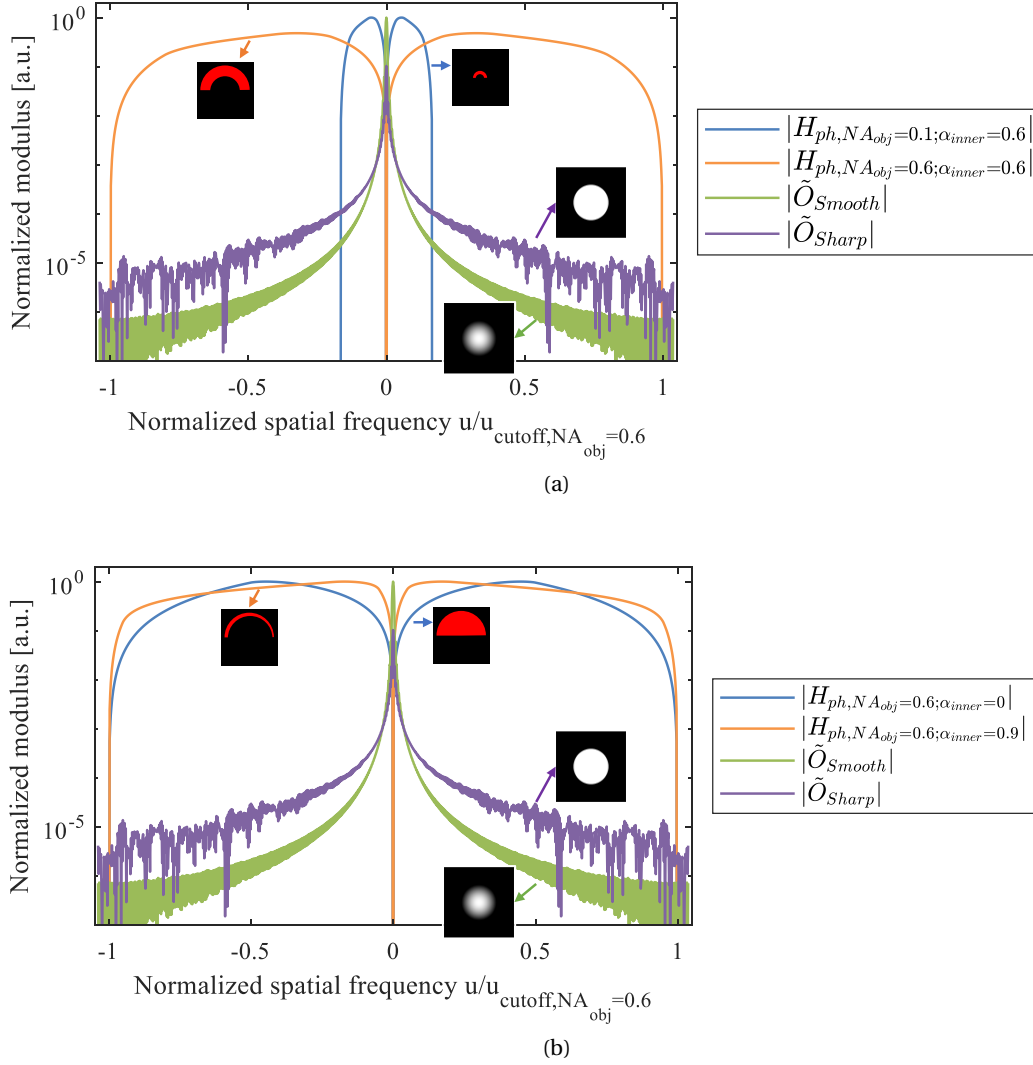
Figure 3.4: (a) Cross-section of the normalized modulus of the phase transfer function H_{ph} for two values of NA_{obj} at fixed α_{inner}, compared with the cross-section spatial frequency spectrum of the sharp and smooth object, $\tilde{O}_{\mathrm{Sharp}}$ and $\tilde{O}_{\mathrm{Smooth}}$ respectively; assuming that the axis of asymmetry of illumination is in direction $(0, u_y)$, the cross-section is taken in the perpendicular direction $(u_x, 0)$. The black and white insets show the shape of the objects corresponding to the respective cross sections, while the black and red insets show the illumination profiles that originated each phase transfer function. (b) Cross-section of the normalized modulus of the phase transfer function H_{ph} for two values of α_{inner} at fixed NA_{obj}, compared with the spatial frequency spectrum of the sharp and smooth object. The black and white insets show the shape of the objects corresponding to the respective cross sections, while the black and red insets show the illumination profiles that originated each phase transfer function.

sections of the spatial frequency spectra of the sharp and smooth object, $\tilde{O}_{\text{Sharp}}$ and $\tilde{O}_{\text{Smooth}}$, are compared to several phase transfer function cross-sections, normalized to their respective background values. In Fig. 3.4 (a), the phase transfer functions are computed for two values of NA_{obj} (0.1 and 0.6) at a fixed value of $\alpha_{\text{inner}} = 0.6$. One can observe that, as expected, for the larger NA_{obj}, the transfer function has a higher cutoff frequency, which would increase resolution. On the other hand, the amplitude of the transfer function at low frequencies is reduced. For the sharp object, the lower amount of information collected at low frequencies for larger NA_{obj} is compensated by the integration of the information at higher frequencies. For the smooth object instead, the high frequencies have such small amplitude that the loss of information at low frequencies results in a lower contrast.

In Fig. 3.4 (b), the case of varying α_{inner} (0.1 and 0.9) for fixed $NA_{\text{obj}} = 0.6$ is shown instead. At the increase of α_{inner}, the cutoff frequency does not change, while the transfer for low frequencies increases. This is beneficial both for the sharp and smooth object, which indeed have an increasing contrast as shown in Fig. 3.3 (d) [24].

3.2.2 Simulation and estimation of the sensitivity limit

In this section, the goal is to define a framework to simulate image formation for a given sample and DPC microscopy setup, and to estimate the minimum phase variation in the sample that can be detected. The standard definition for the sensitivity is the magnitude of the quantity of interest for which the SNR equals one. Typical DPC images present a strong background, so it is rather more appropriate to use the Contrast to Noise Ratio (CNR), which measures the ratio between the difference in intensity of two reference points in the image and the noise [51, 52]. In DPC, an object appears with its edges highlighted in opposite grey level polarity with respect to the background, so the maximum and minimum grey levels are considered to compute the CNR.

The first step is to simulate the DPC image. The phase transfer function is computed using Eq. 3.2. Details on the exact image formation equations are given in Appendix A, and for the method of simulation see Appendix B. Given an a-priori knowledge of the general shape of the phase object of interest, or in other words of its spatial frequency spectrum, we can then calculate the contrast as in Eq. 3.4:

$$c = \max\left\{\mathfrak{F}^{-1}\left[H_{\text{ph}} p \tilde{\phi}_{01}\right]\right\} - \min\left\{\mathfrak{F}^{-1}\left[H_{\text{ph}} p \tilde{\phi}_{01}\right]\right\}, \tag{3.6}$$

where p is the phase magnitude and $\tilde{\phi}_{01}$ is the phase spectrum of the object normalized between 0 and 1.

Regarding the noise, I assume that the main contributions arise from the camera, in particular in the form of shot-noise [53] and a signal independent component. We model the Poissonian-Gaussian noise of the specific camera in use following the MATLAB®algorithm developed by Foi et al. [49, 50]. The overall standard deviation of the noise is defined as $\sigma(I) = \sqrt{aI(x) + b}$, where a and b are the parameters that define the Poissonian and the Gaussian noise, respectively, and $I(x)$ is the intensity at pixel location x. The algorithm is capable of characterizing the noise profile of the camera from an image, by segmenting it in

areas of uniform intensity. The noise model is then fitted to the data points of intensity and standard deviation of each area, giving back the parameters a, b.

The sensitivity limit can be estimated as the phase magnitude p such that the CNR is equal to 1:

$$CNR = \frac{\max\left\{\mathfrak{F}^{-1}\left[H_{\text{ph}} p \tilde{\phi}_{01}\right]\right\} - \min\left\{\mathfrak{F}^{-1}\left[H_{\text{ph}} p \tilde{\phi}_{01}\right]\right\}}{\sigma(I_b)} \, , \tag{3.7}$$

$$p_{\text{sensitivity}} = \frac{\sigma(I_b)}{\max\left\{\mathfrak{F}^{-1}\left[H_{\text{ph}} \tilde{\phi}_{01}\right]\right\} - \min\left\{\mathfrak{F}^{-1}\left[H_{\text{ph}} \tilde{\phi}_{01}\right]\right\}} \, , \tag{3.8}$$

where $\sigma(I_b)$ is the noise standard deviation calculated at the background intensity. Other sources of noise may be included as a more sophisticated upgrade of this simulation, without changing the main steps here described. Indeed, it is only necessary to find and apply the correct model for the noise to compute $\sigma(I_b)$.

3.2.3   Reconstructing samples below the sensitivity limit

The sensitivity limit obtained with the calculations of Section 3.2.2 is related to the single DPC image. According to this definition, if the sample under observation were below the sensitivity limit, it would not be visible. On the other hand, DPC reconstructions can use multiple images to improve the fidelity of the retrieved phase. Normally, at least two images are recorded, with mirrored illumination profiles; the pixel-wise difference of the two images is then calculated, and this resulting image is used to reconstruct the phase. This digital subtraction process increases the modulation given by the sample by a factor of 2, while the noise standard deviation is also increased by a factor of $\sqrt{2}$. Overall, the image used for inversion will have a CNR that is $\sqrt{2}$ times that of the single image. Using more axis of illumination, the coverage of the spatial frequency spectrum is improved [4, 24], and if a sufficient number of images is used, the sample may be reconstructed even if the CNR of a single image is below one.

Nevertheless, it is important to be aware of the sensitivity limit of a single image in a given setup, since a set of higher quality single images will provide a better reconstruction. Moreover, if the reconstruction is performed off-line, the user of the microscope will only be able to see a stream of single DPC images.

The choice of reconstruction algorithm and parameters is also influenced by the quality of the DPC images. Both iterative [54] and direct [24] inversion methods have been demonstrated for DPC data, with Tikhonov inversion being the most common. In this method, a regularization parameter is used to balance the effect of fitting noise in the data: if the regularization parameter is too small, the inversion process will fit the noise and the reconstruction will suffer from excessive oscillations; if the regularization parameter is too big, the data will be under-fitted and errors will arise. It is a good approach to look for the smallest parameter that suppresses oscillations [55], but the optimal value depends on the quality of the data. Several approaches to automatically select the best parameter have been proposed [35, 36, 55], but often a manual approach is employed. In this case, the regularization parameter is chosen to be

proportional to the reciprocal of the CNR. As a result, images with low CNR are to be inverted with rather big regularization parameters, resulting in partially distorted reconstructions.

In this Chapter, I show experimentally in Section 3.3.3 that, by performing a phase reconstruction with four images, the ground truth phase can be recovered and confirmed by the theoretical contrast values. For the phase reconstruction, I followed the manual approach, starting from the inverse of the CNR and then testing several values until I obtained a satisfactory trade-off between accuracy of the reconstructed shape and management of noise amplification. Our results are applied to single images for which there is a detectable phase contrast (CNR > 1). As noted earlier, it may still be possible to reconstruct the phase from single images which are below the phase contrast limit.

3.3 Experimental validation

3.3.1 Setup

The DPC setup used in the experiments is shown in Fig. 3.5. Illumination from red LEDs (660 nm) is focused onto the sample with a 4f system. The light exiting the sample is collected by an objective (20x magnification, 0.5 NA) whose BFP is relayed with a 4f system. A variable aperture is located at the relayed BFP, and by changing its radius, the effective NA of the setup can be controlled. A beam splitter separates the light in two paths. On the sample arm, a tube lens forms an image onto a CMOS camera. On the Fourier arm, a second 4f system creates an image of the angular profile of the illumination onto a second CMOS camera. This image contains at once information regarding the source profile S and the pupil function P, which can be used for the calculation of the phase transfer function, ensuring that the simulations represent the actual configuration of the setup.

The illumination setup is shown in detail in Fig. 3.6. In order to obtain a uniform illumination of the sample plane, with a half ring angular profile, a glass diffuser is located in the Fourier plane of the 4f system. The glass is partly covered with black tape, such that the profile is shaped as a half ring, where the outer radius corresponds to the radius of the glass diffuser. This partially obstructed diffuser serves both goals of uniform intensity and asymmetric illumination. By having the sample plane exactly at the image plane of the illumination 4f system, we obtain an illumination profile whose Fourier transform looks like the half ring diffuser. To change the size of the half ring profile, it is sufficient to change the second lens of the 4f system with one with a different focal length, as shown in Fig. 3.6. In the case on the left, the two lenses are equal, so the Fourier transform of the illumination at the sample plane would give the same shape of the half ring diffuser. In the case on the right, a lens with a longer focal length is used, so the Fourier transform of the illumination at the sample plane would be a shrunk version of the half ring diffuser. By switching between different lenses, I can obtain several ring sizes, while maintaining the ratio of the inner radius to the outer radius.
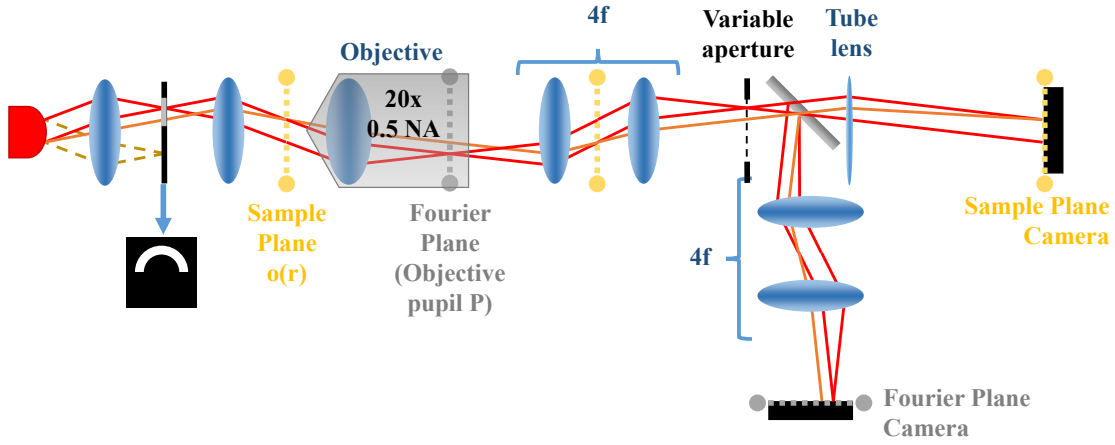
Figure 3.5: The microscope setup. Yellow dashed planes are conjugated with the sample plane, while grey dashed planes are conjugated with the Fourier plane.
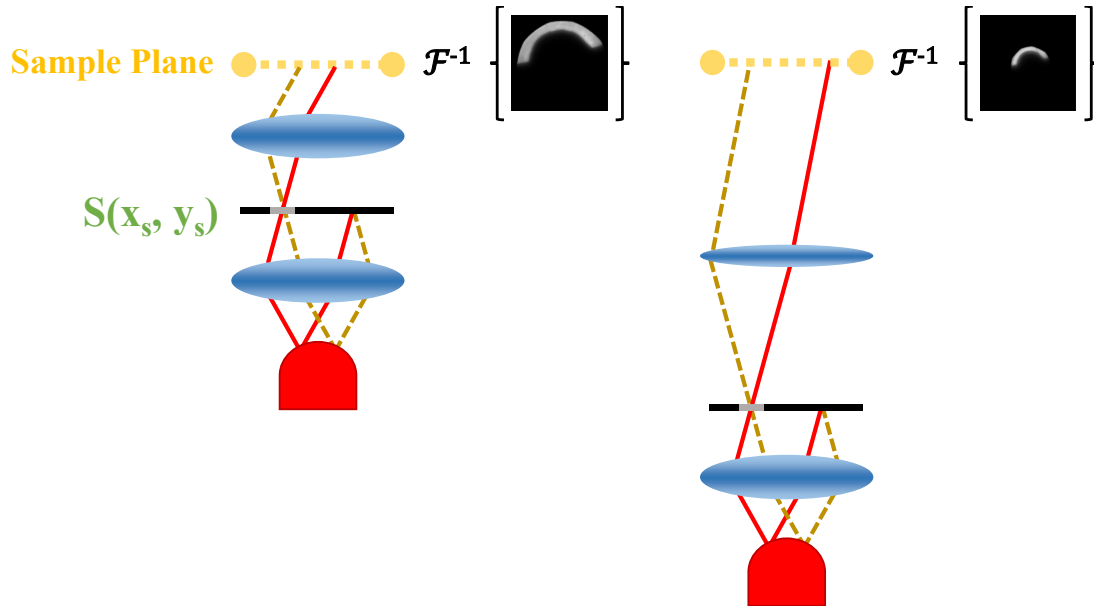
Figure 3.6: The illumination configuration. The output of an LED is imaged onto the sample plane using a 4f system. A diffusing glass is located at the Fourier plane of this system. The glass is partially obstructed with black tape to form a half ring illumination. Thanks to the diffusing properties of the glass, the illumination at the sample plane is uniform. By using lenses with different focal length, it is possible to achieve several scaled versions of the same angular profile.
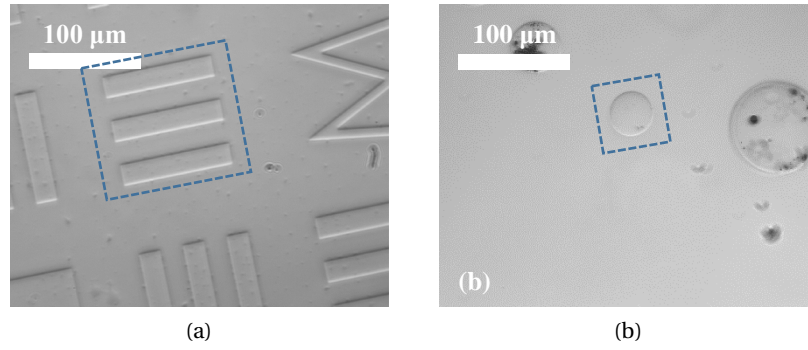
Figure 3.7: (a) USAF target etched in glass. (b) Glass microbeads immersed in index-matching oil. The blue dashed squares represent the regions of interest of each sample.

3.3.2 Contrast trend for increasing Numerical Aperture

The setup described in the previous section was used to collect measurements of different samples under varying conditions of illumination and collection. The lenses in the illumination setup were used to create several illumination profiles of different angular aperture. The first lens and the diffusing glass were kept in fixed relative position, while lenses of increasingly long focal length were used to focus the illumination on the sample. The illumination system was shifted vertically so that its focal plane would always correspond to the sample plane. At the same time, the aperture located in the relayed BFP of the objective was decreased to match the microscope NA to the maximum angle of the illumination. In this way, a set of measurements was obtained in which all the illumination and collection parameters would be maintained, except for the NA.

For each configuration, two images were taken: one image of the sample on the sample camera and, after having removed the sample, one image of the illumination profile on the Fourier camera. In particular, two samples are considered here: a USAF target etched in glass, and glass microbeads in a layer of immersion oil (IMMOIL-F30CC, by Olympus). These samples are shown in Fig. 3.7. The USAF target falls in the category of sharp objects, while the glass microbeads are representative of the smooth object category. In all cases, for each illumination configuration the normalized contrast was computed, according to Eq. 3.5. These contrast values were further normalized to the maximum of each series, so that changes in contrast can be read in relative terms. The results are shown in Fig. 3.8 and Fig. 3.9.

The data in Fig. 3.8 shows that the contrast varies between approximately 85% and 100% of the maximum value. From the simulations of Fig. 3.3 (c), it is expected to observe an almost constant contrast, which is not the case in the experiment. This can be explained by the non-uniform thickness of the illumination half ring, which has a strong impact on the contrast as shown in Fig. 3.3 (d). To verify the validity of this measurement, a corresponding simulation was performed. In order to reproduce faithfully the configuration of the experiment, I reconstructed the USAF target using an inversion algorithm with Tikhonov regularization [24], and I processed this image to obtain a thresholded mask in which I assigned the value of
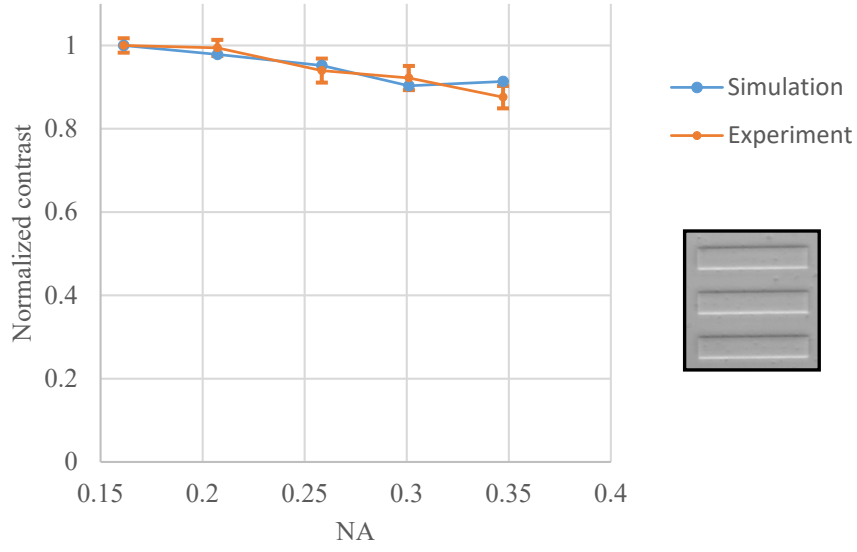
Figure 3.8: Normalized contrast for varying NA_{obj} for the USAF sample of Fig. 3.7 (a). The blue line represents the simulated contrast, while the orange line represents the experimental contrast. Error bars for the experiment indicate the standard deviation of the contrast over several measurement. The ROI considered is shown in the inset.

Figure 3.9: Normalized contrast for varying NA_{obj} for the glass microbead sample of Fig. 3.7 (b). The blue line represents the simulated contrast, while the orange line represents the experimental contrast. Error bars for the experiment indicate the standard deviation of the contrast over several measurement. The ROI considered is shown in the inset.

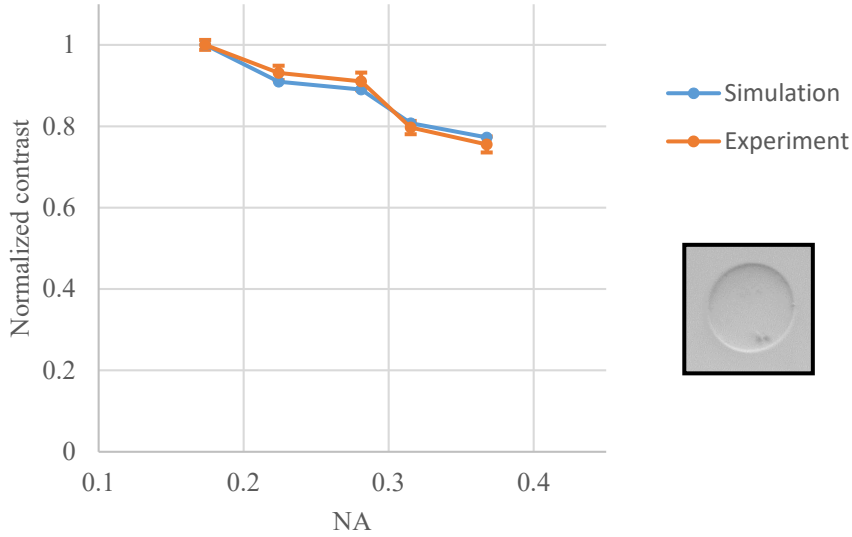0 mrad to the background and the nominal phase value of 685 mrad to the USAF structure. This nominal object was smoothed with a Gaussian filter of standard deviation $\sigma = 2$ to suppress overshoot caused by the Gibbs effect, without excessive distortion of the nominal rectangular shape. Moreover, an image of the illumination profile obtained on the Fourier plane camera was used to calculate the phase transfer function, according to Eq. 3.2. The result of this simulation is also displayed in Fig. 3.8, and shows a good agreement with the measurements: similar variations of contrast are present in both simulation and experiment. The use of a measured illumination profile for simulations allowed to correctly account for shape deviations from the half-ring. The differences in exact values might be due to the estimation of the NA for each case: indeed, due to the polygonal shape of the variable aperture placed in the relayed BFP, it was necessary to calculate an average aperture radius.

Similarly, the experimental and simulation data for the glass microbead sample of Fig. 3.7 (b) are shown in Fig. 3.9. In order to generate accurate simulations, it is necessary to have a nominal sample structure. The diameter of the bead was measured directly from the image, thanks to the known scale of magnification, to be 39 μm. The exact refractive index of these beads is unknown, so it was estimated by taking several DPC images of the bead immersed in oil mixes with varying refractive indices. The refractive index of these oils is very sensitive to temperature changes, so all measurements were performed in a temperature controlled room, and repeated several times. From each image, I measured the contrast, and I interpolated the results to find the refractive index at which the contrast fell to 0. With this approach, the refractive index of the beads was estimated to be 1.5197.

In this experiment, I reduced the phase difference introduced by this bead, by immersing it in microscopy oil (IMMOIL-F30CC, by Olympus) whose refractive index at our wavelength of interest was estimated to be 1.5163. Thus, for the simulations, a spherical object with a nominal phase of 1.33 rad was used. The results of both simulation and experiment are shown in Fig. 3.9. The expected decreasing trend of contrast versus numerical aperture of Fig. 3.3 (c) is clearly visible, and the experimental values match the corresponding simulation.

3.3.3 CNR simulation and sensitivity estimation

Given the agreement between simulations and experiment for the contrast in DPC images, it is left to verify whether the simulation algorithm is accurate enough also at very low phase values, and if the noise model can provide the correct CNR values, for both types of samples. For this experiment, I used the same approach described in the previous section to record several DPC images for varying NA.

First I used a glass USAF target, which has a height of 12nm as measured with Atomic Force Microscopy (AFM); given the refractive index of glass and air, at the wavelength of our LEDs, this sample introduces a phase difference of 55.34 mrad. An example of a single DPC image of this sample is shown in Fig. 3.10 (a). The contrast of this image is stretched for better visualization, which makes the grainy noise pattern apparent. Nevertheless, with four images obtained with illumination shifted at 90° intervals (the remaining three are not shown here) it is still possible to reconstruct the phase object. The reconstructed phase was again
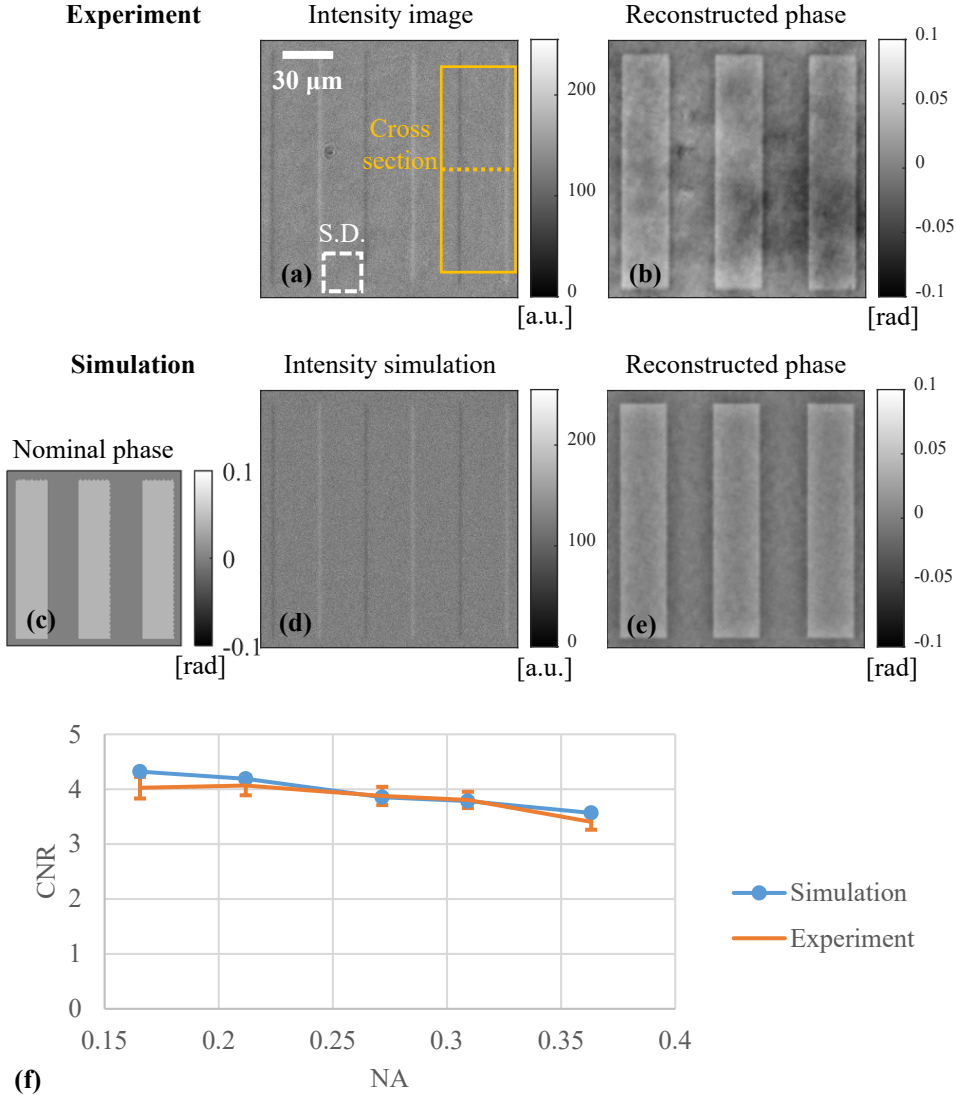
Figure 3.10: (a) Single DPC image of a USAF target with phase difference of 55.34 mrad, imaged in the setup with NA_{obj}=0.19. (b) Corresponding phase reconstruction performed with 4-axis illumination. (c) Phase object used for simulation, representing the same portion of USAF target from the experiment. (d) Simulated image for the same illumination and collection conditions as in (a). Noise is added using the algorithm proposed by Foi et al. [49, 50]. (e) Phase reconstruction from 4-axis simulated DPC images. (f) CNR calculated for both simulation and experiment at several NA_{obj} values. In order to calculate the CNR, a low noise cross-section was obtained by averaging the DPC image in the vertical direction, as shown in (a): the yellow square shows the ROI, and the dotted yellow line shows the direction of the cross section. The maximum and minimum of the cross section are used to compute the contrast. For the noise, the standard deviation of a featureless area was computed, shown in white in (a). The CNR is then calculated using Eq. 3.4. This process is repeated to obtain the data points in (f).
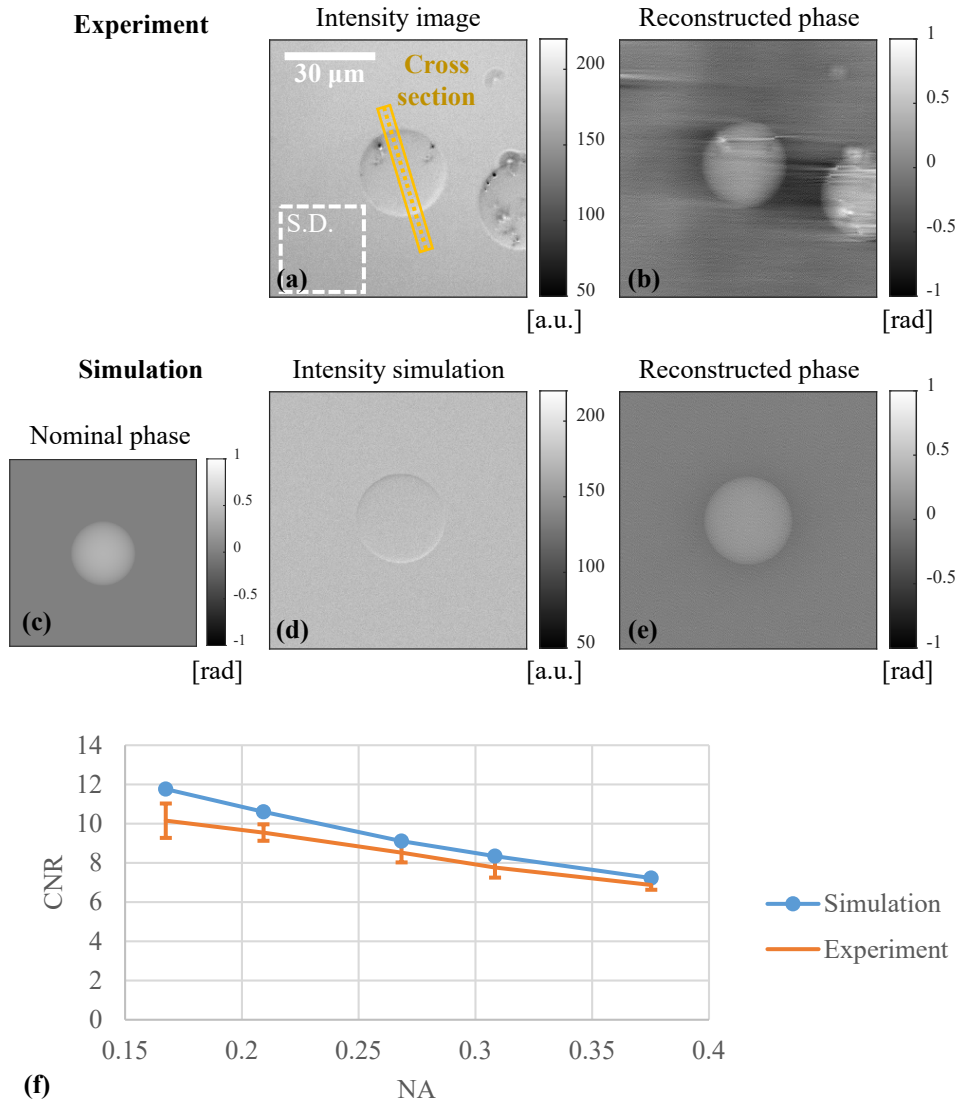
Figure 3.11: (a) Single DPC image of a glass microbead immersed in oil, giving a maximum phase difference of 463.4 mrad, imaged in the setup with NA_{obj}=0.375. (b) Corresponding phase reconstruction performed with 4-axis illumination. (c) Phase object used for simulation, representing the same bead size and refractive index mismatch from the experiment. (d) Simulated image for the same illumination and collection conditions as in (a). Noise is added using the algorithm proposed by Foi et al. [49, 50]. (e) Phase reconstruction from 4-axis simulated DPC images. (f) CNR calculated for both simulation and experiment at several NA_{obj} values. In order to calculate the CNR, a low noise cross-section was obtained by averaging the DPC image as shown in (a): the yellow square shows the ROI, and the dotted yellow line shows the direction of the cross section. The maximum and minimum of the cross section are used to compute the contrast. For the noise, the standard deviation of a featureless area was computed, shown in white in (a). The CNR is then calculated using Eq. 3.4. This process is repeated to obtain the data points in (f).

used to draw a theoretical phase object, as described in Section 3.3.2, to use in the following simulations, shown in Fig. 3.10 (c). The resulting simulated image, with added noise, is shown in Fig. 3.10 (d). Due to the highly noisy nature of these images, in order to compute the grey levels of the maximum and minimum, I first averaged in the vertical direction to obtain a single low-noise cross section from which to extract the contrast. The noise was instead calculated as the standard deviation over a 100x100 pixel area where no features are present, highlighted in white in Fig. 3.10(a) [46, 47]. The area is chosen close to the Region of Interest (ROI), such that the background intensity is uniform. The resulting CNR values for several NAs are shown in the plot of Fig. 3.10(f), for both simulation and experiment. The results are in good agreement, and show that this sample is very close to the sensitivity limit, since it gives a CNR between 3.5 and 4 over the NA_{obj} range.

Similarly, I prepared a low-CNR smooth sample using glass beads. In this case, I immersed the bead in an oil with a refractive index of 1.519, to obtain a much lower phase. Given the bead diameter of approximately 30.29 μm and the refractive index difference, this sample should introduce a maximum phase difference of approximately 463.4 mrad. As for the previous sample, I measured the CNR as the ratio between the amplitude of the phase object and the standard deviation of an empty area, shown in Fig. 3.11 (a). We tested that it was indeed possible to invert this object, and obtained a sphere of approximately 0.45 rad, shown in Fig. 3.11 (b). Following the same steps of the previous experiment, I generated a noisy image of this nominal sample; the nominal object, simulated image and simulated reconstruction are shown in Fig. 3.11 (c-d-e), respectively. The CNR computed for both simulation and experiment is displayed in Fig. 3.11 (f): the trend is correctly predicted by the simulation. The slight mismatch is due to an incorrect assumption of the refractive index of the immersion medium. Indeed, it is well known that the refractive index of oils is temperature dependent: as an example, the refractive index liquid # 1809 by Cargille, used to make the medium for this experiment, has a temperature coefficient of $-0.000418 dn_D/dt$.

Given the refractive index difference between beads and medium in this experiment, a temperature drift of 1° would already cause a 90 mrad change in phase, which would account for a change in contrast. Moreover, as explained in Section 3.3.2, the refractive index of the beads has been estimated using similar oil mixes, thus the overall error on the nominal phase may equally come from an error on the beads refractive index.

The noisy image simulation can now be used to extrapolate the sensitivity limit, according to the procedure described in Section 3.2.2. The sensitivity limit is computed for several NAs and for both samples, based on the CNR simulations. The results are displayed in Fig. 3.12. It is expected that the result should be different for different types of samples, based on their spatial spectrum. According to the simulations, USAF targets with phase differences lower than 20 mrad can be measured in this DPC setup, and the sensitivity remains somewhat constant over the whole range. For the microbeads, the sensitivity is 85 mrad for the smallest NA_{obj}, and up to 140 mrad for the higher NA_{obj} value. In this case, the sensitivity for the smooth object is up to seven times worse than for the sharp object. This can be explained with how the frequency spectrum of these two objects overlap with the phase transfer function, as detailed in Section 3.2.1.
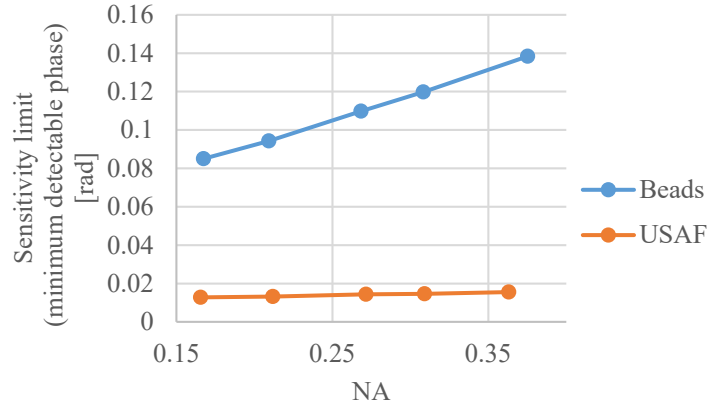
Figure 3.12: Sensitivity simulation at several NA values, for the USAF target and the glass microbead.

3.4 Conclusion

The first part of this chapter focused on the parameters that influence the phase contrast in DPC. Assuming a half ring illumination, it was observed that the NA of the system and the inner radius of the ring have an impact on the resulting phase contrast. With simulations and experiments, it was noted that this effect can be strikingly different based on the sample under observation: in particular, decreasing the NA can help increasing the contrast for samples whose spatial frequency spectrum is mostly low-frequency, as observed in Fig. 3.3. This is an important factor to keep in mind when planning the parameters for a DPC setup. If the goal is to obtain highly sensitive measurements, it might be necessary to trade off contrast and resolution. A system with variable NA can provide the flexibility to adapt to the needs of each measurement.

The second goal was to develop an approach to provide preliminary prediction of sensitivity for a given setup and sample. It was demonstrated that it is sufficient to know the main optical parameters of the setup, and to model the main source of noise [49, 50] to test the sensitivity performance of a system. Since no actual DPC images are necessary for this calculation of sensitivity, this algorithm can be used in the design stage of a DPC microscope, to help choose the best illumination profile and camera for the goal. A synthetic sample of choice can be used in the simulation to precisely evaluate the sensitivity in the specific use-case scenario, and the user can verify whether their expectations are realistic. Our simulations showed that with a simple, 8-bit CMOS camera, it is possible to reach a sensitivity above 1nm of OPL.

Other phase microscopy techniques, especially those based on interferometry, demonstrated spatial phase sensitivity, from 0.7 nm down to 0.14 nm [56–58]. On the other hand, these techniques require more sophisticated hardware and software, or are slower due to components like liquid crystal modulators [58].

Still, it is possible to increase sensitivity in DPC, for example by employing higher end cameras with a bigger well capacity or with more bits for encoding, thus decreasing the impact

of shot noise. This is because a background intensity close to the dynamic range limit of the camera optimizes the ratio $I/\sqrt{I}$ of the SNR due to shot noise. Indeed, the LEDs that I employed in my experiments had to be used well under their maximum rated driving current, as the camera pixels were otherwise saturating even at short exposure time. With a bigger well capacity, more of this available power can be used, without incurring in saturation. For two cameras with different saturation levels $I_{\text{sat},2} > I_{\text{sat},1}$, where the subscripts 1,2 refer to the two cameras, if we illuminate both detectors close to saturation, we would gain a factor of $\sqrt{I_{\text{sat},2}/I_{\text{sat},1}}$. Using a thinner ring of illumination increases contrast thus allowing to reach better sensitivities, and for smooth samples, decreasing the NA can be a solution if within the resolution need. As pointed out in Section 3.2.3, using multiple images at different illumination conditions also allows to reconstruct samples with single-image CNR<1. The conditions and number of images needed should be investigated with a similar approach as shown here for the forward problem.

Finally, the sensitivity simulation approach demonstrated here, can be easily translated to other imaging techniques. Imaging systems that can be linearised, for example according to the Born approximation, can be analysed in a similar manner, but also other types of models can be adapted, since only the forward model is used here [6]. Moreover, extensions to absorptive and 3D samples are interesting future applications [59].

4 Beyond the sensitivity limit: lock-in DPC

The content of this chapter is based on the paper: C. Bonati, D. Loterie, T. Laforest, and C. Moser, "Lock-in incoherent differential phase contrast imaging," *Photon. Res.*, vol. 10, 237-247(2022).

4.1   Introduction

In the previous chapter, it was shown that the phase sensitivity is limited to several tens of mrad [60], which prevents applications where extreme phase sensitivity is required, such as the optical imaging of action potentials, where interferometric techniques still dominate [61–66].

Several steps can be taken to maximize contrast and improve sensitivity. For example, blocking light coming from low angles can increase the contrast by up to a factor of two [60]. Another approach is to average multiple frames, but this comes at the cost of speed and makes real time recording much more data intensive: the sensitivity only improves as the square root of the number of frames.

Finally, sensitivity can be improved by increasing the power of the illumination source, as the phase image is proportional to the total light intensity [24]. On the other hand, the background is also proportional to the illumination power, and for small phase modulations the background component can saturate the detector before significant sensitivity improvement is achieved. While detectors with larger well capacity can be used to extend the dynamic range, these usually have much larger pixels, thus sacrificing either spatial resolution or field of view.

In this chapter, I explore a new approach to DPC, based on lock-in amplification to directly measure the amplitude of phase modulation, produced by alternating mirrored illuminations. Using a so-called lock-in camera (heliCam®, Heliotis), I demonstrate how it is possible to obtain high-contrast, background-free, full field DPC images. Other advantages of this technique include a reduced amount of data to be collected, rejection of out of frequency modulations, and optimized use of the dynamic range. Comparative measurements of weak phase transparent samples in standard and lock-in DPC are used to show the improvement given by the proposed technique.

4.2 Theory

Let us start once more from the DPC image formation equation, for a phase only object:

$$\tilde{I}(\vec{u}_i) = B\delta(\vec{u}_i) + H_{\mathrm{ph}}(\vec{u}_i)\tilde{\phi}(-M\vec{u}_i)\,. \tag{4.1}$$

This equation refers to a single image being recorded by a detector, so no time dependence is included.

If the source profile is modulated over time, the intensity will also change accordingly. Typically, in DPC the source profile will switch between two or more mirrored profiles. This modulation can be periodic, for example:

$$S(\vec{u}, t) = \begin{cases} S(\vec{u}) & \text{for } 0 + kT \leq t < \frac{T}{2} + kT \\ S(-\vec{u}) & \text{for } \frac{T}{2} + kT \leq t < T + kT \end{cases}. \tag{4.2}$$

The time-dependent image would then be:

$$\tilde{I}(\vec{u}_i, t) = \begin{cases} B\delta(\vec{u}_i) + H_{\mathrm{ph}}(\vec{u}_i)\tilde{\phi}(-M\vec{u}_i) & \text{for } 0 + kT \leq t < \frac{T}{2} + kT \\ B\delta(\vec{u}_i) - H_{\mathrm{ph}}(\vec{u}_i)\tilde{\phi}(-M\vec{u}_i) & \text{for } \frac{T}{2} + kT \leq t < T + kT \end{cases}. \tag{4.3}$$

The quantity of interest is, in this case, the amplitude of the modulated term. In standard DPC this component is isolated from the background by recording a frame for each illumination state, and computing the difference between the two frames, such that $\tilde{I}_{\mathrm{DPC}}(\vec{u}_i) = 2H_{\mathrm{ph}}(\vec{u}_i)\tilde{\phi}(-M\vec{u}_i)$. This procedure digitally removes the background, but the single raw measurements still contain it. If the modulated term $2H_{\mathrm{ph}}(\vec{u}_i)\tilde{\phi}(-M\vec{u}_i)$ is big enough compared to the background, this is not an issue, but if the sample is too weak, the dynamic range of the detector will not be able to accommodate at the same time a powerful background and a weak modulation. Indeed, both the phase transfer function and the background term depend on the source profile and the pupil, thus any increase of the modulated term comes with an increase of the background, which might cause saturation.

In order to circumvent this problem, it is necessary to use a scheme that directly demodulates the amplitude of $H_{\mathrm{ph}}(\vec{u}_i)\tilde{\phi}(-M\vec{u}_i)$, for example using lock-in amplification. A classic lock-in detector has a single point, so it would require a scanning confocal optical system in order to obtain a full image. Clearly, this would impact the complexity and speed of the system, which is not an ideal solution.

An alternative option is to use a detector with "smart pixels", which incorporate special electronics to perform more advanced analog operations. One such detector is Heliotis' heliCam C3, which is a detector based on CMOS technology, and whose pixels contain signal demodulation circuitry [67–70]. The demodulation stage is based on I-Q direct detection, schematically depicted in Fig. 4.1 (d) [68]. The camera outputs the frames I and Q, which are the demodulated amplitudes of the input signal multiplied by discrete quadrature signals from the local oscillator. From these demodulated frames one can then calculate the signal amplitude and phase as:
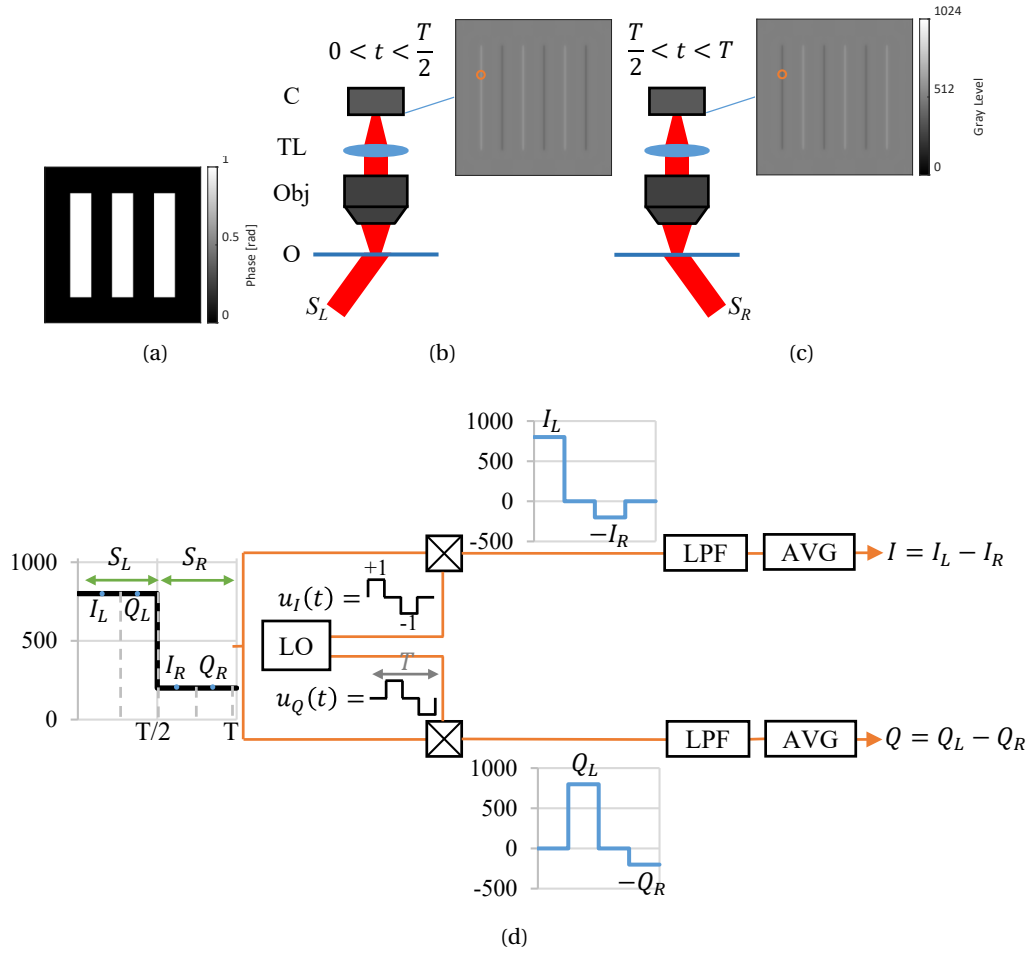
Figure 4.1: Scheme of operation of lock-in DPC with two illuminations. (a) Simulated phase sample; (b) Simplified DPC microscope scheme during the first half period; the left source S_L illuminates the object (O), the transmitted light is collected by the objective (Obj) and an image is formed by the Tube Lens (TL) on the camera (C); on the right, simulated DPC image generated with this illumination; (c) simplified DPC scheme during the second half period, using the right source S_R; on the right, simulated DPC image generated with this illumination; (d) scheme of operation of a heliCam C3 pixel. The signal modulated at frequency 1/T is integrated and sampled four times during each period. The local oscillator (LO) generates two discrete signals: u_I is a periodic sequence of [+1, 0, -1, 0], and u_Q is the same signal phase shifted by 90°. Discrete multiplication is performed between the sampled signal and each of the two local oscillator signals. The resulting signals are then low pass filtered (LPF) and averaged in time (AVG), giving at the output the frames I and Q, which are digitized by a 10-bit ADC. To synchronize with the DPC illumination, the two sources S_L and S_R are switched on and off alternatively over a period T equal to the demodulation period of the lock-in camera. Four samples are taken during one cycle: two while the source S_L is on (I_L and Q_L) and two while the source S_R is on (I_R and Q_R). If the illumination switches in phase with the local oscillator, I and Q are equal.

$$A = \sqrt{I^2 + Q^2}\,, \tag{4.4}$$

$$\phi = \arctan2(I, Q) - \frac{\pi}{4} \tag{4.5}$$

This type of detector can be used to obtain DPC images according to the scheme of Fig. 4.1. Let us assume that the sample under observation is the simulated phase sample depicted in Fig. 4.1(a). When the sample is illuminated with the left source as in Fig. 4.1(b), the image at the camera would be as shown to the right of the scheme. Under right source illumination, the resulting image would be as in 4.1(c). We can focus our attention on the intensity received by the pixels on the left-most rectangle edge, highlighted in the orange circle in Fig. 4.1(b, c). If the light sources are switched over a period T, tracking the intensity received by the pixels of interest would give a plot such as shown on the left in Fig. 4.1 (d). This is the input light modulation at the detector.

The lock-in camera integrates four samples from the input signals, each with a duration of one quarter of the local oscillator period. The key to performing lock-in DPC is to set the light switching period to be equal to the local oscillator period, and to make sure that they are synchronized in phase. In this way, the first two samples (I_L and Q_L) are obtained during the left illumination, while the last two samples (I_R and Q_R) are obtained during the right illumination. Moreover, I_L and Q_L are equal, as well as I_R and Q_R.

The local oscillator generates two periodic signals with period T, u_I and u_Q, which are a sequence of [+1, 0, -1, 0], and are shifted in phase by 90° with respect to each other. These two periodic signals are multiplied with the four input samples, giving the two quadrature signals in blue in 4.1(d). The last stages are low-pass filtering and averaging, after which two single frames, I and Q, are output by the camera.

Unlike applications such as optical coherence tomography, in this case the only quantity of interest is the amplitude of the signal. Moreover, if timing of the illumination has been done correctly, I and Q are identical, and from Eq. 4.5 the phase between them is always zero. Since we also need to preserve information on the positivity and negativity of pixel values with respect to the background, which would be lost with Eq. 4.4, the lock-in DPC image is calculated simply as the sum of I and Q.

4.2.1 Phase sensitivity

As seen in Chapter 3, sensitivity in DPC can be calculated from the CNR. If shot noise is the dominating noise source [49, 53], it is possible to approximate the CNR as [50, 51, 60]:

$$\mathrm{CNR} \propto \frac{\mathfrak{F}^{-1}\{2H_{\mathrm{ph}}(\vec{u}_i)\tilde{\phi}(-M\vec{u}_i)\}}{\sqrt{B}}\,. \tag{4.6}$$

Let us now rewrite this expression in terms of source power. The source term S can be expressed as the product between the total power K and the normalized source, which depends on the direction $\vec{u}_s$ of the emitted photons:

$$S(\vec{u}_s) = K \cdot S_{\text{norm}}(\vec{u}_s) \,, \tag{4.7}$$

where:

$$K = \iint S(\vec{u}_s) d^2 \vec{u}_s \,, \tag{4.8}$$

$$\iint S_{\text{norm}}(\vec{u}_s) d^2 \vec{u}_s = 1 \,. \tag{4.9}$$

If we assume that the support of S is entirely contained in the support of the pupil P, which is normally the case in DPC, then from Eq. 2.16 we can see that $B = K$. The same normalization can be also done for H_{ph}, so that:

$$H_{\text{ph}}(\vec{u}_i) = B \cdot H_{\text{ph,norm}}(\vec{u}_i) \,, \tag{4.10}$$

where $H_{\text{ph,norm}}$ is the phase transfer function normalized to one. By inserting Eq. 4.10 in Eq. 4.6, we obtain:

$$\text{CNR} \propto \sqrt{B} \mathfrak{F}^{-1} \left\{ 2 H_{\text{ph,norm}}(\vec{u}_i) \tilde{\phi}(-M\vec{u}_i) \right\} . \tag{4.11}$$

It is indeed possible to increase the CNR by simply increasing the incident power, but in standard DPC the maximum CNR is limited by saturation of the pixels.

The CNR of Eq. 4.11 holds equally for the lock-in scheme. In this case, the maximum CNR can be limited in three ways:

1. the source has reached its maximum power and cannot be further increased;

2. the modulation is saturating the pixels, in which case the maximum CNR is reached;

3. the background term between the two illuminations is not identical, and their difference $B_L - B_R$ saturates the pixels.

In our current implementation, this last case turned out to limit the CNR improvement the most. While the average background power can be easily tuned, non-uniformities in the illuminations are going to be different. We define the single-shot CNR improvement as the ratio between the maximum lock-in CNR and the maximum standard CNR, for the same sample. Let us first write the CNR limit for the standard method, using Eq. 4.11. The most simple way to improve the CNR is by increasing the background intensity B; this is of course limited by the well capacity of a pixel, W, since higher intensities would saturate the image making any analysis impossible. This means that the theoretical maximum standard CNR is:

$$\text{CNR}_{\text{s,max}} \propto \sqrt{W} \mathfrak{F}^{-1} \left\{ 2 H_{\text{ph,norm}} \tilde{\phi} \right\} . \tag{4.12}$$

Of course this is a limit case, since non-uniformity and phase structures may increase the intensity in some pixels at the saturation level. Let us now express the amplitude of the background non-uniformity as a percentage r of the background B_S, as shown in Fig. 4.2(a).
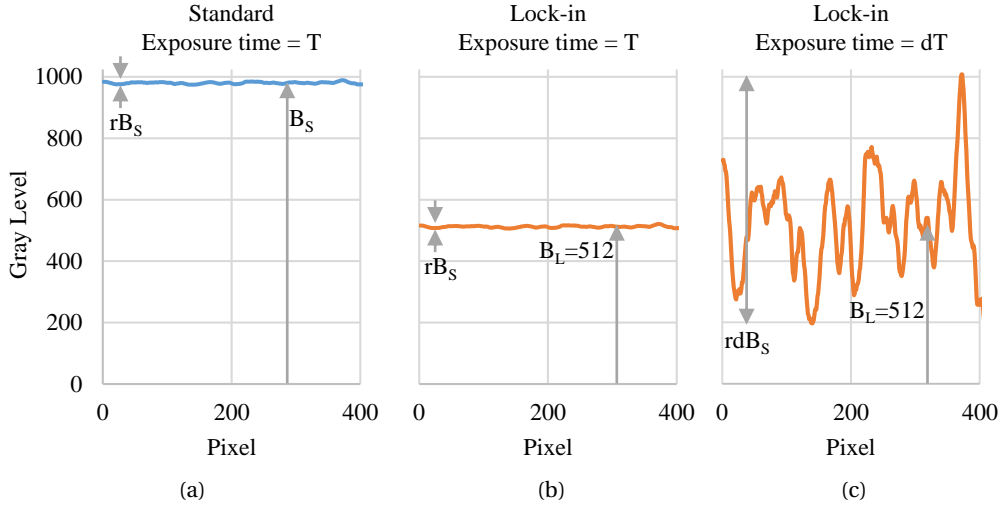
Figure 4.2: (a) Simulated pixel values along a cross-section, for standard DPC image recorded over an exposure time T. B_S indicates the background value, close to the limit of 1024 in the case of a 10 bit detector; rB_S indicates the amplitude of the background non-uniformity. (b) Simulated pixel values along the same cross-section, for a lock-in DPC image recorded over an exposure time T. B_L indicates the background value, which is approximately 512 if the left-right illuminations are tuned to have the same average power; the non-uniformity is still rB_S. (c) Simulated pixel values along the same cross-section, for a lock-in DPC image recorded over an exposure time d times longer than before. The background is still 512 assuming well-tuned illuminations, but the non-uniformity is now increased by the same factor d as the exposure time.

In the lock-in case, for the same exposure time T, the cross section would look as in Fig. 4.2(b), where the background B_L is approximately 512: if the left and right illuminations are properly tuned to have the same average intensities, there would be no modulation over time, and the camera maps this to the mid-level of the scale. The non-uniformity here is still rB_S. In this case though, none of the pixels are close to saturation, so we can safely increase the exposure time, thus improving the CNR. If we increase the exposure time by a factor d, the non-uniformity also increases by the same factor, as depicted in Fig. 4.2(c). Clearly in this situation, the limit is reached when the amplitude of non-uniformity equals the maximum gray level W, so we can write:

$$d_{\max} r B_s = W \Rightarrow d_{\max} = \frac{W}{r B_s}, \tag{4.13}$$

$$\text{CNR}_{\text{L,max}} \propto \sqrt{d_{\max} B_s} \mathfrak{F}^{-1}\left\{2 H_{ph,\text{norm}} \tilde{\phi}\right\} = \sqrt{\frac{W}{r}} \mathfrak{F}^{-1}\left\{2 H_{\text{ph,norm}} \tilde{\phi}\right\}. \tag{4.14}$$

As a consequence, the maximum CNR improvement is given as:

$$\frac{\text{CNR}_{\text{lock-in}}}{\text{CNR}_{\text{standard}}} = \frac{1}{\sqrt{r}}. \tag{4.15}$$

For incoherent sources such as those in our setup, a uniformity level of 1% of the average intensity is presently state-of-the-art [71]. As a consequence, with our current implementation we can expect in practice a maximum improvement in sensitivity by an order of magnitude.

In the lock-in camera by Heliotis, we can set the demodulation period, $T_{\text{lock-in}}$, and the number of cycles that are averaged before a frame is obtained, m, which is a minimum of four. During this acquisition time of $m T_{\text{lock-in}}$, the two frames I and Q are obtained, which are summed as they are identical, thus the equivalent exposure time of DPC is given by:

$$T_{IQ} = \frac{m T_{\text{lock-in}}}{2}. \tag{4.16}$$

In standard DPC, we collect the two images I_L and I_R, with an exposure time of T_{LR} for each. To obtain the DPC image, these two are subtracted. As shown before, both standard and lock-in DPC CNR is governed by Eq. 4.11, which is also proportional to the square root of the total number of photons integrated by the detector:

$$\text{CNR} \propto \sqrt{NT}, \tag{4.17}$$

where T is the exposure time and N is the photon rate. If the power of the sources is maintained the same for both standard and lock-in DPC experiments, then we can expect the improvement of CNR as:

$$\frac{\text{CNR}_{\text{lock-in}}}{\text{CNR}_{\text{standard}}} = \sqrt{\frac{T_{IQ}}{T_{LR}}}. \tag{4.18}$$

In the following, I will verify this ratio.

4.2.2 Reconstruction

A key step of DPC is the reconstruction of a quantitative phase map of the sample. In order to do this, the DPC image is normalized by the background factor B [24], so that the result of the reconstruction is directly expressed in units of radians. Usually the factor B is simply calculated as the sum of the two images with opposite illuminations, since the phase modulation should cancel out. This is not possible in lock-in DPC, where the demodulated phase is directly obtained and the separate images I_L and I_R are not measured.

A simple way to circumvent this issue is to record a single standard DPC image, to use as reference. The heliCam lock-in camera allows to record images also as a standard detector. The sources are always driven at their maximum power, which means that the total exposure time in standard DPC has to be much shorter than in lock-in DPC, due to the saturation caused by the strong background. Similarly to the CNR ratio in Eq. 4.18, the background ratio is equal to the exposure time ratio, thus we can write:

$$B_{\text{lock}-\text{in}} = \frac{B_{\text{standard}} T_{IQ}}{T_{LR}} \; . \tag{4.19}$$

This estimated background will be used to reconstruct quantitative phase in lock-in DPC. In this chapter, the method of Tikhonov inversion [24] is used to reconstruct the phase sample from the DPC images.

4.3 Experimental validation

4.3.1 Setup

Microscope

The microscope DPC setup is shown in Fig. 4.3. It consists of a classic DPC microscope setup, with the addition of an extra 4f system to relay the pupil located inside the objective barrel. In order to control the NA of the setup, a variable aperture is located at the relayed pupil. After the aperture, a beam splitter separates the light in two paths: on the transmitted path, a tube lens forms an image of the sample at the lock-in camera; on the reflected path, a second 4f system is used to form an image of the pupil plane on a secondary camera. This image represents the illumination profile within the boundaries of the pupil, and will be used to calculate the phase transfer function for phase reconstruction [60].

The helicam C3 detector features 300x300 pixels with a 40x40 μm spacing. The fill factor is 50% or more thanks to a microlens array. It can demodulate signals at a frequency of up to 250 kHz, but the maximum frame rate is 3800 fps. The frames are digitized over 10 bits. The microscope's field of view has a size of 600x600 μm, while the pixel size limits resolution to 2μm.

Illumination

Several strict requirements have to be met for the illumination of the lock-in DPC setup. In order to ensure the maximum field of view with unsaturated pixels, the background subtraction provided by lock-in only works if the switching illuminations have equal distributions in the object plane. Therefore, it is necessary to build a system that is able to match and align these light distributions to a high degree of accuracy. Moreover, high efficiency in light delivery is necessary, so that enough power is available to take advantage of the lock-in scheme. Finally, the NA should be as close as possible to that of the objective, in order to maximize contrast [45, 60].

Considering these conditions, I opted to use two high power red LEDs, with approximately 120° emission angle. Their emission area is obstructed by electrodes which lead to an inhomogeneous light profile, so it is not possible to directly image them onto the object plane. Among various options to even out the illumination, the use of a hexagonal light pipe was chosen (Edmund Optics, # 63-080 N-BK7 Hexagonal Light Pipe). These light pipes can homogenize non-uniform light thanks to total internal reflection, so that the output facet
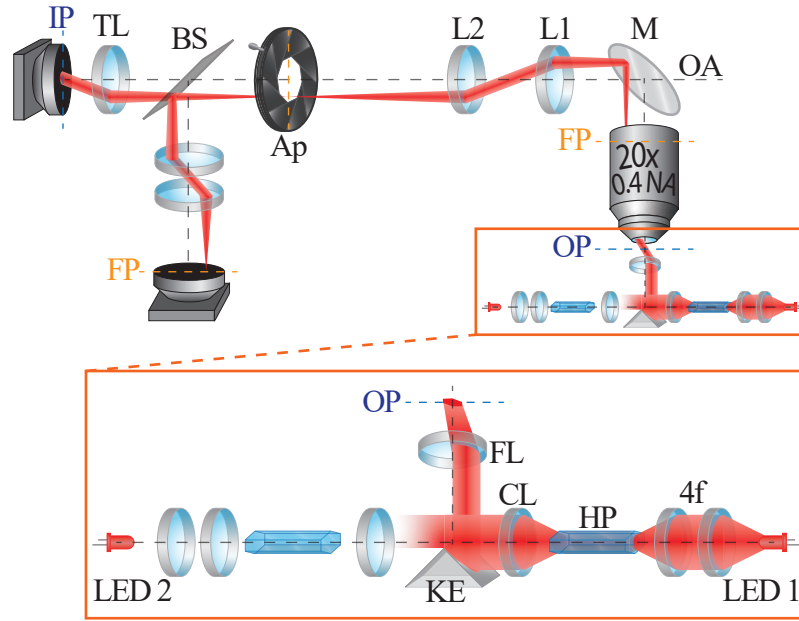
Figure 4.3: Lock-in DPC microscope setup. The sample is located at the object plane (OP) of the objective (20x, 0.4 NA) and illuminated with red LED light (LED Engin LZ1 623 nm). The pupil (FP) of the objective is located inside the objective barrel (yellow dashed line) and is relayed with a 4f system (lenses L1 and L2, two identical 180 mm focal length lenses, with 2" diameter). A variable aperture (Ap) is located at the relayed pupil to adjust the system's NA to the maximum illumination angle. With a tube lens (TL, a 200 mm focal length lens, matched to the objective's specifications) an image is formed at the image plane (IP) where the lock-in camera is located. A beam splitter (BS) is used to form a second arm: there, a second 4f system forms an image of the pupil onto a standard CMOS camera. The zoomed inset shows the scheme of the illumination part of the setup. The light coming from a high power red LED is focused with a 4f system onto the facet of a hexagonal glass pipe (HP). The light going through this glass pipe is reflected several times and gets scrambled, lighting the output facet with uniform intensity. A knife-edge mirror (KE) is placed at the back focal plane of a collimating lens (CL). This mirror has two reflecting surfaces at a 90° angle, and the edge is also reflecting. This mirror is placed such that the edge crosses the optical axis at the back focal plane. In this way the mirror acts as a Fourier filter that selects only one half of the illumination profile. A focusing lens (FL) is then placed above the KE and it makes an image of the output facet of the HP, at the OP. An identical set of elements is placed on the other side of the KE.

lights up with even intensity. The output facet can then be imaged at the object plane.

The angular distribution of this facet is still symmetric with respect to the optical axis, so it has to be filtered so that the two LEDs provide mirrored distributions that can be both focused at the same position. A convenient solution that combines the filtering and combination of illuminations is the Knife Edge mirror (KE). This is made of two mirrors at 90°, and the edge is also reflective (Thorlabs, MRAK25-G01). The edge is placed at the back focal plane of the collimating lens, such that it intersects the optical axis. In this way, the horizontal plane just above the KE will contain only half of the angular distribution of each light pipe output. A focusing lens is then placed at a focal distance from this plane, so that two similar images of the hexagonal facets are created at the object plane.

This solution is very compact, and as a consequence it is possible to use short focal length, high NA lenses, with the benefit of minimal losses and maximum NA. On the other hand, this implementation only features one axis of illumination, which can cause distortions of the phase reconstruction due to missing spatial frequencies in the direction perpendicular to the axis of illumination [24]. This issue could be solved by using custom mirrors with multiple facets, such as pyramidal for two-axis illumination. The I and Q output could then be dedicated to an axis of illumination each, rather than being identical such as in the current implementation. In this chapter, the main focus is contrast, and distortions are mitigated for the reconstructions in Section 4.3.4 by making sure that none of the main edges were parallel to the illumination.

Fig. 4.4 shows the achieved uniformity of illumination using this system. Fig. 4.4(a) and (b) report images of the sample plane under left and right illumination, respectively. The average grey level is 210. The difference between these two images is shown in Fig. 4.4 (c), and a cross section along the blue dashed line is shown in Fig. 4.4 (d). The difference image shows the residual non-uniformity that will be enhanced in lock-in DPC, ultimately fixing the limit to the improvement of CNR in the current implementation, as discussed in Section 4.2.1. The standard deviation across Fig. 4.4 is 2.8, giving approximately a 1% non-uniformity.

4.3.2 Method

The setup described in Fig. 4.3 was used to characterize the improvements given by the use of lock-in compared to standard DPC.

For each experiment, images of the same sample are collected using both DPC modalities: standard DPC, based on the difference of two images that were separately acquired, and lock-in DPC, based on in-pixel demodulation by the camera.

The lock-in camera features a so-called "intensity mode", where two standard images at different exposure times are collected. The camera then outputs a High Dynamic Range (HDR) image, composed of the non-saturated pixels from the two images. In order to avoid the mixing of these two images, which could introduce extra noise and make the evaluation of CNR incorrect, I maintained the average grey level around one quarter of the 10 bit range, so that only the long exposure time image is used. This means that the exposure time could be increased by a factor of 4, improving the CNR by a factor of two, according to Eq. 4.17. Since
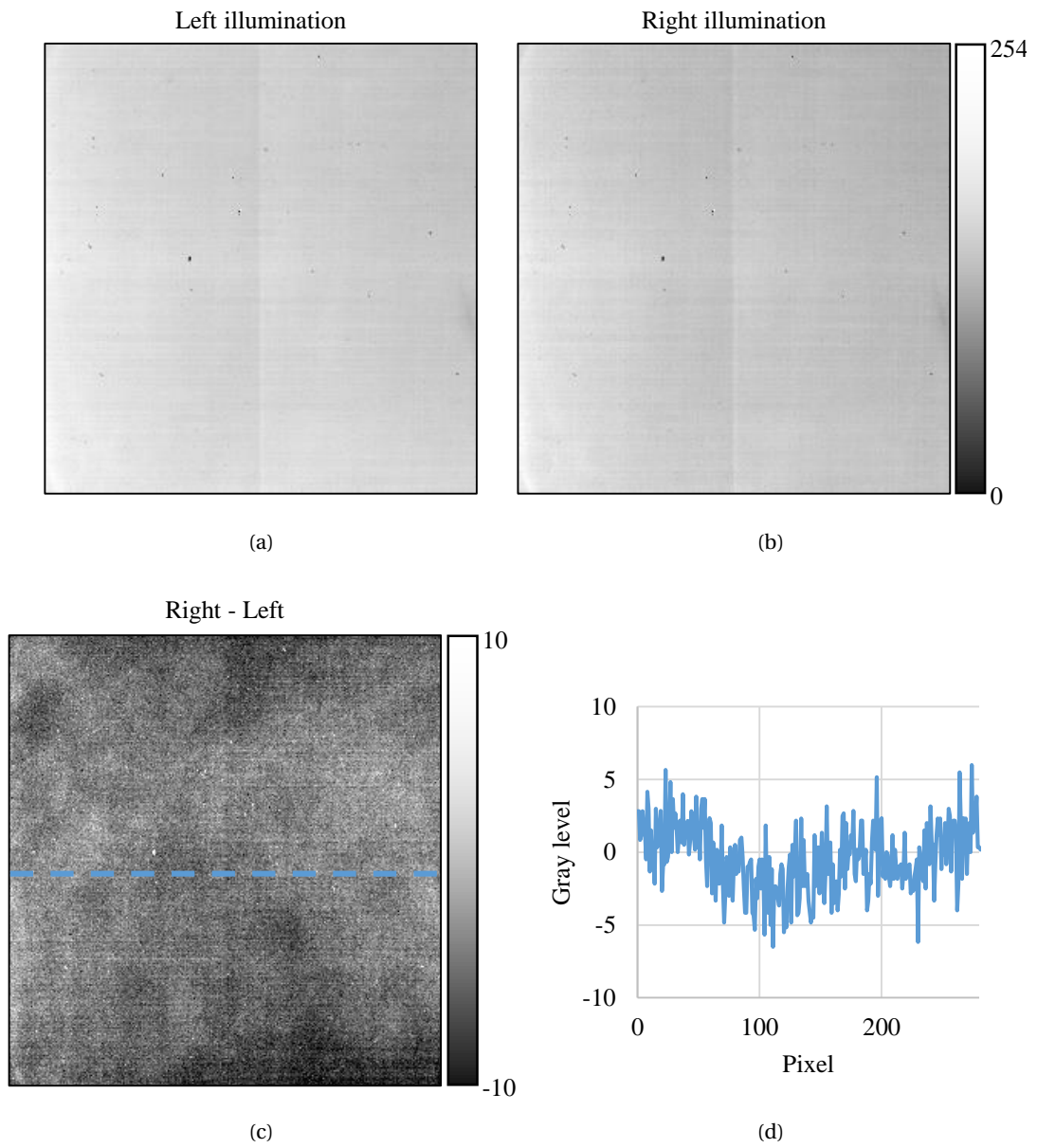
Figure 4.4: (a) Image of the sample plane under left illumination. (b) Image of the sample plane under right illumination. (c) Difference between (a) and (b), corresponding to the residual non-uniformity which will be present in lock-in DPC images. (d) Cross section of the difference image along the blue dashed line.

we are interested in comparing the best result of lock-in DPC with the best result of standard DPC, I will take these factors into account in the following results.

Background images in the absence of a sample are also collected in order to remove unwanted illumination structures, which are particularly intense in lock-in DPC due to the strong amplification. The power of the LEDs is maintained equal during all measurements. This means that the exposure time for standard DPC has to be much shorter due to saturation.

The USAF target samples used in these experiments where fabricated by photo lithography of fused silica wafers with varying etching times, in order to obtain different heights and, as a consequence, different phase values. The nominal height was calculated based on the calibrated etching rate, and later verified via AFM measurements.

4.3.3 Sensitivity

The first set of measurements concerns the improvement of sensitivity that lock-in DPC allows to achieve. A qualitative comparison is shown in Fig. 4.5, for a USAF target whose phase difference is approximately 19 mrad. In particular, Fig. 4.5 (a) and (b) show a ROI for standard and lock-in DPC, respectively.

For the lock-in image, the duration of one cycle is set to be approximately 140 μs, and four cycles are averaged by the camera before transmitting the digitized measurement to the computer. From Eq. 4.16, the effective exposure time is 280 μs. The sum $I + Q$ is shown in Fig. 4.5(b), after background subtraction.

The standard DPC image is obtained by subtracting the images I_L and I_R, obtained with left side and right side illumination respectively. Each image is recorded over 1 μs, and Fig. 4.5 (a) shows the average of 280 DPC images, which is approximately equivalent to the amount of integrated light in lock-in DPC.

The cross-section of the USAF target obtained in the two cases is shown in Fig. 4.5(c), without averaging of the standard DPC case. It is possible to appreciate that, while the shape of the cross-section is very similar, the intensity of the positive and negative peaks in lock-in DPC is encoded over approximately two orders of magnitude more than those of standard DPC. Moreover, having been able to integrate significantly more light, the relative variation of the grey level between the pixels, caused by noise, is greatly reduced in the lock-in measurement. For an equal amount of collected data, that is I and Q in lock-in, and I_L and I_R in standard DPC, it is possible to observe a much better contrast and reduced noise in the first case.

In order to analyse the improvement of contrast in a more quantitative way, I measured the CNR of several USAF samples, with varying phase values, in both DPC techniques. The CNR was calculated as the ratio between the amplitude of the cross section (maximum minus minimum, as seen in Fig. 4.5 (c)), and the standard deviation of a featureless area [46, 47]. The ratio of exposure time was again 280. The exposure time chosen for the lock-in DPC was such that some of the peripheral pixels were saturated, thus this is considered to be the maximum amount of photons that can be integrated before significant distortion. In the standard case, the average grey level reached only one quarter of the full dynamic range, for the reasons explained previously. In order to compare the maximum CNR of both techniques, I corrected
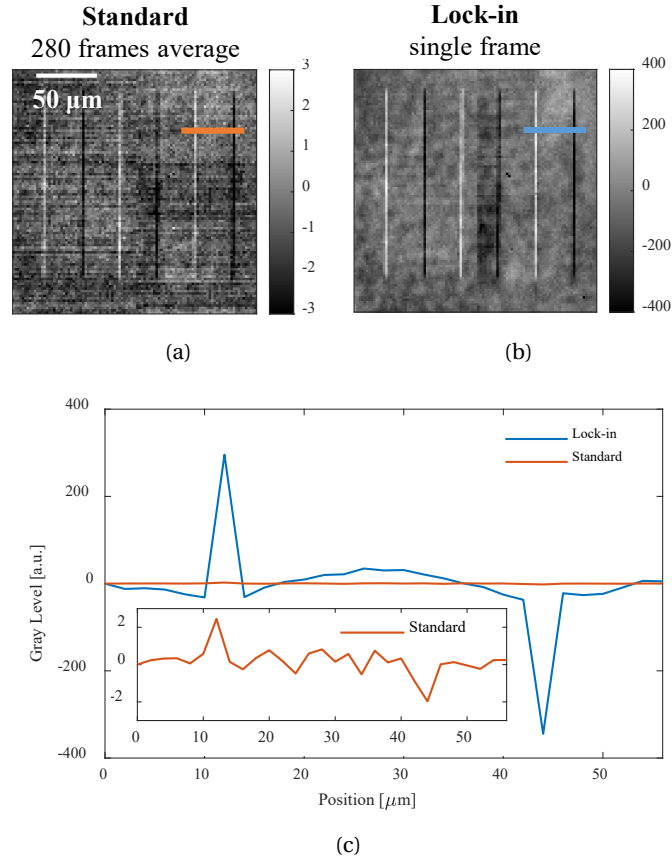
Figure 4.5: Comparison of standard and lock-in DPC images of a 19 mrad USAF target. (a) ROI of the USAF target measured in standard DPC, after background subtraction and averaging of 280 frames of 1 μs exposure each. (b) ROI of the USAF target measured in lock-in DPC, over a total exposure time of 280 μs, after background subtraction. This image is the sum of the two quadrature images I, Q. (c) Comparison of the cross section of the right-most structure, in lock-in and standard DPC. The blue cross section refers to the lock-in measurement, while the orange cross section refers to a single standard measurement. The inset shows the same cross section for standard DPC, but with a zoomed scale.

(a)

(b)

(c)
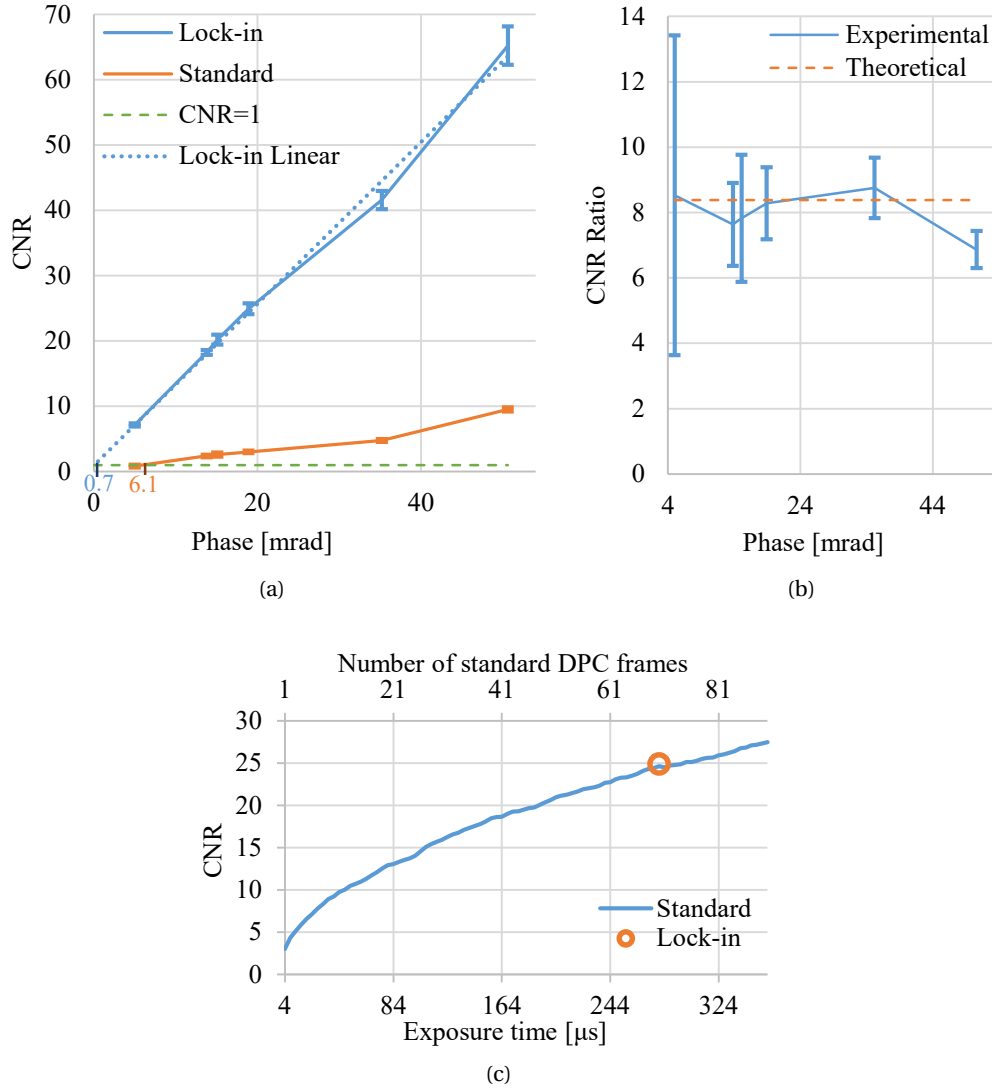
Figure 4.6: (a) The CNR is calculated for several samples and plotted against their phase, for both lock-in and standard DPC, in blue and orange, respectively. The CNR of the standard DPC measurements has been multiplied by 2 to take into account the possibility to increase the exposure time without saturating the 10-bit detector. The error bar is obtained over 100 measurements. The green dashed line represents the sensitivity limit at CNR=1, while the blue dotted line is the extrapolated linear trend of the CNR in lock-in DPC. According to this extrapolation, on the horizontal axis the phase sensitivity of lock-in DPC and standard DPC are shown, in blue and orange respectively. (b) The ratio of CNR between lock-in and standard DPC is plotted against the phase of several USAF targets. This ratio should be constant at 8.36. The error bars are obtained over 100 measurements. (c) CNR for increasing number of averaged standard DPC frames, compared to a single lock-in acquisition. The top horizontal axis shows how many frames are averaged, while the bottom horizontal axis shows how much time is required in total.

the exposure time ratio by a factor of four, giving 70, and I multiplied all the CNR values of standard DPC by a factor of two.

The results of these measurements are given in Fig. 4.6 (a): it is possible to observe how the CNR for the lock-in technique are consistently greater than those of standard DPC. In particular, for the smallest sample that I used, at 5 mrad, the CNR of the standard DPC is around 0.82, which means it is already below sensitivity. On the other hand, for the lock-in case, the CNR is around 7.2, which means that the sensitivity limit would be reached around 0.7 mrad. This is approximately a factor of 8 improvement, which is expected given the exposure time ratio of 70, using Eq. 4.18. Indeed, Fig. 4.6 (b) shows the experimental CNR ratio, plotted for all the samples I tested, compared with the theoretical value: the experimental CNR ratio oscillates around this value. Two of the experimental points require further explanations. The error bar for the first phase value is significantly bigger than the other ones: this is because the amplitude of the cross section in standard DPC suffered from great uncertainty due to its being below sensitivity. This error is then propagated to the CNR ratio. The last experimental point is further from the theoretical values compared to the other cases. It is possible that the amplitude of the cross section in lock-in DPC is in fact underestimated in this case, as the modulation given by this sample was very close to saturation. Saturation of the lock-in DPC image would explain a CNR value lower than expected.

As shown theoretically and experimentally, for an equal amount of collected data, the CNR of lock-in DPC will be greater than that of standard DPC by a factor equal to the square root of the exposure time ratio. On the other hand, it is still possible to reach the same CNR, by averaging enough frames to reach an equivalent total exposure time, as shown in Fig. 4.6 (c). In this experiment, I collected multiple identical frames in standard DPC, and calculated the CNR of an increasing number of averaged frames. The curve of CNR displays the classic behaviour, where N is the number of samples, in this case frames. The orange circle marks the CNR value and exposure time of the lock-in case. Indeed, when 70 standard frames are averaged, reaching the same total exposure time, the CNR is very similar.

4.3.4 Reconstruction

A key feature of DPC is the possibility of reconstructing quantitative phase information about the sample. As explained in Section 4.2.2, in order to do this, the DPC image has to be normalized by the background B. While this value is not known in a lock-in measurement, a solution was described, by multiplying the standard DPC background and to the ratio of exposure time. As an example, I measured the phase of a reconstructed USAF target, in both standard and lock-in DPC, and the result is shown in Fig. 4.7. In this experiment, I reconstructed a 50.6 mrad sample. In Fig. 4.7(a), the reconstruction is based on a single standard DPC image, over an 8 μs exposure. In Fig. 4.7(b), instead, 58 standard DPC frames were averaged, equalling the 464 μs exposure of the lock-in DPC reconstruction of Fig. 4.7(c). Indeed, it is possible to see how in the first image, it is difficult to recognize the shape of the target, due to the amount of noise that has been transferred to the reconstructed phase. By averaging enough frames, it is possible to obtain a similar reconstruction quality as in lock-in.
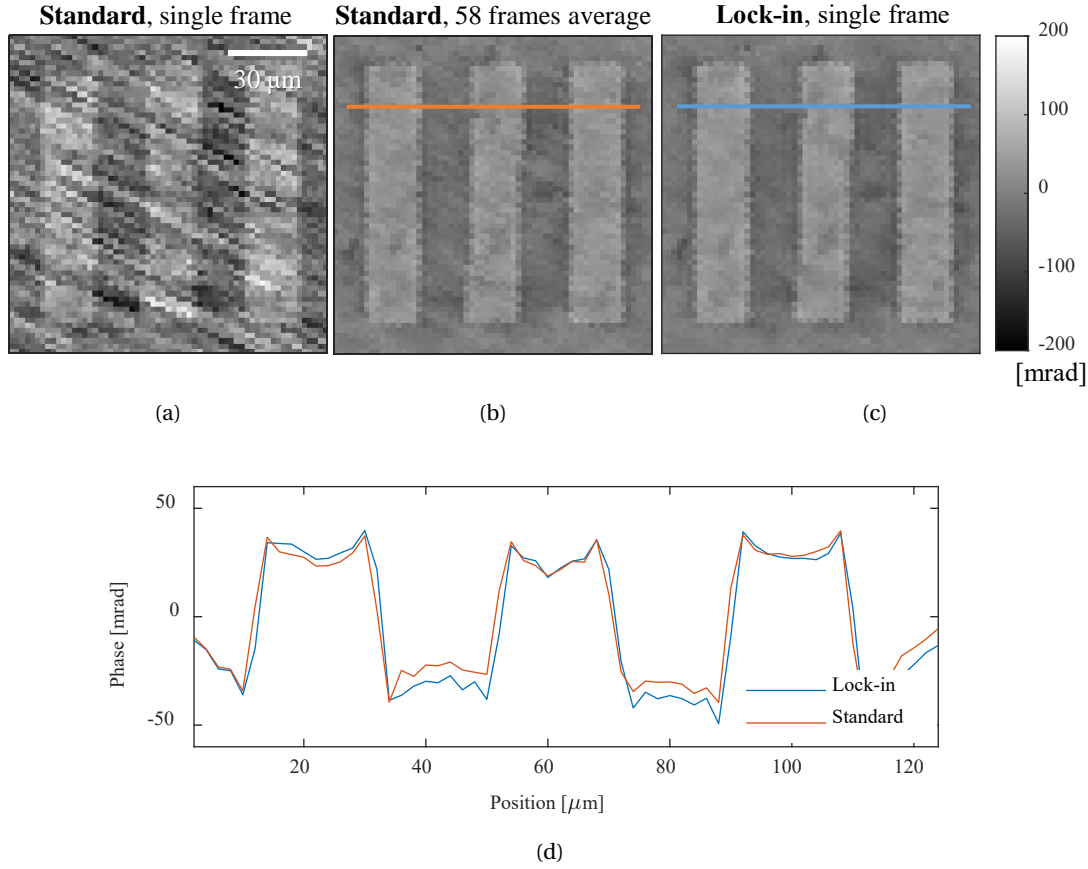
Figure 4.7: Reconstructed phase of a 50.6 mrad USAF target. The target was placed with an angle of 25° with respect to the direction of illumination, so that none of the edges was parallel to it. As a consequence, no distortion is caused by the missing frequencies. The ROI is rotated here to show straight rectangles. (a) Reconstructed phase from a single 8 μs exposure standard DPC image. (b) Reconstructed phase from 58 averaged standard DPC frames. (c) Reconstructed phase from a single 464 μs lock-in measurement. (d) Comparison of the cross sections indicated in (b) and (c) with the orange and blue lines.

From a quantitative point of view, Fig. 4.7(d), shows the comparison of the cross sections from reconstructions (b) and (c), highlighting the correct quantitative result of reconstruction for our lock-in DPC measurement, using the standard background.

In Fig. 4.8, I show another interesting feature of lock-in DPC, which is the possibility of modulating contrast by changing the exposure time, without the need to acquire more frames. In particular, Fig. 4.8(a) shows the phase reconstruction from a single 7 μs exposure standard DPC image, compared with a single lock-in exposure of 120 μs in (b), and 248 μs in (c). The zoomed in areas shows how some low-phase features become more nuanced using lock-in. In both (b) and (c), just a single image was collected. As demonstrated previously, it would still be possible to obtain similar results in standard DPC, but this would require acquiring 17 images to reach the contrast of Fig. 4.8(b), and 35 images to reach Fig. 4.8(c), with the disadvantages

Standard, 7 µs exposure   **Lock-in**, 120 µs exposure   **Lock-in**, 248 µs exposure
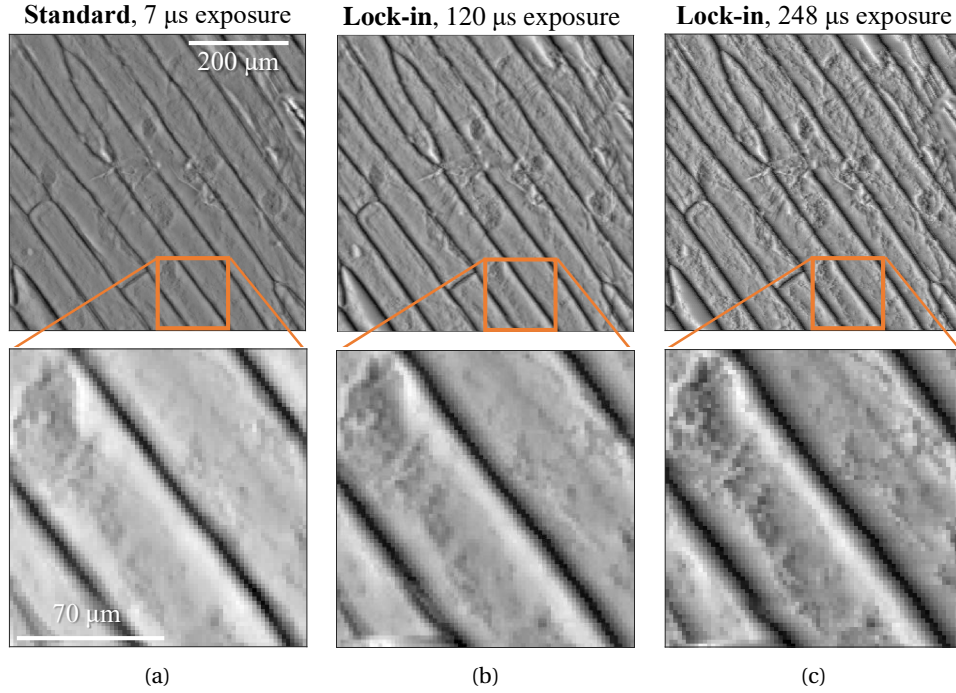
Figure 4.8: Phase reconstruction of onion epidermal cells. (a) Reconstruction from a single, 7μs exposure, standard DPC image. (b) Reconstruction from a single, 120 μs exposure, lock-in DPC image. (c) Reconstruction from a single, 248 μs exposure, lock-in DPC image. Second row: zoom from the areas indicated in the orange squares.

that come with a more data intensive measurement, as explained in Sec. 4.3.3.

4.4   Advantages of lock-in DPC

In Fig. 4.6(c), it was demonstrated that similar sensitivities can be reached in standard DPC as in lock-in DPC, by averaging tens of frames. This drastically increases the bit rate of the stream from camera to computer, or reduces the duration of recording for cameras with onboard memory. The power of lock-in DPC stands in being able to reach such sensitivity in a single frame, drastically reducing the data- and time- intensiveness of the technique. For example, for a time lapse recording at 1400 frames/second, with a 300x300 pixels detector and a 10 bit depth, we obtain a 1.26 Gbit/s rate in lock-in DPC, and 88.2 Gbit/s with standard DPC for equal CNR. Current camera interface technologies can reach few tens of Gbit/s speed, such as multichannel CoaXPress, so reaching the same sensitivity as lock-in DPC at the same speed would not be possible. The current heliCam model, like most high-speed cameras, is actually equipped with an onboard memory, which dictates the maximum total recording time before images have to be downloaded to the computer. Considering for example an 8GB memory, in lock-in DPC it is possible to record up to 50.79 s, compared to only 0.72 s in standard DPC. This example is summarized in Table 1.

Table 4.1: Example of bit rate and recording time at 1400 frames/s

	Standard DPC	Lock-in DPC
Bit rate	88.2 Gbit/s	1.26 Gbit/s
Recording time for 8GB memory	0.72 s	50.79 s
Recording time for 16GB memory	1.45 s	101.58 s

This analysis shows that, when resorting to averaging multiple frames to obtain the same sensitivity as in lock-in DPC, the result will still be inferior: with direct computer transfer the frame rate will be lower, and with onboard memory the total recording time will be drastically reduced. Both these choices are undesirable for real time biological imaging.

4.5 Conclusion

In this chapter, a new approach to DPC was described, which takes advantage of periodic modulation of illumination to automatically extract the DPC information without encoding the background. As a consequence, longer exposure times are possible without saturation of the pixels, which allows to increase the CNR by almost an order of magnitude, in a single shot. In particular, I demonstrated an improvement by a factor of up to 8.3 of CNR for single exposures, which means that around 70 frames are needed in standard DPC to reach the image quality of lock-in DPC.

While similar CNRs are reachable in standard DPC, it is necessary to average tens of frames, which drastically increases the bit rate of the stream from camera to computer, or reduces the duration of recording for cameras with onboard memory.

Currently, these results are limited by the non-uniformity of the illumination, which could be improved with better illumination setups or by actively matching the sources, for example using a spatial light modulator. If better illumination is achieved, even longer exposure times can be sustained, further increasing the single-shot sensitivity.

Another limit of this technique is the resolution and field of view given by currently available lock-in cameras. The in-pixel demodulation circuit requires a certain amount of space, giving a pixel size of 40 by 40 μm, and a total detector size of 300 by 300 pixels. On the other hand, this technical limitation may be overcome in the future.

Moreover, other types of applications can be foreseen for this type of imaging, which can be applied in any situation where weak modulations over strong backgrounds have to be measured. For example, the sample response to illuminations of different polarization or wavelength may be analysed to map morphological or chemical structures within the sample.

Overall, this approach may enable easier measurement of weak phase details or dynamic phenomena, such as in biological samples, where only interferometric techniques were applied until now [61–63]: for example, Ling et al. [62] successfully imaged action potentials in an interferometric system with 0.3 mrad sensitivity and 1 000 fps. In my experiments, I have obtained a sensitivity of 0.7 mrad over a 1400 fps frame rate, which comes quite close to the requirements of action potential imaging, while removing issues associated with the use of

coherent sources, such as speckle noise. This performance is currently unparalleled in any incoherent phase contrast imaging system.

While further improvement of the illumination setup and spatial resolution may be necessary, future applications of this technique will be of interest for several scenarios in biology.

5 | Lock-in Raman difference spectroscopy

In this chapter, I introduce a new approach to Raman spectroscopy, that takes advantage of the lock-in camera to perform high-sensitivity, background-free Raman spectroscopy measurements.

5.1   Introduction

Raman spectroscopy is a widely used spectroscopic technique that enables label-free detection of chemicals as well as their quantification [15, 72, 73]. The analysis of the spectrum of light after inelastic scattering events within a sample can yield significant information regarding its structure and composition [74, 75]. While Raman spectroscopy is presently available as consumer products [15, 72, 76, 77], its use has been limited until recently due to its very low efficiency and long integration times. Indeed, a number of Raman techniques have been developed over the years to increase the signal [15], such as surface enhanced Raman spectroscopy, coherent anti-Stokes Raman spectroscopy, stimulated Raman scattering, as well as ongoing research to improve spontaneous Raman [78–80].

One well known challenge in Raman spectroscopy is the presence of a strong fluorescence background when visible light is used as the excitation wavelength [13, 14], particularly when compared to typical Raman efficiency, that can be as low as 10^{-8} of the incident excitation power [15, 16]. Fluorescence light can be emitted by the molecules of interest themselves, as well as the surrounding medium, and is particularly problematic for biological investigation [13], which is also one of the main drivers for research and further development of the technique [17]. The presence of this background causes several limitations [14]: it is difficult to identify Raman peaks over the fluorescence background and thus obtain quantitative estimations. The background noise is increased and the SNR is reduced. Detector saturation may limit the exposure time and again reduce the SNR.

Several solutions to enhance the Raman signal with respect to the fluorescence background have been proposed, either taking advantage of different characteristics of those types of emission (lifetime, spectral width, polarization), via interaction with other materials such as nanoparticles, or by leveraging the relation to the excitation wavelength [13]. Each of these methods has its advantages and disadvantages, and the appropriate choice is dictated by the application.

One way to reduce the fluorescence signal is to use excitation wavelength in the near infrared, where the fluorescence emission is typically weaker. On the other hand, the Stokes emission then takes place at longer wavelength, and silicon based detectors are not efficient above 1000 nm. Alternatively, the use of differential excitation has been proposed [81, 82]: the idea in this case is to use two or more wavelengths of excitation to produce multiple spectra. Raman scattering occurs at fixed offsets to the excitation wavelength, so its wavelength shifts in lockstep with the excitation source. The fluorescence component instead, has a much lower dependence on the wavelength of excitation when small shifts are considered. Computing the difference between spectra generated by two closely spaced excitation wavelengths generates background free differential spectra that can be analysed more effectively [18, 19, 83, 84]. This technique is usually referred to as SERDS. It is important to note that all these steps occur in post-processing. Each spectrum still contains the high-intensity background, which is digitally removed by subtraction. This means that the exposure time might have to be reduced in order to avoid detector saturation from strong backgrounds, and that the single-shot SNR of the Raman peaks remains low. Some previous works use synchronized illumination and detection, such as with charge-shifting CCDs [85], but the two spectra are still separately digitized, thus not solving the issue of saturation. The same applies to schemes that include multichannel lock-in [86], as the signal comes from a standard CCD and is thus bound to the well capacity of its pixels. One example of analog lock-in amplification was proposed by Liao et al. [87], showing improved SNR at short exposure times, but paired with stimulated Raman scattering, and with only 16 parallel channels.

Taking inspiration from our previous work on lock-in DPC [88], in this chapter I show how it is possible to use a lock-in camera to obtain on-line, analog SERDS spectra. With this method, it is possible to obtain background free spectra with longer exposure times and no saturation. Here, I demonstrate two case scenarios for the use of lock-in Raman spectroscopy. In the first example I use a single wavelength of excitation, and show how the ambient light, that would otherwise saturate the detector in normal conditions, can be removed. This allows the use of Raman for in-vivo or in-vitro applications without the need to shield the detector or operating in dark ambient conditions, facilitating the use of Raman instrumentation in non-conventional configurations. In a second example, two distinct excitation wavelengths are used to obtain a SERDS measurement whereby the fluorescent background is removed analogically in the lock-in camera. To encompass both the single source and double source configuration, I will refer to this technique as lock-in Raman Difference Spectroscopy (RDS).

5.2   Theory

5.2.1   Basic SERDS theory

Let us assume that the Raman emission spectrum obtained from a sample of interest is described ideally by the function $R(\lambda, \lambda_e)$, where λ is the emission wavelength, and λ_e is the excitation wavelength. The sample may also emit light in the form of fluorescence upon excitation, which is described by the function $L(\lambda)$. Moreover, unwanted light may also come

from external disturbances such as ambient illumination or stray light, and are described as an excitation-independent background $B(\lambda)$.

The whole spectrum can then be described as the sum of these contributions [83]:

$$S(\lambda, \lambda_e) = [L(\lambda) + R(\lambda, \lambda_e)]M(\lambda) + B(\lambda)\,, \tag{5.1}$$

where $M(\lambda)$ represents the modulations of the ideal spectrum introduced by the optical system.

The Raman spectrum responds to changes in the excitation wavelength only by an equal shift in the emission, with no significant changes in the spectrum itself. For two excitation wavelengths λ_1 and λ_2, where $\lambda_2 = \lambda_1 + \delta\lambda$, we can write:

$$R(\lambda, \lambda_2) = R(\lambda + \delta\lambda, \lambda_1)\,. \tag{5.2}$$

If we measure the spectra $S(\lambda, \lambda_1)$ and $S(\lambda, \lambda_2)$, we can then compute their difference:

$$\delta S(\lambda) = [R(\lambda + \delta\lambda, \lambda_1) - R(\lambda, \lambda_1)]M(\lambda)\,. \tag{5.3}$$

If the excitation wavelength difference is small, then δS can be expressed as the differential of the Raman spectrum, so the Raman spectrum can be retrieved through an integration:

$$R(\lambda) = \int M^{-1}(\lambda)\delta S(\lambda)\delta\lambda\,. \tag{5.4}$$

5.2.2 Lock-in RDS

While SERDS helps in digitally removing the fluorescence and ambient background from Raman spectra by subtraction, it does so in a post processing second step. This means that no benefit is provided in terms of dynamic range: when the Raman signal is much weaker compared to the background, the exposure time has to be set to accommodate the whole intensity within the well capacity of the detector. As a consequence, the SNR of the Raman peaks is only partially improved, unless multiple spectra are recorded and averaged. Of course, the stronger the background intensity, the shorter the possible exposure time, which means more spectra need to be collected. This can obviously put a strain on the data-intensiveness of the experiments, especially when a scanning confocal microscope is used to map the Raman spectrum of a sample.

A clear parallel can be drawn between this case and that of DPC [88]. In both techniques, the difference between two similar measurement, be it images or spectra, is calculated to separate a small, periodically modulated signal of interest from a high-intensity constant background. In DPC, the signal of interest is the phase term, and the modulation is a change of sign caused by the switching of mirrored illumination sources. In SERDS, the signal of interest is the Raman spectrum, and the modulation is the shifting of Raman peaks caused by a change in wavelength of excitation.

In order to remove the background in a bit-efficient way, I propose the use of a lock-in camera as a detector for differential Raman spectra. In our experiments, I used the helicam C3,

(a)

(b)
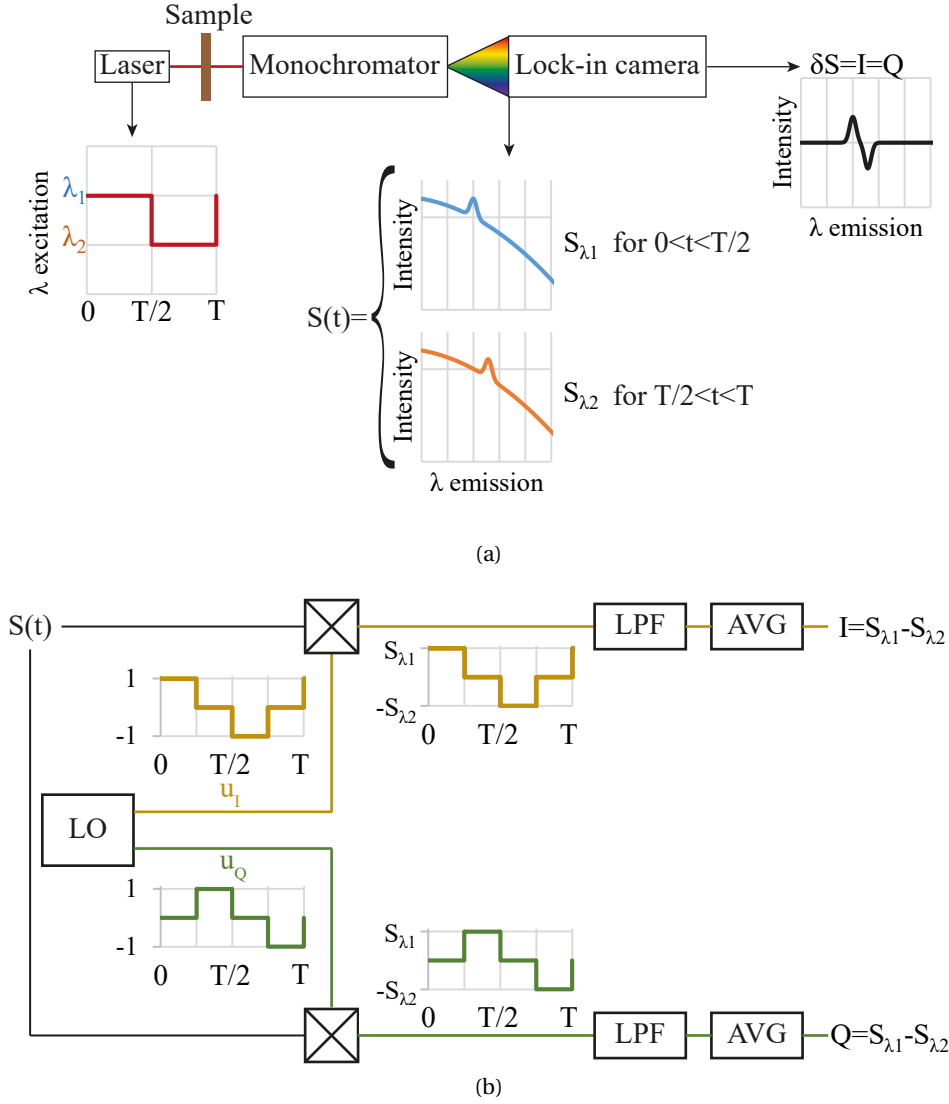
Figure 5.1: Scheme of operation of lock-in RDS. (a) The laser source is periodically driven between two wavelengths λ_1 and λ_2 over a period T. The spectrum $S(t)$ emitted by the sample is consequently time dependent and periodically modulated over the same period, switching from S_{λ_1} to S_{λ_2}. The lock-in camera demodulates this signal and outputs directly the difference spectrum δS. (b) Internal operation of a pixel of the lock-in camera. The local oscillator (LO) generates two periodic signals in quadrature, which are multiplied with the input modulated spectrum. The resulting signals are low-pass filtered (LPF) and summed, giving the two outputs I and Q. If the modulation of the input spectrum takes place at the same period and phase of the local oscillator signals, then I and Q are identical, and equal to the difference spectrum δS.

produced by Heliotis: this camera features a detector with pixel-level circuitry that allows to perform direct I-Q demodulation [67–69]. A schematic explanation of the mode of operation of lock-in RDS is given in Fig. 5.1.

The hardware elements of the setup are shown schematically in Fig. 5.1(a). The source of excitation wavelength is modulated periodically over a period T, switching between two closely spaced wavelengths λ_1 and λ_2. This may be done by modulating a single source, or alternatively switching on and off two different lasers. This wavelength switching source is used to excite Raman emission in the sample, and the emission is collected by a monochromator. The wavelength-spread light is sent to the detector of the lock-in camera, and due to the periodically shifting nature of the excitation, the spectrum is also time-dependent. In particular, Fig. 5.1(a) shows two example simulated spectra where a single Raman peak is present over a strong background. For the first half period, $S(t) = S_{\lambda_1}$, and for the second half period $S(t) = S_{\lambda_2}$, where the background portion of the spectrum is the same as in S_{λ_1}, and the Raman peak has shifted by $\delta\lambda$. Thanks to the pixel-level demodulation, the lock-in camera outputs directly the difference spectrum δS.

The internal operations performed at the pixel level are showed in more details in Fig. 5.1(b). A local oscillator generates two periodic signals in quadrature, which are made of a sequence of [1, 0, -1]. The modulated optical signal received by each pixel, which represents a portion of the emitted spectrum, is multiplied to each local oscillator signal. The resulting signals are then low-pass filtered and summed, giving the two output frames I and Q. It is possible to see that, if both the modulated spectrum and local oscillator are periodic over a period T, and in phase, both I and Q are given by the difference between the two shifted spectra, so effectively they are the difference spectrum δS.

What is described in Fig. 5.1 is a scheme that is capable of removing the fluorescence and ambient light background similarly to SERDS. The same scheme could also be used with a single laser, which is switched on and off over the period T. In this case, the spectrum during the first half interval is given by the Raman peaks and any background present, while during the second half period the spectrum would correspond only to the ambient light. As a consequence, the difference spectrum output by the camera would be the Raman spectrum without ambient light contributions. Obviously this cannot remove emissions that depend on the presence of laser excitation, such as fluorescence, but if this source of background is negligible compared to ambient light, this scheme of operation would be advantageous since it directly gives the Raman spectrum rather than the difference spectrum.

Another possible way to use this camera is with four wavelengths, each on during a quarter period. Two differential spectra would be obtained, providing extra information to improve the recovery of the Raman peaks.

The advantage of analog demodulation of the difference spectrum at the pixel level is that the background information is never stored, and thus it does not contribute to filling the well capacity. As a consequence, the exposure time can be increased, causing only the Raman peaks' intensity to rise. Ideally, the exposure time could be set up to the point where one of the Raman peaks almost fills half of the bit-depth, which would give the best possible SNR with the given detector. The overall intensity of the spectrum still generates noise within the pixels,

and it is possible to show that SNR of lock-in RDS improves with respect to the standard case as [88]:

$$\frac{SNR_{\text{lock-in}}}{SNR_{\text{standard}}} = \sqrt{\frac{T_{\text{lock-in}}}{T_{\text{standard}}}} \qquad (5.5)$$

Where $T_{\text{lock-in}}$ is the duration of a half modulation period and T_{standard} is the exposure time for a single spectrum.

5.3 Experimental

5.3.1 Raman setup

The setup used for the experiments is shown in Fig. 5.2. Since two lasers were used, they needed to be aligned onto the same path using a beam splitter. In order to maximize power efficiency, I used a polarizing beam splitter and two half-wave plates to rotate the polarization of each laser. A band-pass filter is used to remove some spurious emissions from the lasers at longer wavelengths. The laser light is then transmitted through a dichroic mirror and focused onto the sample by a 60x objective with 0.8 NA. The same objective is also used to collect light emitted by the sample, and the dichroic mirror reflects it toward the monochromator. While the dichroic mirror mostly doesn't reflect the laser light, the remaining small percentage is still stronger than the Raman emission, so a long-pass filter is used to remove this remaining disturbance. The spectrum is obtained with a Horiba grating monochromator with 25 cm focal distance; the grating is blazed at 750 nm and has 600 grooves/mm. A cylindrical lens is used to focus the spectrum over a thin line at the lock-in camera's detector.

The laser diodes used in this setup are Thorlabs' HL63142DG, with nominal wavelength of 637 nm and maximum power of 100 mW. In order to obtain slightly spaced wavelengths, I used the LDM56 temperature control mounts and set their temperatures to different values, observing experimentally optimal differentiation of the Raman peaks of interest. The switching of the lasers was controlled by a National Instruments acquisition card, which also generated the triggering signal for the lock-in camera.

5.3.2 Adapting the lock-in camera for Raman experiments

As mentioned previously, it is expected that the analog demodulation of the difference spectrum would bring the advantage of longer exposure times over multiple short exposure frames, in line with what has been demonstrated for DPC [88]. On the other hand, the current model of the lock-in camera was not developed for this application and, as such, is not optimized for the low signals related to Raman spectroscopy: even the fluorescence component is typically several orders of magnitude weaker than the excitation source, and is subject to saturation and quenching. As a consequence, the maximum period of one demodulation cycle on the C3 detector is limited to approximately 470 μs. This is extremely short compared to typical Raman spectroscopy experiments, which can last up to several minutes. Moreover, the aspect
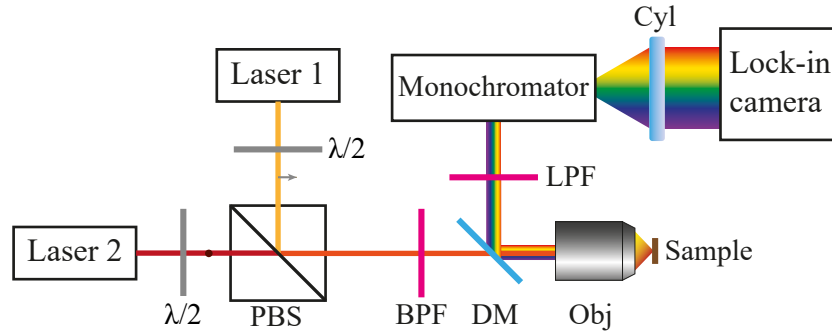
Figure 5.2: Setup for lock-in RDS. Two lasers are combined on the same path using a Polarizing Beam Splitter (PBS). In order to maximize transmission and reflection respectively, the polarization of each laser is tuned using a half-wave plate ($\lambda/2$). A Band-Pass Filter (BPF) is used to remove some spurious emissions from the lasers at longer wavelengths. The laser light is transmitted through a Dichroic Mirror (DM) and focused on the sample by a 60x objective (Obj) with 0.8 NA. The light emitted by the sample is collected by the same objective, and reflected by the DM. A Long-Pass Filter (LPF) rejects remaining laser light. The different wavelengths are then dispersed by a Horiba monochromator with focal length of 25 cm. A cylindrical lens (Cyl) focuses the spectrum to a line that occupies few pixels on the detector of the lock-in camera.

ratio of the camera is square, since it is meant for imaging, whereas only a thin line of pixels is actually being used for this spectroscopy application. It is possible to set the detector to average up to 510 cycles internally, practically increasing the effective exposure time. However, in our experiments, the performance in terms of SNR seemed to deteriorate for more than 32 cycles, so I assumed this to be the maximum effectively usable.

In this chapter, I used samples that are known to be strong emitters, like diamond powder, so that a Raman signal may be picked up even in such short exposure time conditions. Where necessary, I sum up multiple frames of lock-in RDS until saturation of the 10-bit scale is virtually close to being reached. Assuming that the camera were to allow such long exposure times, this would be the limit at which we would need to stop our measurement, and thus it would give the SNR to compare with standard RDS [88]. In the manuscript, extrapolated results will be pointed out for clarity, with respect to purely experimental results. It is important to note that the results extrapolated from summing multiple frames are expected to be slightly worse than the equivalent single long exposure, due to extra digitization noise present in each frame, so these may be interpreted as worst case scenario.

The goal of the present chapter is to demonstrate a proof of concept to improve single-shot SNR in RDS, given the high interest present around Raman imaging [17]. The benefits of this technique may be enhanced in the future with a tailored version of the helicam detector.

5.3.3 Single-laser RDS

The first experiment demonstrates the use of the lock-in camera for the analog removal of background light that is not excited by the laser source itself, such as ambient disturbances.
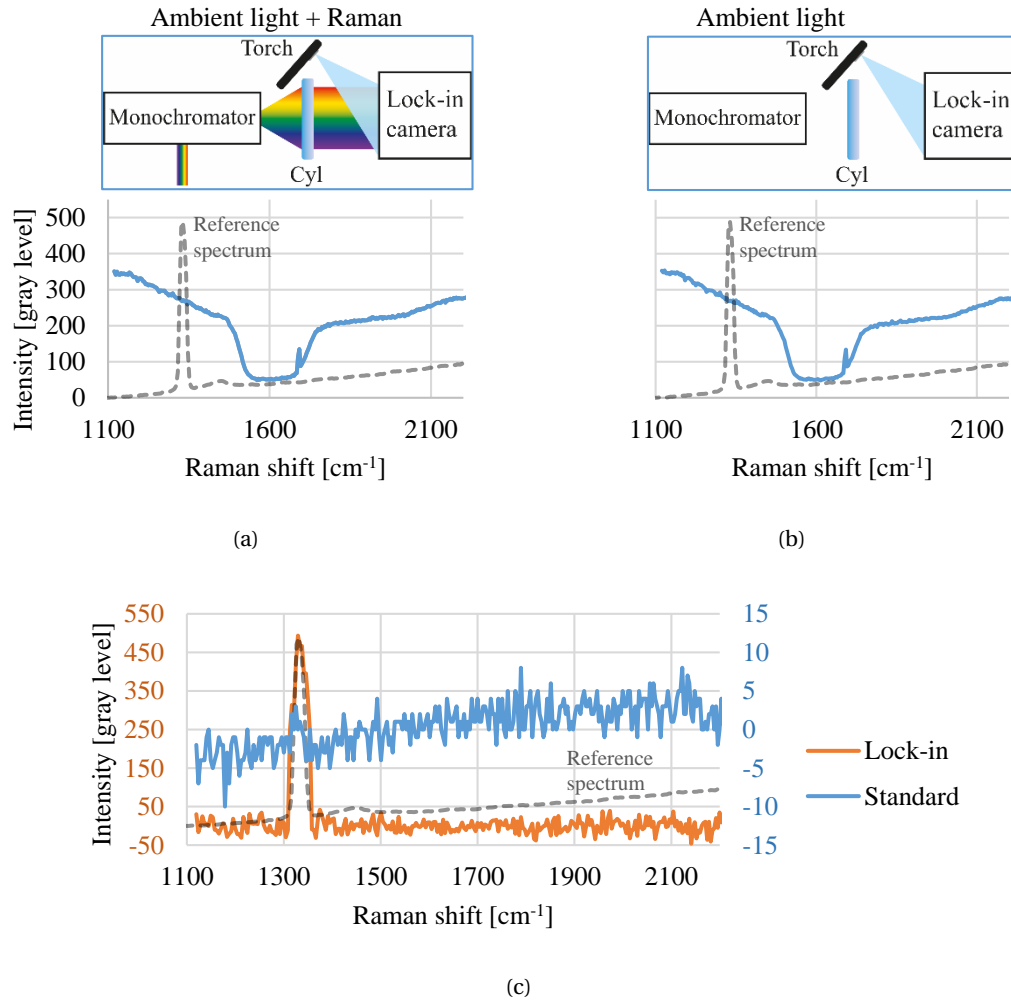
Figure 5.3: Single laser background removal experiment. (a) Standard measurement of the Raman spectrum with external disturbance. The box above the spectrum shows the measurement configuration, with both the laser source and torch on. (b) Standard measurement of the external disturbance. The box above the spectrum shows the measurement configuration, with only the torch on. (c) Comparison between the standard Raman spectrum after digital background subtraction, and the lock-in Raman measurement. The blue standard spectrum was obtained from the difference between spectrum (a) and (b). The orange lock-in spectrum was obtained by switching the laser on and off periodically, synchronously to the lock-in camera local oscillator. In all graphs, the dashed black spectrum shows the reference diamond powder spectrum measured with a commercial confocal Raman microscope using a 600 gr/mm grating.

The spectrum resulting from this experiment is expected to show normal Raman peaks.

The sample used to emit Raman signal was diamond powder. We focused in particular on the 1332 cm^{-1} peak [89]. For this experiment, I introduced an external disturbance in the form of a smartphone torch light shined directly onto the detector.

In this experiment, I first collected a measurement of the spectrum by setting the lock-in camera in intensity mode, which essentially operates as a standard detector. The exposure time was limited to 0.512 ms in order to avoid saturation of pixels caused by the external disturbance. This spectrum is shown in Fig. 5.3(a). The configuration of the sources, the laser and the torch, is depicted in the box above the graph. The dashed black spectrum shows the reference spectrum of the diamond powder, but it is not actually possible to see the diamond line at the same location in the blue spectrum because of the torch light which is much more powerful. The peak at 1700 cm^{-1} is not a Raman peak but a hot pixel. I then collected an image of the disturbance only, with the same exposure time, and the laser being turned off, which is shown in Fig. 5.3(b). Since the Raman emission was very small compared to the background, Fig. 5.3(a) and Fig. 5.3(b) look almost the same.

The spectrum resulting from the difference between these two measurements is shown in Fig. 5.3(c), in blue. Due to the very short exposure time, the Raman peak is almost imperceptible in this measurement.

For the lock-in measurement, I set the duration of one quarter period to the maximum allowed of 0.119 ms, and the number of cycles averaged by the detector to 32. In total, this gives an equivalent exposure time of 3.8 ms. The laser was on during the first half period, and off during the second half period. In this way, the lock-in procedure effectively removes the external disturbance at the analog level. The Raman peak was thus the only signal present in the measurement, and its magnitude was only 7 gray levels out of the 1024 available. This means that, if the camera allowed a longer cycle duration, it would be possible to integrate for a much longer time without saturation. This extrapolated result is shown by the orange plot in Fig. 5.3(c), which is given by the sum of 80 frames, effectively an exposure time of 228 ms. The quality of this spectrum is clearly improved with respect to the standard measurement.

These results are summarized in Table 5.1. The exposure times, their square roots, and the SNR for both lock-in and standard RDS are given in the table, as well as the respective ratios. Note that two values are reported for the lock-in case. In the white cells are the experimental values from a single frame. In the orange cells, the values are obtained from the sum of 80 frames, showing the experimentally extrapolated result with a longer exposure time. As expected from the theory and Eq. 5.5, the ratios of the SNRs correspond to the ratios of the square roots of the exposure times.

Table 5.1: SNR comparison for single laser RDS. The white cells correspond to experimental values from single spectra, while orange cells correspond to extrapolated results through averaging of multiple spectra.

	$T_{exposure}$ [ms]		$T_{exposure}^{1/2}$ [ms$^{1/2}$]		SNR	
Lock-in	3.8	3.8·80=228	1.95	15.1	3.04	24.18
Standard	0.512		0.71		1.09	
Ratio	7.42	442	2.74	21.12	2.78	22.1

(a)

(b)

(c)
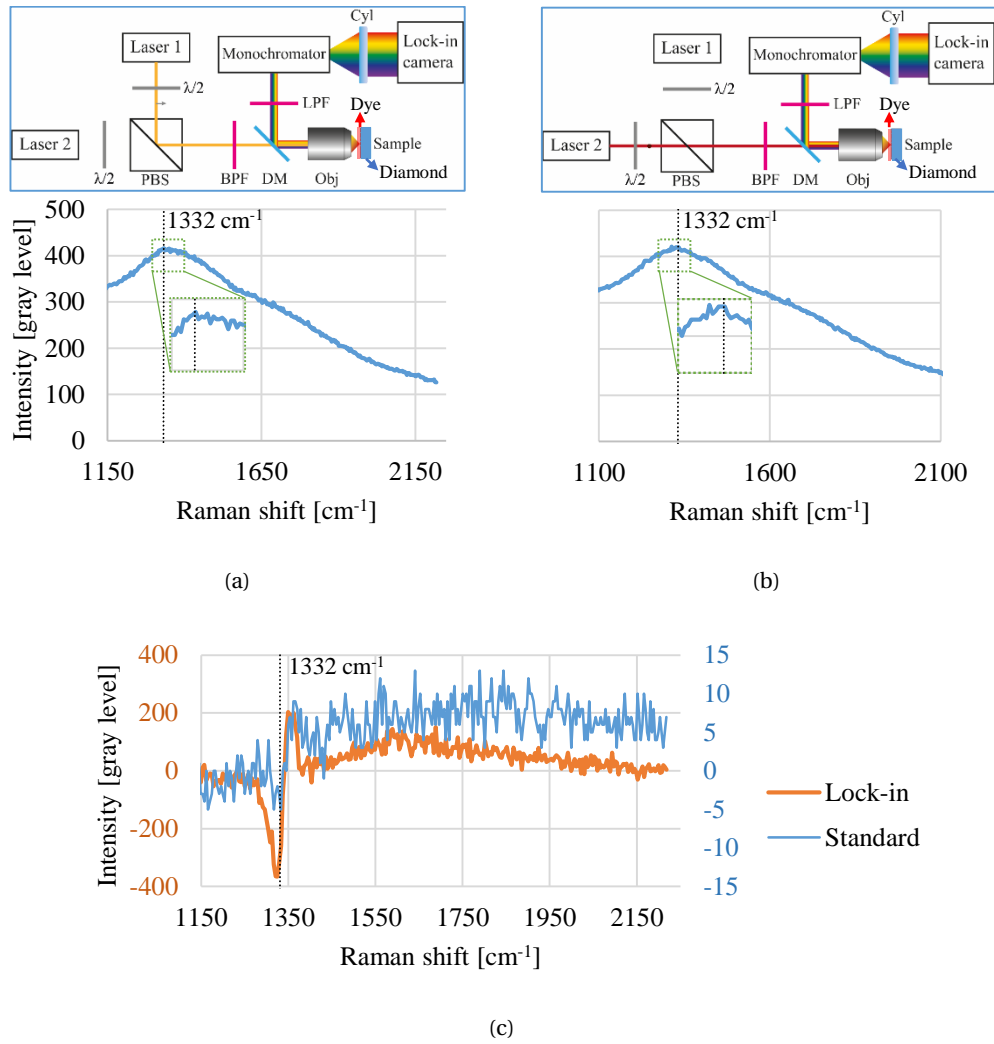
Figure 5.4: Comparison of standard and lock-in double laser RDS, with a sample made of a mixture of diamond powder and oil red. (a) Spectrum of the diamond powder and oil red mixture obtained with the first laser. The inset shows a zoomed view of where the diamond line should be. (b) Spectrum of the diamond powder and oil red mixture obtained with the second laser. The inset shows a zoomed view of where the diamond line should be. (c) Comparison of the difference spectra in lock-in (orange) and standard (blue) mode. The standard RDS spectrum is obtained as the difference between spectrum (a) and (b). The lock-in RDS spectrum is obtained by switching periodically the two laser sources synchronously to the local oscillator of the camera.

5.3.4 Double-laser RDS

In this section, I demonstrate the use of the lock-in camera for fluorescence removal in RDS. The sample used for this set of experiments is a mixture of diamond powder and oil red dye diluted in sunflower seed oil as a fluorescent disturbance. Two laser sources were used in
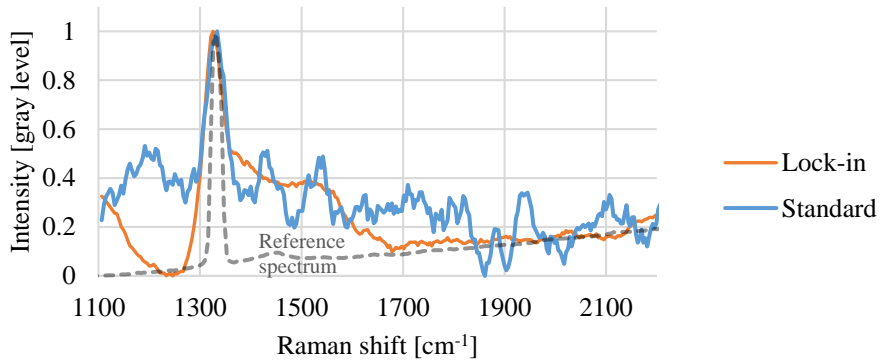
Figure 5.5: Normalized, integrated spectra for lock-in and standard RDS, obtained from the difference spectra of Fig. 5.4(c).

this case. The diode is the same for both, but their temperature was set to 22°C and 30°C, respectively. In this way, the wavelength shift between the two lasers is enough to clearly distinguish a positive and negative peak in the difference spectra.

For the standard case, I collected a spectrum for each laser, with an exposure time of 2.56 ms to avoid saturation caused by the fluorescence background. The two standard spectra are shown in Fig. 5.4(a) and (b), which also show the corresponding configuration in the boxes above. The two spectra are very similar, as expected, and the theoretical location of the diamond peak appears to shift slightly with respect to the fluorescence curve. The standard RDS spectrum is shown in Fig. 5.4(c), where it is compared to the lock-in RDS spectrum.

In the lock-in experiment, the quarter period was again set to 0.119 ms with 12 cycles being averaged. This gives an equivalent exposure time for one laser of 1.41 ms. The orange plot in Fig. 5.4(c) shows the sum of 100 lock-in RDS spectra. As in the previous set of experiments, even at the maximum exposure time, the lock-in camera is not saturated, thanks to the analog removal of the background. If it were possible to set a 100 times longer exposure time, the 10 bit detector would still not be saturated, as appears from Fig. 5.4(c).

With discrete integration I obtain the reconstructed Raman spectra for lock-in and standard RDS, which are shown in Fig. 5.5. The quality of the diamond peak in terms of noise appears to be higher for the lock-in case as expected, despite the uncovering of a spurious signal at 1500 cm^{-1}. Most likely, this is related to the presence of some residual fluorescence signal and caused by a mismatch between the two lasers emission. More spectrally pure lasers would not incur such issue.

In terms of quantitative analysis, Table 5.2 summarizes the exposure times and SNRs of the difference spectra, for a single standard RDS, a single lock-in RDS, and the extrapolated result for a 100 times longer exposure in lock-in RDS. In this case, there appears to be a 10% mismatch between the expected values of SNR ratio and calculated ones. This might be due to some additional quantization noise, as the Raman peaks were only a few gray levels in this case.

Table 5.2: SNR comparison for double laser RDS. The white cells correspond to experimental values from single spectra, while orange cells correspond to extrapolated results through averaging of multiple spectra.

	$T_{exposure}$ [ms]		$T_{exposure}^{1/2}$ [ms$^{1/2}$]		SNR	
Lock-in	1.41	$1.41 \cdot 100 = 141$	1.18	11.8	3.57	37.13
Standard	2.56		1.6		5.44	
Ratio	0.55	55	0.74	7.41	0.65	6.8

5.4 Discussion and conclusion

In this chapter, I have demonstrated the use of a lock-in camera paired with synchronized wavelength-shifted switching lasers to obtain difference Raman spectra. In particular, I showed how this method can effectively remove both external disturbances and fluorescence background through analog demodulation. This allows to obtain difference spectra that are not plagued by saturation, and the whole bit depth available can be used to encode the relevant Raman peaks.

The lock-in camera available for this work, the helicam C3, is not optimized for low signals and long exposure times, and its square aspect ratio is intended for imaging applications rather than spectroscopy. Despite this limitation, I have demonstrated that the SNR of lock-in RDS does scale compared to the standard measurement as the square root of the exposure times ratio.

In the first set of experiments in Section 3.3, I have obtained a factor of 2.78 improvement in SNR, limited by the maximum cycle duration of the camera. On the other hand, with longer exposure time, it would have been possible to improve to SNR by up to a factor of 22, as shown by the extrapolated result in Table 5.1.

In Section 5.3.4, I also demonstrated a more classic RDS application for fluorescence removal, where a long exposure time would have allowed a factor of 6.8 improvement.

Next to our experimental results, the extrapolations show how an effective system for single-shot, high-sensitivity Raman can be constructed based on the principles presented here. Indeed, the limited exposure time in standard RDS due to saturation means that in order to reach better SNRs, multiple frames have to be averaged [88]. In the case of an SNR improvement by a factor of 20, such as in Section 5.3.3, 400 frames are required. For a single point measurement, this may be feasible, but current trends in biological imaging show that Raman spectroscopy is most valuable when paired with microscopic imaging, providing hyperspectral information with a high spatial resolution. The method proposed in this chapter allows practical shifted excitation measurements even in this case, thanks to data processing requirements that are several orders of magnitude lower than digital difference methods.

To conclude, the results in this chapter demonstrate the technical feasibility of lock-in RDS in at least two configurations. Experimental results validate the expected scaling of SNR, while extrapolated result show the future potential of this technique for Raman spectroscopy in biology.

6 Conclusion and outlook

In this thesis, I introduced the concept of differential imaging, giving some examples of techniques that fall in this category. Using changes in the source of illumination to induce changes in the recorded image can be of great interest to detect specific events or components within biological samples, when a relation is found between the source modulation and the quantity of interest. This type of approach can be of great interest for biological applications, and in particular to track real-time changes in a sample. Two examples in particular were considered in this thesis: phase imaging and Raman imaging.

In Chapter 3, the sensitivity to phase of DPC was studied in detail. In particular, I demonstrated both in theory and with experiments how phase contrast can be optimised by matching the phase transfer function of the microscope to the spatial frequency content of the sample of interest. Indeed, I showed how it is possible to choose the right value of NA to improve the contrast of specific samples. Based on this result, I also showed how this analysis can be used to optimise the optical parameters of the setup for the required resolution and sensitivity. Still, with the best possible optimisation, this technique does not reach the same performance as other interferometric techniques in terms of phase sensitivity.

The limitation is inherent to the fact that a significant portion of the power collected by the detector in DPC comes from the background term, which doesn't yield any interesting information and is anyway subsequently removed. In Chapter 4, I demonstrate a new approach to DPC, that directly demodulates the phase term from the DPC images, allowing an increased single-shot CNR and improved bit efficiency. This new development brings incoherent DPC close to the results obtained in state-of-the-art interferometric phase imaging methods, leading to possible new applications, such as potentially for in-vivo retinal imaging.

In Chapter 5, I propose a similar innovation to Raman spectroscopy. Indeed, Raman spectroscopy suffers from a similar issue, given that Raman spectra typically contain both the Raman peaks of interest and a fluorescence background, which is typically stronger than the Raman emission itself. As in DPC, this can easily saturate the detector even at short exposure times, meaning that multiple frames need to be averaged to obtain a reasonable SNR. Since the fluorescence background is independent from the wavelength of excitation, while the Raman peaks shift accordingly, SERDS has been proposed as a way to reduce the effects caused by the fluorescence background, but this is only a digital computation that does not help with saturation. For this reason I demonstrated how the lock-in camera method can be successfully

applied to SERDS.

To summarise, I have proposed and demonstrated a new approach to differential imaging methods, using analog lock-in demodulation. I have shown two examples in particular, but the concept is general and can be easily applied to other scenarios. The improvements obtained in the experiments open the way for new exciting applications, where the lack of sufficient sensitivity limited what could be observed in practice.

6.1   Future outlook

The full potential of applications of DPC is still to be uncovered. Both in the standard and lock-in versions, new scenarios and use cases can be demonstrated.

One particular application of interest for DPC is the live monitoring during 3D printing. DPC has been used before for 3D reconstruction [32], using through-focus scanning. On the other hand, there has been growing interest for light based 3D printing using a rotating container [90]. This type of tomographic 3D printing uses transparent resins, and the only difference between the polymerised and non-polymerised material from an optical point of view is in the refractive index. Therefore, a phase contrast technique such as DPC could be used to monitor the state of the print, and possibly give feedback for live correction of the print model. In this case, the 3D information would come from a rotating plane of focus instead of a translating one. An algorithm for the reconstruction of the 3D object needs to be developed, and several options are available. For example, it would be possible to reconstruct each 2D focus plane separately, and reconstruct the full volume from these planes. This type of reconstruction would be fairly simple and fast to implement, but it would require an imaging system with a short depth of field, in order to avoid distortions in the reconstruction caused by the presence of out-of-focus contributions. Alternatively, an inversion algorithm based on the Radon transform may be implemented. In this case, a complex kernel would have to be included in the reconstruction, making it slower [91]. Nevertheless, this method would yield more precise results, and it could be sped up with a priori information, such as the fact that only two values of refractive index are expected, one for the polymerised and one for the non-polymerised material.

While this application is not necessarily specific to lock-in DPC given the phase differences involved, there are many instances where high sensitivity is necessary. One such example is the imaging of action potentials in retinal ganglion cells. Ganglions are neuronal cells located in the retina. When light travels through the eye, it excites the photoreceptors, which generate a chemical signal to activate the ganglion cells. These neurons fire so-called action potentials at a certain base rate when they are at rest: an action potential is an electrical signal expressed in terms of membrane potential, which travels along the axon of the neuron. Upon excitation from the photoreceptors, the firing rate increases, and vice versa [92]. The standard way of measuring such type of signals is electrophysiology, for example in the form of patch-clamp [93] or micro-electrode array [94] measurements. While these approaches provide reliable electrical measurements with high signal to noise ratio, they are fundamentally limited in terms of access to the probed area: it is necessary to locate the probe
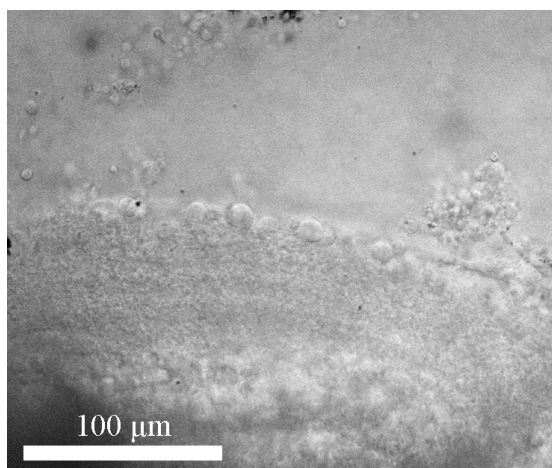
Figure 6.1: Raw DPC image of retinal ganglions.

in close proximity to the neurons, which brings inevitable interference and possibly damages the tissues [95]. More recently, new optical techniques have been proposed. In fluorescence measurements, voltage sensitive elements (e. g. molecules, dyes, proteins) are linked to the neuron and signal through fluorescence in the presence of a voltage change [95]. Fluorescence measurements provide quite good signal to noise ratio, but they still rely on the local interaction of an external chemical with the neuron, which could interfere with its normal functioning; moreover, issues like photo-bleaching and photo-toxicity must be considered. Label-free optical techniques avoid these issues by measuring the neuronal activity without an exogenous reagent. The question lies in how to translate an electrical signal into an optical signal that can actually be measured. A wealth of publications over the years show that, during the generation and propagation of action potentials, the geometrical and physical properties of the neuron body undergo some change. Most notably, there can be changes in optical path length [96–98]. Changes in optical path length have been found to range within 0.1-150 nm based on the type of neuron and source. All the label-free optical measurements that where reported used interferometric techniques [61–63, 99]. Results obtained in these publications show that sensitivity below 1 mrad is necessary to successfully detect these changes. Given the results of Chapter 4, this could be possible using lock-in DPC.

Some steps in this direction have already been taken with the help of Prof. Diego Ghezzi's group. Static images of retinal ganglion layers in ex-vivo samples have been obtained, though no action potential activity could be measured with standard DPC, as expected.

Lock-in RDS is also interesting for applications in biology. Though a more specifically targeted detector needs to become available for practical use, the possibility of performing single-shot high sensitivity Raman measurements will open new result in ex-vivo and in-vivo spectral imaging. Reducing the amount of data that needs to be stored for each spectrum will make it possible to more easily observe volumes of samples, or track changes in time.

Finally, more ways to incorporate lock-in into differential imaging methods can be developed. While two specific examples were discussed in this thesis, the concept is quite

general and can be applied in other scenarios. One example could be to use lock-in detection for polarisation imaging. Different micro- and nanoscopic features influence how polarisation properties of light are changed upon interaction with the material. When the polarisation of input light is modulated, the output image changes depending on the properties of the sample being observed. Specific correlations between the response to polarisation and the characteristics of the sample can be drawn, making polarisation imaging a versatile diagnostic tool [100]. Lock-in demodulation could be effectively used in place of digital demodulation [101], to extrapolate with high sensitivity each element of the Mueller matrix.

A DPC equations

In this appendix, I compute the DPC image formation equations, including the scaling due to magnification.

Let us consider an imaging system as in Fig. 2.3. From the theory, we have seen that the image formed at the image plane from an extended source can be expressed as:

$$I(\vec{r}_i) =$$
$$= \left(\frac{1}{\lambda^3 z f_o f_t}\right)^2 \iint \left| \iint \left[\iint \sqrt{S(\vec{r}_s)} e^{i2\pi \frac{\vec{r}_o \cdot \vec{r}_s}{\lambda z}} o(\vec{r}_o) e^{-i2\pi \frac{\vec{r}_o \cdot \vec{r}_p}{\lambda f_o}} d^2 \vec{r}_o \right] P(\vec{r}_p) e^{-i2\pi \frac{(\vec{r}_p \cdot \vec{r}_i)}{\lambda f_t}} d^2 \vec{r}_p \right|^2 d^2 \vec{r}_s,$$

(A.1)

where I is the intensity, $\vec{r}_i$ is the transverse coordinate in the image plane, λ is the source wavelength, f_o is the focal length of the objective lens, f_t is the focal length of the tube lens, $\vec{r}_o$ is the transverse coordinate in the object plane, $\vec{r}_s$ is the transverse coordinate in the source plane, $S(\vec{r}_s)$ is the profile of the illumination, z is the distance between source and object, $o(\vec{r}_o)$ is the transmittance of the sample, $\vec{r}_p$ is the transverse coordinate at the pupil plane, and $P(\vec{r}_p)$ is the pupil function.

We rewrite Eq. A.1 as:

$$I(\vec{r}_i) =$$
$$= \left(\frac{1}{\lambda^3 z f_o f_t}\right)^2 \iint S(\vec{r}_s) \left| \iint \left[\iint e^{i2\pi \frac{\vec{r}_o \cdot \vec{r}_s}{\lambda z}} o(\vec{r}_o) e^{-i2\pi \frac{\vec{r}_o \cdot \vec{r}_p}{\lambda f_o}} d^2 \vec{r}_o \right] P(\vec{r}_p) e^{-i2\pi \frac{(\vec{r}_p \cdot \vec{r}_i)}{\lambda f_t}} d^2 \vec{r}_p \right|^2 d^2 \vec{r}_s.$$

(A.2)

The most inner integral can be expressed as a Fourier transform from $\vec{r}_o$ to $\vec{r}_p/\lambda f_o$:

$$\iint e^{i2\pi \frac{\vec{r}_o \cdot \vec{r}_s}{\lambda z}} o(\vec{r}_o) e^{-i2\pi \frac{\vec{r}_o \cdot \vec{r}_p}{\lambda f_o}} d^2 \vec{r}_o = \mathfrak{F}_{\vec{r}_o \rightarrow \vec{r}_p/\lambda f_o} \left[e^{i2\pi \frac{\vec{r}_o \cdot \vec{r}_s}{\lambda z}} o(\vec{r}_o) \right] = \hat{o}\left(\frac{\vec{r}_p}{\lambda f_o} - \frac{\vec{r}_s}{\lambda z} \right), \qquad \text{(A.3)}$$

where $\hat{o}$ is the Fourier transform of o. Similarly, for the integral on $\vec{r}_p$:

$$\iint \hat{o}\left(\frac{\vec{r}_p}{\lambda f_o} - \frac{\vec{r}_s}{\lambda z}\right) P(\vec{r}_p) e^{-i2\pi \frac{(\vec{r}_p \cdot \vec{r}_i)}{\lambda f_t}} d^2 \vec{r}_p = \mathfrak{F}_{\vec{r}_p \to \vec{r}_i / \lambda f_t}\left[\hat{o}\left(\frac{\vec{r}_p}{\lambda f_o} - \frac{\vec{r}_s}{\lambda z}\right) P(\vec{r}_p)\right]. \tag{A.4}$$

We now apply a Fourier transform on both sides of Eq. A.2:

$$\mathfrak{F}_{\vec{r}_i \to \vec{u}_i}\left[I(\vec{r}_i)\right] =$$

$$= \mathfrak{F}_{\vec{r}_i \to \vec{u}_i}\left[\frac{1}{\lambda^3 z f_o f_t} \iint S(\vec{r}_s) \left|\mathfrak{F}_{\vec{r}_p \to \vec{r}_i / \lambda f_t}\left[\hat{o}\left(\frac{\vec{r}_p}{\lambda f_o} - \frac{\vec{r}_s}{\lambda z}\right) P(\vec{r}_p)\right]\right|^2 d^2 \vec{r}_s\right] = \tag{A.5}$$

$$= \frac{1}{\lambda^3 z f_o f_t} \iint S(\vec{r}_s) \mathfrak{F}_{\vec{r}_i \to \vec{u}_i}\left[\left|\mathfrak{F}_{\vec{r}_p \to \vec{r}_i / \lambda f_t}\left[\hat{o}\left(\frac{\vec{r}_p}{\lambda f_o} - \frac{\vec{r}_s}{\lambda z}\right) P(\vec{r}_p)\right]\right|^2\right] d^2 \vec{r}_s.$$

We can expand the modulus square, and use the convolution property of the Fourier transform:

$$\mathfrak{F}_{\vec{r}_i \to \vec{u}_i}\left[\left|\mathfrak{F}_{\vec{r}_p \to \vec{r}_i / \lambda f_t}\left[\hat{o}\left(\frac{\vec{r}_p}{\lambda f_o} - \frac{\vec{r}_s}{\lambda z}\right) P(\vec{r}_p)\right]\right|^2\right] =$$

$$= \mathfrak{F}_{\vec{r}_i \to \vec{u}_i}\left[\left(\mathfrak{F}_{\vec{r}_p \to \vec{r}_i / \lambda f_t}\left[\hat{o}\left(\frac{\vec{r}_p}{\lambda f_o} - \frac{\vec{r}_s}{\lambda z}\right) P(\vec{r}_p)\right]\right)\right] * \mathfrak{F}_{\vec{r}_i \to \vec{u}_i}\left[\left(\mathfrak{F}_{\vec{r}_p \to \vec{r}_i / \lambda f_t}\left[\hat{o}\left(\frac{\vec{r}_p}{\lambda f_o} - \frac{\vec{r}_s}{\lambda z}\right) P(\vec{r}_p)\right]\right)^*\right] \tag{A.6}$$

Let us now consider the first term of the convolution in Eq. A.6:

$$\mathfrak{F}_{\vec{r}_i \to \vec{u}_i}\left[\mathfrak{F}_{\vec{r}_p \to \vec{r}_i / \lambda f_t}\left[\hat{o}\left(\frac{\vec{r}_p}{\lambda f_o} - \frac{\vec{r}_s}{\lambda z}\right) P(\vec{r}_p)\right]\right] = (\lambda f_t)^2 \hat{o}\left(-\frac{f_t}{f_o} \vec{u}_i - \frac{\vec{r}_s}{\lambda z}\right) P(-\lambda f_t \vec{u}_i). \tag{A.7}$$

For the second term of the convolution we can write, keeping in mind the properties of Fourier transforms and complex conjugation:

$$\mathfrak{F}_{\vec{r}_i \to \vec{u}_i}\left[\left(\mathfrak{F}_{\vec{r}_p \to \vec{r}_i / \lambda f_t}\left[\hat{o}\left(\frac{\vec{r}_p}{\lambda f_o} - \frac{\vec{r}_s}{\lambda z}\right) P(\vec{r}_p)\right]\right)^*\right] =$$

$$= \mathfrak{F}_{\vec{r}_i \to \vec{u}_i}\left[\mathfrak{F}_{\vec{r}_p \to -\vec{r}_i / \lambda f_t}\left[\hat{o}^*\left(-\frac{\vec{r}_p}{\lambda f_o} + \frac{\vec{r}_s}{\lambda z}\right) P^*(\vec{r}_p)\right]\right] = \tag{A.8}$$

$$= (\lambda f_t)^2 \hat{o}^*\left(-\frac{f_t}{f_o} \vec{u}_i + \frac{\vec{r}_s}{\lambda z}\right) P^*(\lambda f_t \vec{u}_i).$$

The transmittance of the object is typically expressed as:

$$o(\vec{r}_o) = e^{-\mu(\vec{r}_o) + i\phi(\vec{r}_o)}. \tag{A.9}$$

We now assume that the object is "weak", meaning that we can linearise the object transmittance:

$$o(\vec{r}_o) \approx 1 - \mu(\vec{r}_o) + i\phi(\vec{r}_o),\tag{A.10}$$

so that the Fourier transform can be written as:

$$\hat{o} = \delta - \hat{\mu} + i\hat{\phi},\tag{A.11}$$

$$\hat{o^*} = \delta - \hat{\mu} - i\hat{\phi}.\tag{A.12}$$

Putting together Eq. A.7, Eq. A.8, Eq. A.11 and Eq. A.12 into Eq. A.5:

$$
\begin{aligned}
\mathfrak{F}_{\vec{r}_i \to \vec{u}_i}&\left[I(\vec{r}_i) \right] = \\
&= \left(\frac{1}{\lambda^3 z f_o f_t} \right)^2 (\lambda f_t)^4 \iint S(\vec{r}_s) \left[\hat{o}\left(-\frac{f_t}{f_o}\vec{u}_i - \frac{\vec{r}_s}{\lambda z} \right) P(-\lambda f_t \vec{u}_i) \right] * \\
&\quad \left[\hat{o^*}\left(-\frac{f_t}{f_o}\vec{u}_i + \frac{\vec{r}_s}{\lambda z} \right) P^*(\lambda f_t \vec{u}_i) \right] d^2\vec{r}_s = \\
&= \left(\frac{1}{\lambda z} \right)^2 \left(\frac{f_t}{f_o} \right)^2 \iint S(\vec{r}_s) \\
&\quad \left\{ \left[\delta\left(-\frac{f_t}{f_o}\vec{u}_i - \frac{\vec{r}_s}{\lambda z} \right) - \hat{\mu}\left(-\frac{f_t}{f_o}\vec{u}_i - \frac{\vec{r}_s}{\lambda z} \right) + i\hat{\phi}\left(-\frac{f_t}{f_o}\vec{u}_i - \frac{\vec{r}_s}{\lambda z} \right) \right] P(-\lambda f_t \vec{u}_i) \right\} * \\
&\quad \left\{ \left[\delta\left(-\frac{f_t}{f_o}\vec{u}_i + \frac{\vec{r}_s}{\lambda z} \right) - \hat{\mu}\left(-\frac{f_t}{f_o}\vec{u}_i + \frac{\vec{r}_s}{\lambda z} \right) - i\hat{\phi}\left(-\frac{f_t}{f_o}\vec{u}_i + \frac{\vec{r}_s}{\lambda z} \right) \right] P^*(\lambda f_t \vec{u}_i) \right\} d^2\vec{r}_s.
\end{aligned}
\tag{A.13}
$$

Nine convolution terms come from Eq. A.13, but we ignore the cross terms between $\hat{\mu}$ and $\hat{\phi}$, as well as the square terms [24].

What is left are the following five terms:

$$\left(\frac{f_o}{f_t} \right)^4 \left| P\left(\frac{f_o}{z}\vec{r}_s \right) \right|^2 \delta(\vec{u}_i),\tag{A.14}$$

$$-\left(\frac{f_o}{f_t} \right)^2 P\left(\frac{f_o}{z}\vec{r}_s \right) P^*\left(\lambda f_t \vec{u}_i + \frac{f_o}{z}\vec{r}_s \right) \hat{\mu}\left(-\frac{f_t}{f_o}\vec{u}_i \right),\tag{A.15}$$

$$-\left(\frac{f_o}{f_t} \right)^2 P^*\left(\frac{f_o}{z}\vec{r}_s \right) P\left(-\lambda f_t \vec{u}_i + \frac{f_o}{z}\vec{r}_s \right) \hat{\mu}\left(-\frac{f_t}{f_o}\vec{u}_i \right),\tag{A.16}$$

$$-i\left(\frac{f_o}{f_t} \right)^2 P\left(\frac{f_o}{z}\vec{r}_s \right) P^*\left(\lambda f_t \vec{u}_i + \frac{f_o}{z}\vec{r}_s \right) \hat{\phi}\left(-\frac{f_t}{f_o}\vec{u}_i \right),\tag{A.17}$$

$$i\left(\frac{f_o}{f_t}\right)^2 P^*\left(\frac{f_o}{z}\vec{r}_s\right)P\left(-\lambda f_t \vec{u}_i + \frac{f_o}{z}\vec{r}_s\right)\hat{\phi}\left(-\frac{f_t}{f_o}\vec{u}_i\right). \tag{A.18}$$

Inserting Eq. A.14 to Eq. A.18, into Eq. A.13 and summing the terms in $\hat{\mu}$ and $\hat{\phi}$ respectively, we obtain the linear DPC equation:

$$\hat{I}(\vec{u}_i) = \delta(\vec{u}_i)B + \hat{\mu}\left(-\frac{f_t}{f_o}\vec{u}_i\right)H_{abs}(\vec{u}_i) + \hat{\phi}\left(-\frac{f_t}{f_o}\vec{u}_i\right)H_{ph}(\vec{u}_i), \tag{A.19}$$

where:

$$B = \left(\frac{1}{\lambda z}\right)^2\left(\frac{f_o}{f_t}\right)^2\iint S(\vec{r}_s)\left|P\left(\frac{f_o}{z}\vec{r}_s\right)\right|d^2\vec{r}_s, \tag{A.20}$$

$$H_{\text{abs}}(\vec{u}_i) = -\left(\frac{1}{\lambda z}\right)^2\iint S(\vec{r}_s)\left[P\left(\frac{f_o}{z}\vec{r}_s\right)P^*\left(\lambda f_t \vec{u}_i + \frac{f_o}{z}\vec{r}_s\right) + P^*\left(\frac{f_o}{z}\vec{r}_s\right)P\left(-\lambda f_t \vec{u}_i + \frac{f_o}{z}\vec{r}_s\right)\right]d^2\vec{r}_s, \tag{A.21}$$

$$H_{\text{ph}}(\vec{u}_i) = -i\left(\frac{1}{\lambda z}\right)^2\iint S(\vec{r}_s)\left[P\left(\frac{f_o}{z}\vec{r}_s\right)P^*\left(\lambda f_t \vec{u}_i + \frac{f_o}{z}\vec{r}_s\right) - P^*\left(\frac{f_o}{z}\vec{r}_s\right)P\left(-\lambda f_t \vec{u}_i + \frac{f_o}{z}\vec{r}_s\right)\right]d^2\vec{r}_s. \tag{A.22}$$

It is possible to express these equations in a more compact way as:

$$H_{\text{abs}}(\vec{u}_i) =$$
$$= -\left(\frac{1}{\lambda z}\right)^2\left(\frac{z}{f_o}\right)^2\iint S\left(\frac{z}{f_o}\vec{r}_s\right)\left[P(\vec{r}_s)P^*(\lambda f_t \vec{u}_i + \vec{r}_s) + P^*(\vec{r}_s)P(-\lambda f_t \vec{u}_i + \vec{r}_s)\right]d^2\vec{r}_s =$$
$$= -\left(\frac{1}{\lambda z}\right)^2\left(\frac{z}{f_o}\right)^2(\lambda f_t)^2\left\{\left[S^*\left(\frac{z\lambda f_t}{f_o}\vec{u}_i\right)P^*(\lambda f_t \vec{u}_i)\right]\star P^*(\lambda f_t \vec{u}_i) + \right.$$
$$\left. P^*(\lambda f_t \vec{u}_i)\star\left[S\left(\frac{z\lambda f_t}{f_o}\vec{u}_i\right)P^*(\lambda f_t \vec{u}_i)\right]\right\}, \tag{A.23}$$

where $\star$ is the cross-correlation operator. We then apply the Fourier property of cross correlation, and assume S to be real:

$$H_{\text{abs}}(\vec{u}_i) =$$

$$= -\left(\frac{f_t}{f_o}\right)^2 \mathfrak{F}^{-1}\left\{\mathfrak{F}^*\left[S\left(\frac{z\lambda f_t}{f_o}\vec{u}_i\right)P^*(\lambda f_t\vec{u}_i)\right]\mathfrak{F}\left[P^*(\lambda f_t\vec{u}_i)\right]+ $$

$$\mathfrak{F}^*\left[P^*(\lambda f_t\vec{u}_i)\right]\mathfrak{F}\left[S\left(\frac{z\lambda f_t}{f_o}\vec{u}_i\right)P^*(\lambda f_t\vec{u}_i)\right]\right\}= \tag{A.24}$$

$$= -\left(\frac{f_t}{f_o}\right)^2 \mathfrak{F}^{-1}\left[\mathfrak{Re}\left\{\mathfrak{F}\left[S\left(\frac{z\lambda f_t}{f_o}\vec{u}_i\right)P^*(\lambda f_t\vec{u}_i)\right]\mathfrak{F}^*\left[P^*(\lambda f_t\vec{u}_i)\right]\right\}\right],$$

where $\mathfrak{Re}\{\cdot\}$ indicates the real part. Similarly for H_{ph}:

$$H_{\text{ph}}(\vec{u}_i) = i\left(\frac{f_t}{f_o}\right)^2 \mathfrak{F}^{-1}\left[\mathfrak{Im}\left\{\mathfrak{F}\left[S\left(\frac{z\lambda f_t}{f_o}\vec{u}_i\right)P^*(\lambda f_t\vec{u}_i)\right]\mathfrak{F}^*\left[P^*(\lambda f_t\vec{u}_i)\right]\right\}\right], \tag{A.25}$$

where $\mathfrak{Im}\{\cdot\}$ indicates the imaginary part. Notice that the pupil plane and the image plane are connected by a Fourier transform, while the source plane "at infinity" and the pupil plane are approximated to be conjugate through a dilation z/f_o, so the scalings in Eq. A.24 and A.25 are correct. Moreover, $f_t/f_o = M$ is the magnification of the microscope.

One important property is observed from Eq. A.21, setting $\vec{u}_i = 0$:

$$H_{abs}(0) = -\left(\frac{1}{\lambda z}\right)^2 \iint S(\vec{r}_s)\left[P\left(\frac{f_o}{z}\vec{r}_s\right)P^*\left(0+\frac{f_o}{z}\vec{r}_s\right)+P^*\left(\frac{f_o}{z}\vec{r}_s\right)P\left(0+\frac{f_o}{z}\vec{r}_s\right)\right]d^2\vec{r}_s = \tag{A.26}$$

$$= -2M^2 B.$$

To conclude, the image formation equations for DPC, can be summarised as:

$$\hat{I}(\vec{u}_i) = \delta(\vec{u}_i)B + \hat{\mu}(-M\vec{u}_i)H_{\text{abs}}(\vec{u}_i) + \hat{\phi}(-M\vec{u}_i)H_{\text{ph}}(\vec{u}_i),$$

$$B = \frac{|H_{\text{abs}}(0)|}{2M^2},$$

$$H_{\text{abs}}(\vec{u}_i) = -M^2\mathfrak{F}^{-1}\left[\mathfrak{Re}\left\{\mathfrak{F}\left[S(z\lambda M\vec{u}_i)P^*(\lambda f_t\vec{u}_i)\right]\mathfrak{F}^*\left[P^*(\lambda f_t\vec{u}_i)\right]\right\}\right], \tag{A.27}$$

$$H_{\text{ph}}(\vec{u}_i) = iM^2\mathfrak{F}^{-1}\left[\mathfrak{Im}\left\{\mathfrak{F}\left[S(z\lambda M\vec{u}_i)P^*(\lambda f_t\vec{u}_i)\right]\mathfrak{F}^*\left[P^*(\lambda f_t\vec{u}_i)\right]\right\}\right].$$

B Quantitative DPC simulation

To perform the DPC simulations shown in Chapter 3, a MATLAB®algorithm was used. More details on this are given here for the interested reader. The equations that describe the forward problem of image formation in DPC have been established in Appendix A, summarised in Eq. A.27.

The operations to calculate the background, transfer functions, and image, are straight-forward and can be easily implemented in Matlab®using matrix multiplications and discrete Fourier transforms. Nevertheless, some care must be taken, as the transforms are performed in Matlab®over a generic system of coordinates, so appropriate factors must be used to retain the quantitative nature of the simulation [102]. As a consequence, the previous equations can be implemented in Matlab®as follows:

$$\bar{\bar{I}} = B + \text{IFFT}\left\{ dx_o^2 \text{FFT}\left\{ \bar{\bar{\mu}} \right\} \cdot \bar{\bar{H}}_{abs} \right\} + \text{IFFT}\left\{ dx_o^2 \text{FFT}\left\{ \bar{\bar{\phi}} \right\} \cdot \bar{\bar{H}}_{ph} \right\}, \tag{B.1}$$

$$B = \frac{\max| \bar{\bar{H}}_{\text{abs}} |}{2M^2}, \tag{B.2}$$

$$\bar{\bar{H}}_{\text{abs}} = -\frac{2}{dx_o^2}\text{IFFT}\left\{ \text{Re}\left[\text{FFT}\left(\bar{\bar{P}} \right)^* \cdot \text{FFT}\left(\bar{\bar{P}} \cdot \bar{\bar{S}} \right) \right] \right\}, \tag{B.3}$$

$$\bar{\bar{H}}_{\text{ph}} = \frac{2}{dx_o^2}\text{IFFT}\left\{ \text{Im}\left[\text{FFT}\left(\bar{\bar{P}} \right)^* \cdot \text{FFT}\left(\bar{\bar{P}} \cdot \bar{\bar{S}} \right) \right] \right\}, \tag{B.4}$$

Where $\bar{\bar{\cdot}}$ indicates a 2D matrix, FFT and IFFT are the 2D discrete Fourier transform and inverse discrete Fourier transform operators, dx_o is the pixel size (assuming a square pixel) in the object space, and $\cdot$ indicates an element-wise matrix multiplication. Further care should be taken when using the FFT and IFFT operators to make sure whether the frequency coordinates are centered. In our simulations, the absorption profile of the sample is assumed to be null.

To obtain the quantitative simulated images, we used the measured illumination profile and the measured NA for $\bar{\bar{P}}$ and $\bar{\bar{S}}$ to calculate $\bar{\bar{H}}_{\text{abs}}$ and $\bar{\bar{H}}_{\text{ph}}$. For the simulation to yield the same result as the experiment, the background term B should be the same as the average background intensity in the experiment. Thus, we assign to B the value of the background

intensity, and we use the relation between B and $\bar{\bar{H}}_{\text{abs}}$ in Eq. B.2 to normalize the transfer functions as follows:

$$\bar{\bar{H}}_{\text{abs,norm}} = \frac{2M^2 B}{\max\left|\bar{\bar{H}}_{\text{abs}}\right|} \, \bar{\bar{H}}_{\text{abs}}, \tag{B.5}$$

$$\bar{\bar{H}}_{\text{ph,norm}} = \frac{2M^2 B}{\max\left|\bar{\bar{H}}_{\text{abs}}\right|} \, \bar{\bar{H}}_{\text{ph}}, \tag{B.6}$$

In this way, the simulated image corresponds to the real pixel values of the experiments, including the background. This is very important for the last step: using the algorithm for noise modelling [49, 50], we map the intensity-dependent noise $\sigma(I)$. Since the simulated image is consistent with the range of gray levels of the camera, the contrast in the simulated image can be directly compared with the standard deviation of the noise at the background intensity, $\sigma(B)$. This simulation allows to obtain quantitative CNR and sensitivity values, given the knowledge of some basic optical parameters of the setup, namely the magnification, pixel size, NA, wavelength and source profile (measured or analytical).

Bibliography

[1] R. Segev, J. Goodhouse, J. Puchalla, and n. Berry, M. J., "Recording spikes from a large fraction of the ganglion cells in a retinal patch," *Nature Neuroscience*, vol. 7, no. 10, pp. 1154–61, 2004.

[2] D. Carpentras, T. Laforest, M. Künzi, and C. Moser, "Effect of backscattering in phase contrast imaging of the retina," *Optics Express*, vol. 26, no. 6, pp. 6785–6795, 2018.

[3] P. Casteleiro Costa, P. Ledwig, A. Bergquist, J. Kurtzberg, and F. E. Robles, "Noninvasive white blood cell quantification in umbilical cord blood collection bags with quantitative oblique back-illumination microscopy," *Transfusion*, vol. 60, no. 3, pp. 588–597, 2020.

[4] H.-H. Chen, Y.-Z. Lin, and Y. Luo, "Isotropic differential phase contrast microscopy for quantitative phase bio-imaging," *Journal of Biophotonics*, vol. 11, no. 8, p. e201700364, 2018.

[5] Y.-H. Chuang, Y.-Z. Lin, S. Vyas, Y.-Y. Huang, J. A. Yeh, and Y. Luo, "Multi-wavelength quantitative differential phase contrast imaging by radially asymmetric illumination," *Optics Letters*, vol. 44, no. 18, pp. 4542–4545, 2019.

[6] Y. Fan, J. Sun, Q. Chen, J. Zhang, and C. Zuo, "Wide-field anti-aliased quantitative differential phase contrast microscopy," *Optics Express*, vol. 26, no. 19, p. 25129, 2018.

[7] W. Lee, J. H. Choi, S. Ryu, D. Jung, J. Song, J. S. Lee, and C. Joo, "Color-coded led microscopy for quantitative phase imaging: Implementation and application to sperm motility analysis," *Methods*, vol. 136, pp. 66–74, 2018.

[8] Z. F. Phillips, M. Chen, and L. Waller, "Single-shot quantitative phase microscopy with color-multiplexed differential phase contrast (cdpc)," *PLoS One*, vol. 12, no. 2, p. e0171228, 2017.

[9] L. Tian, Z. Liu, L.-H. Yeh, M. Chen, J. Zhong, and L. Waller, "Computational illumination for high-speed in vitro fourier ptychographic microscopy," *Optica*, vol. 2, no. 10, pp. 904–911, 2015.

[10] C. Yurdakul, O. Avci, A. Matlock, A. J. Devaux, M. V. Quintero, E. Ozbay, R. A. Davey, J. H. Connor, W. C. Karl, L. Tian, and M. S. Ünlü, "High-throughput, high-resolution interferometric light microscopy of biological nanoparticles," *ACS Nano*, vol. 14, no. 2, pp. 2002–2013, 2020.

Bibliography

[11] T. Laforest, M. Künzi, L. Kowalczuk, D. Carpentras, F. Behar-Cohen, and C. Moser, "Transscleral optical phase imaging of the human retina," *Nature Photonics*, vol. 14, pp. 439–445, 2020.

[12] R. S. Jonnal, O. P. Kocaoglu, R. J. Zawadzki, Z. Liu, D. T. Miller, and J. S. Werner, "A review of adaptive optics optical coherence tomography: Technical advances, scientific applications, and the future," *Investigative Ophthalmology & Visual Science*, vol. 57, no. 9, pp. OCT51–68, 2016.

[13] D. Wei, S. Chen, and Q. Liu, "Review of fluorescence suppression techniques in raman spectroscopy," *Applied Spectroscopy Reviews*, vol. 50, no. 5, pp. 387–406, 2015.

[14] J. Kostamovaara, J. Tenhunen, M. Kögler, I. Nissinen, J. Nissinen, and P. Keränen, "Fluorescence suppression in raman spectroscopy using a time-gated cmos spad," *Optics Express*, vol. 21, no. 25, pp. 31632–31645, 2013.

[15] R. R. Jones, D. C. Hooper, L. Zhang, D. Wolverson, and V. K. Valev, "Raman techniques: Fundamentals and frontiers," *Nanoscale Research Letters*, vol. 14, no. 1, p. 231, 2019.

[16] A. J. Driscoll, M. H. Harpster, and P. A. Johnson, "The development of surface-enhanced raman scattering as a detection modality for portable in vitro diagnostics: progress and challenges," *Physical Chemistry Chemical Physics*, vol. 15, no. 47, pp. 20415–20433, 2013.

[17] R. Strack, "Imaging without the labels," *Nature Methods*, vol. 19, no. 1, pp. 30–30, 2022.

[18] B. B. Praveen, P. C. Ashok, M. Mazilu, A. Riches, S. Herrington, and K. Dholakia, "Fluorescence suppression using wavelength modulated raman spectroscopy in fiber-probe-based tissue analysis," *Journal of Biomedical Optics*, vol. 17, no. 7, p. 077006, 2012.

[19] B. B. Praveen, M. Mazilu, R. F. Marchington, C. S. Herrington, A. Riches, and K. Dholakia, "Optimisation of wavelength modulated raman spectroscopy: towards high throughput cell screening," *PLoS One*, vol. 8, no. 6, p. e67211, 2013.

[20] M. Born and E. Wolf, *Principles of Optics: Electromagnetic Theory of Propagation, Interference and Diffraction of Light*. Cambridge: Cambridge University Press, 7 ed., 1999.

[21] J. W. Goodman, *Introduction to Fourier optics*, vol. 1. Englewood: Roberts & Co. Publishers, 3 ed., 2005.

[22] G. Popescu, *Quantitative Phase Imaging of Cells and Tissues*. New York: McGraw-Hill, 1 ed., 2011.

[23] M. Nazarathy and J. Shamir, "Fourier optics described by operator algebra," *Journal of the Optical Society of America*, vol. 70, pp. 150–159, Feb 1980.

[24] L. Tian and L. Waller, "Quantitative differential phase contrast imaging in an led array microscope," *Optics Express*, vol. 23, no. 9, pp. 11394–403, 2015.

[25] F. Zernike, "Phase contrast, a new method for the microscopic observation of transparent objects, part i," *Physica*, vol. 9, pp. 686–698, 1942.

[26] F. Zernike, "Phase contrast, a new method for the microscopic observation of transparent objects, part ii," *Physica*, vol. 9, pp. 974–986, 1942.

[27] C. J. R. Sheppard, "Defocused transfer function for a partially coherent microscope and application to phase retrieval," *Journal of the Optical Society of America A*, vol. 21, pp. 828–831, May 2004.

[28] D. K. Hamilton and C. J. R. Sheppard, "Differential phase-contrast in scanning optical microscopy," *Journal of Microscopy-Oxford*, vol. 133, no. Jan, pp. 27–39, 1984. Rz085 Times Cited:88 Cited References Count:10.

[29] D. K. Hamilton, C. J. R. Sheppard, and T. Wilson, "Improved imaging of phase gradients in scanning optical microscopy," *Journal of Microscopy-Oxford*, vol. 135, no. 3, pp. 275–286, 1984.

[30] B. Kachar, "Asymmetric illumination contrast: a method of image formation for video light microscopy," *Science*, vol. 227, no. 4688, pp. 766–8, 1985.

[31] S. B. Mehta and C. J. R. Sheppard, "Quantitative phase-gradient imaging at high resolution with asymmetric illumination-based differential phase contrast," *Optics Letters*, vol. 34, no. 13, pp. 1924–1926, 2009.

[32] L. Tian, J. Wang, and L. Waller, "3d differential phase-contrast microscopy with computational illumination using an led array," *Optics Letters*, vol. 39, no. 5, pp. 1326–9, 2014.

[33] M. H. Jenkins and T. K. Gaylord, "Quantitative phase microscopy via optimized inversion of the phase optical transfer function," *Applied Optics*, vol. 54, no. 28, pp. 8566–79, 2015.

[34] P. C. Hansen, "The l-curve and its use in the numerical treatment of inverse problem," 2001.

[35] G. H. Golub, P. C. Hansen, and D. P. O'Leary, "Tikhonov regularization and total least squares," *SIAM Journal on Matrix Analysis and Applications*, vol. 21, no. 1, pp. 185–194, 1999.

[36] D. P. O'Leary, "Near-optimal parameters for tikhonov and other regularization methods," *SIAM Journal on Scientific Computing*, vol. 23, no. 4, pp. 1161–1171, 2001.

[37] D. Gabor, "A new microscopic principle," *Nature*, vol. 161, pp. 777–778, 1948.

[38] J. Hecht, "Holography and the laser," *Optics & Photonics News*, vol. 21, pp. 34–41, Jul 2010.

[39] M. Testorf and A. W. Lohmann, "Holography in phase space," *Applied Optics*, vol. 47, pp. A70–A77, Feb 2008.

[40] T. Zhang and I. Yamaguchi, "Three-dimensional microscopy with phase-shifting digital holography," *Optics Letters*, vol. 23, no. 15, pp. 1221–1223, 1998.

[41] I. Yamaguchi and T. Zhang, "Phase-shifting digital holography," *Optics Letters*, vol. 22, no. 16, pp. 1268–1270, 1997.

[42] G. Popescu, L. P. Deflores, J. C. Vaughan, K. Badizadegan, H. Iwai, R. R. Dasari, and M. S. Feld, "Fourier phase microscopy for investigation of biological structures and dynamics," *Optics Letters*, vol. 29, no. 21, pp. 2503–2505, 2004.

[43] N. Lue, W. Choi, G. Popescu, T. Ikeda, R. R. Dasari, K. Badizadegan, and M. S. Feld, "Quantitative phase imaging of live cells using fast fourier phase microscopy," *Applied Optics*, vol. 46, no. 10, pp. 1836–1842, 2007.

[44] J. W. Goodman, *Statistical Optics*. New York: John Wiley & Sons, 2 ed., 2015.

[45] Y. Fan, J. Sun, Q. Chen, X. Pan, L. Tian, and C. Zuo, "Optimal illumination scheme for isotropic quantitative differential phase contrast microscopy," *Photonics Research*, vol. 7, no. 8, pp. 890–904, 2019.

[46] W. Lee, D. Jung, S. Ryu, and C. Joo, "Single-exposure quantitative phase imaging in color-coded led microscopy," *Optics Express*, vol. 25, no. 7, pp. 8398–8411, 2017.

[47] H. Lu, J. Chung, X. Ou, and C. Yang, "Quantitative phase imaging and complex field reconstruction by pupil modulation differential phase contrast," *Optics Express*, vol. 24, no. 22, pp. 25345–25361, 2016.

[48] Y. Ma, S. Y. Guo, Y. Pan, R. Fan, Z. J. Smith, S. Lane, and K. Q. Chu, "Quantitative phase microscopy with enhanced contrast and improved resolution through ultra-oblique illumination (uo-qpm)," *Journal of Biophotonics*, vol. 12, no. 10, p. e201900011, 2019.

[49] L. Azzari and A. Foi, "Gaussian-cauchy mixture modeling for robust signal-dependent noise estimation," in *IEEE International Conference on Acoustics, Speech and Signal Processing (ICASSP)*, pp. 5357–5361, 2014.

[50] A. Foi, M. Trimeche, V. Katkovnik, and K. Egiazarian, "Practical poissonian-gaussian noise modeling and fitting for single-image raw-data," *IEEE Transactions on Image Processing*, vol. 17, no. 10, pp. 1737–1754, 2008.

[51] F. Timischl, "The contrast-to-noise ratio for image quality evaluation in scanning electron microscopy," *Scanning*, vol. 37, no. 1, pp. 54–62, 2015.

[52] H. Jiang, N. Lu, and L. Yao, "A high-fidelity haze removal method based on hot for visible remote sensing images," *Remote Sensing*, vol. 8, no. 10, p. 844, 2016.

[53] P. Hosseini, R. J. Zhou, Y. H. Kim, C. Peres, A. Diaspro, C. F. Kuang, Z. Yaqoob, and P. T. C. So, "Pushing phase and amplitude sensitivity limits in interferometric microscopy," *Optics Letters*, vol. 41, no. 7, pp. 1656–1659, 2016.

[54] M. Chen, L. Tian, and L. Waller, "3d differential phase contrast microscopy," *Biomedical Optics Express*, vol. 7, no. 10, pp. 3940–3950, 2016.

[55] P. C. Hansen and D. P. Oleary, "The use of the l-curve in the regularization of discrete ill-posed problems," *Siam Journal on Scientific Computing*, vol. 14, no. 6, pp. 1487–1503, 1993.

[56] G. Popescu, T. Ikeda, R. R. Dasari, and M. S. Feld, "Diffraction phase microscopy for quantifying cell structure and dynamics," *Optics Letters*, vol. 31, no. 6, pp. 775–777, 2006.

[57] R. Shang, S. Chen, and Y. Zhu, "High-sensitivity quantitative phase microscopy using spectral encoding," in *Frontiers in Optics* (O. T. Digest, ed.), p. paper FW4G.3, 2014.

[58] Z. Wang, L. Millet, M. Mir, H. F. Ding, S. Unarunotai, J. Rogers, M. U. Gillette, and G. Popescu, "Spatial light interference microscopy (slim)," *Optics Express*, vol. 19, no. 2, pp. 1016–1026, 2011.

[59] R. Ling, W. Tahir, H. Y. Lin, H. Lee, and L. Tian, "High-throughput intensity diffraction tomography with a computational microscope," *Biomedical Optics Express*, vol. 9, no. 5, pp. 2130–2141, 2018.

[60] C. Bonati, T. Laforest, M. Kunzi, and C. Moser, "Phase sensitivity in differential phase contrast microscopy: limits and strategies to improve it," *Optics Express*, vol. 28, no. 22, pp. 33767–33783, 2020.

[61] S. Batabyal, S. Satpathy, L. Bui, Y. T. Kim, S. Mohanty, R. Bachoo, and D. P. Dave, "Label-free optical detection of action potential in mammalian neurons," *Biomedical Optics Express*, vol. 8, no. 8, pp. 3700–3713, 2017.

[62] T. Ling, K. C. Boyle, G. Goetz, P. Zhou, Y. Quan, F. S. Alfonso, T. W. Huang, and D. Palanker, "Full-field interferometric imaging of propagating action potentials," *Light, Science & Applications*, vol. 7, no. 107, 2018.

[63] T. Ling, K. C. Boyle, V. Zuckerman, T. Flores, C. Ramakrishnan, K. Deisseroth, and D. Palanker, "High-speed interferometric imaging reveals dynamics of neuronal deformation during the action potential," *Proceedings of the National Academy of Sciences of the United States of America*, vol. 117, no. 19, pp. 10278–10285, 2020.

[64] S. Oh, C. Fang-Yen, W. Choi, Z. Yaqoob, D. Fu, Y. Park, R. R. Dassari, and M. S. Feld, "Label-free imaging of membrane potential using membrane electromotility," *Biophysical Journal*, vol. 103, no. 1, pp. 11–18, 2012.

Bibliography

[65] G. Goetz, T. Ling, T. Gupta, S. Kang, J. Wang, P. D. Gregory, B. H. Park, and D. Palanker, "Interferometric mapping of material properties using thermal perturbation," *Proceedings of the National Academy of Sciences of the United States of America*, vol. 115, no. 11, pp. E2499–E2508, 2018.

[66] B. Bhaduri, C. Edwards, H. Pham, R. J. Zhou, T. H. Nguyen, L. L. Goddard, and G. Popescu, "Diffraction phase microscopy: principles and applications in materials and life sciences," *Advances in Optics and Photonics*, vol. 6, no. 1, pp. 57–119, 2014.

[67] S. Beer, S. Waldis, and P. Seitz, "Video-rate optical coherence tomography imaging with smart pixels," in *Optical Coherence Tomography and Coherence Techniques* (W. Drexler, ed.), vol. 5140, SPIE, 2003.

[68] S. Beer, P. Zeller, N. Blanc, F. Lustenberger, and P. Seitz, "Smart pixels for real-time optical coherence tomography," in *Electronic Imaging* (SPIE, ed.), vol. 5302 of *Three-Dimensional Image Capture and Applications VI*, p. 21, 2004.

[69] S. Beer and P. Seitz, "Real-time tomographic imaging without x-rays: A smart pixel array with massively parallel signal processing for real-time optical coherence tomography performing close to the physical limits," in *2005 PhD Research in Microelectronics and Electronics, Vols 1 and 2, Proceedings*, pp. 335–338, 2005.

[70] B. Buttgen and P. Seitz, "Robust optical time-of-flight range imaging based on smart pixel structures," in *IEEE Transactions on Circuits and Systems I: Regular Papers*, vol. 55, pp. 1512–1525, 2008.

[71] F. M. Dickey, M. Zimmermann, D. L. Shealy, N. Lindlein, R. Voelkel, and K. J. Weible, "Microlens laser beam homogenizer: from theory to application," in *Photonic Devices + Applications*, vol. 6663, p. 666302, Proc. SPIE, 2007.

[72] P. Rostron, S. Gaber, and D. Gaber, "Raman spectroscopy, a review," *International Journal of Engineering and Technical Research*, vol. 6, no. 1, 2016.

[73] C. V. Raman and K. S. Krishnan, "Polarisation of scattered light-quanta," *Nature*, vol. 122, no. 3066, pp. 169–169, 1928.

[74] V. D'Ippolito, G. B. Andreozzi, D. Bersani, and P. P. Lottici, "Raman fingerprint of chromate, aluminate and ferrite spinels," *Journal of Raman Spectroscopy*, vol. 46, no. 12, pp. 1255–1264, 2015.

[75] A. Kudelski, "Analytical applications of raman spectroscopy," *Talanta*, vol. 76, no. 1, pp. 1–8, 2008.

[76] N. Emmanuel, R. B. Nair, B. Abraham, and K. Yoosaf, "Fabricating a low-cost raman spectrometer to introduce students to spectroscopy basics and applied instrument design," *Journal of Chemical Education*, vol. 98, no. 6, pp. 2109–2116, 2021.

[77] H. J. Butler, L. Ashton, B. Bird, G. Cinque, K. Curtis, J. Dorney, K. Esmonde-White, N. J. Fullwood, B. Gardner, P. L. Martin-Hirsch, M. J. Walsh, M. R. McAinsh, N. Stone, and F. L. Martin, "Using raman spectroscopy to characterize biological materials," *Nature Protocols*, vol. 11, no. 4, pp. 664–687, 2016.

[78] R. B. Versteeg, J. Zhu, P. Padmanabhan, C. Boguschewski, R. German, M. Goedecke, P. Becker, and P. H. M. van Loosdrecht, "A tunable time-resolved spontaneous raman spectroscopy setup for probing ultrafast collective excitation and quasiparticle dynamics in quantum materials," *Structural Dynamics*, vol. 5, no. 4, 2018.

[79] B. Durrant, M. Trappett, D. Shipp, and I. Notingher, "Recent developments in spontaneous raman imaging of living biological cells," *Current Opinion In Chemical Biology*, vol. 51, pp. 138–145, 2019.

[80] Z. Q. Li, Z. Li, Q. Chen, A. Ramos, J. Zhang, J. P. Boudreaux, R. Thiagarajan, Y. Bren-Mattison, M. E. Dunham, A. J. McWhorter, X. Li, J. M. Feng, Y. P. Li, S. M. Yao, and J. Xu, "Detection of pancreatic cancer by convolutional-neural-network-assisted spontaneous raman spectroscopy with critical feature visualization," *Neural Networks*, vol. 144, pp. 455–464, 2021.

[81] A. P. Shreve, N. J. Cherepy, and R. A. Mathies, "Effective rejection of fluorescence interference in raman-spectroscopy using a shifted excitation difference technique," *Applied Spectroscopy*, vol. 46, no. 4, pp. 707–711, 1992.

[82] P. A. Mosier-Boss, S. H. Lieberman, and R. Newbery, "Fluorescence rejection in raman spectroscopy by shifted-spectra, edge detection, and fft filtering techniques," *Applied Spectroscopy*, vol. 49, no. 5, 1995.

[83] M. A. D. Martins, D. G. Ribeiro, E. A. P. dos Santos, A. A. Martin, A. Fontes, and H. D. Martinho, "Shifted-excitation raman difference spectroscopy for in vitro and in vivo biological samples analysis," *Biomedical Optics Express*, vol. 1, no. 2, pp. 617–626, 2010.

[84] M. Chen, N. McReynolds, E. C. Campbell, M. Mazilu, J. Barbosa, K. Dholakia, and S. J. Powis, "The use of wavelength modulated raman spectroscopy in label-free identification of t lymphocyte subsets, natural killer cells and dendritic cells," *PLoS One*, vol. 10, no. 5, p. e0125158, 2015.

[85] K. Sowoidnich, M. Towrie, and P. Matousek, "Lock-in detection in raman spectroscopy with charge-shifting ccd for suppression of fast varying backgrounds," *Journal of Raman Spectroscopy*, 2019.

[86] A. C. De Luca, M. Mazilu, A. Riches, C. S. Herrington, and K. Dholakia, "Online fluorescence suppression in modulated raman spectroscopy," *Analytical Chemistry*, vol. 82, no. 2, pp. 738–45, 2010.

[87] C.-S. Liao, M. N. Slipchenko, P. Wang, J. Li, S.-Y. Lee, R. A. Oglesbee, and J.-X. Cheng, "Microsecond scale vibrational spectroscopic imaging by multiplex stimulated raman scattering microscopy," *Light, Science & Applications*, vol. 4, p. e265, 2015.

[88] C. Bonati, D. Loterie, T. Laforest, and C. Moser, "Lock-in incoherent differential phase contrast imaging," *Photonics Research*, vol. 10, no. 1, pp. 237–247, 2022.

[89] R. S. Krishnan, "Raman spectrum of diamond," *Nature*, vol. 155, no. 3928, pp. 171–171, 1945.

[90] D. Loterie, P. Delrot, and C. Moser, "High-resolution tomographic volumetric additive manufacturing," *Nature Communications*, vol. 11, no. 1, p. 852, 2020.

[91] O. Koskela, T. Montonen, B. Belay, E. Figueiras, S. Pursiainen, and J. Hyttinen, "Gaussian light model in brightfield optical projection tomography," *Scientific Reports*, vol. 9, no. 1, p. 13934, 2019.

[92] L. A. Remington, *Clinical Anatomy and Physiology of the Visual System.* Butterworth-Heinemann, 3 ed., 2012.

[93] B. Sakmann and E. Neher, "Patch clamp techniques for studying ionic channels in excitable membranes," *Annual Review of Physiology*, vol. 46, pp. 455–72, 1984.

[94] J. Dunlop, M. Bowlby, R. Peri, D. Vasilyev, and R. Arias, "High-throughput electrophysiology: an emerging paradigm for ion-channel screening and physiology," *Nature Reviews Drug Discovery*, vol. 7, no. 4, pp. 358–68, 2008.

[95] M. Scanziani and M. Hausser, "Electrophysiology in the age of light," *Nature*, vol. 461, no. 7266, pp. 930–9, 2009.

[96] T. Akkin, D. P. Dave, T. E. Milner, and H. G. Rylander, "Detection of neural activity using phase-sensitive optical low-coherence reflectometry," *Optics Express*, vol. 12, no. 11, pp. 2377–2386, 2004.

[97] C. Fang-Yen, M. C. Chu, H. S. Seung, R. R. Dasari, and M. S. Feld, "Noncontact measurement of nerve displacement during action potential with a dual-beam low-coherence interferometer," *Optics Letters*, vol. 29, no. 17, pp. 2028–2030, 2004.

[98] M. A. Choma, A. K. Ellerbee, C. H. Yang, T. L. Creazzo, and J. A. Izatt, "Spectral-domain phase microscopy," *Optics Letters*, vol. 30, no. 10, pp. 1162–1164, 2005.

[99] M. Q. Tong, M. M. Hasan, S. S. Lee, M. R. Haque, D. H. Kim, M. S. Islam, M. E. Adams, and B. H. Park, "Oct intensity and phase fluctuations correlated with activity-dependent neuronal calcium dynamics in the drosophila cns [invited]," *Biomedical Optics Express*, vol. 8, no. 2, pp. 726–735, 2017.

[100] H. He, R. Liao, N. Zeng, P. Li, Z. Chen, X. Liu, and H. Ma, "Mueller matrix polarimetry—an emerging new tool for characterizing the microstructural feature of complex biological specimen," *Journal of Lightwave Technology*, vol. 37, no. 11, 2019.

[101] O. Arteaga, M. Baldrís, J. Antó, A. Canillas, E. Pascual, and E. Bertran, "Mueller matrix microscope with a dual continuous rotating compensator setup and digital demodulation," *Applied Optics*, vol. 53, no. 10, pp. 2236–2245, 2014.

[102] D. Voelz, *Computational Fourier Optics: A MATLAB Tutorial.* SPIE Press, 2011.

Chiara Bonati

📱 (+41) 0783152821
✉ chiara.bonati93@gmail.com
in chiara-bonati

Experience

2018–Present **Doctoral Research Assistant**, *École Polytechnique Fédérale de Lausanne*, Lausanne, Switzerland
- Designed and developed a Differential Phase Contrast microscope with dual Fourier plane/image plane detection and variable numerical aperture;
- Developed full software control in LabView, allowing customisable illumination patterns and automatic synchronised recording;
- Designed and developed a novel Differential Phase Contrast microscope based on in-pixel lock-in demodulation, with 7-fold phase sensitivity improvement at 1400 fps. Currently this is the best performance of incoherent based phase microscopy;
- Supervised multiple Master student projects.

March 2017– December 2017 **Master Thesis Project**, *Politecnico di Milano*, Milan, Italy
Development and characterisation of a compact multiwavelength time resolved spectroscopy system for thyroid cancer screening
Thesis supervisor: Prof. Davide Contini
- Contributed to H2020 European project LUCA;
- Designed and optimized a free-space optical coupling system for the alignment of a set of lasers with tight mechanical constraints;
- Carried out a preliminary study on the application of the diffusion equation to a phantom-based model of the neck;
- Proposed a procedure for the analysis of Near Infrared Time Resolved Spectroscopy data from the neck.

Summer 2015 **Internship**, *Tyndall National Institute*, Cork, Ireland
Setup and characterisation of supercontinuum laser source for InP waveguides testing.

Summer 2014 **Internship**, *Tyndall National Institute*, Cork, Ireland
Modeling and characterisation of GaN micro LEDs for optimised emission.

Summer 2010 **Internship**, *Giornale di Bergamo newspaper*, Bergamo, Italy

2008–2014 **Physics and Maths high school private tutoring**

Education

2018–Present **PhD Candidate**, *École Polytechnique Fédérale de Lausanne*, Lausanne, Switzerland
Differential Imaging for Phase Contrast Microscopy and Raman Spectroscopy
Supervisor: Prof. Christophe Moser

2015–2017 **Master of Science in Engineering Phyisics - Photonics and Nanooptics**, *Politecnico di Milano*, Milan, Italy, *Final grade − 110 cum laude/110*

2012–2015 **Bachelor of Science in Engineering Physics**, *Politecnico di Milano*, Milan, Italy, *Final grade − 110/110*

Certifications

Prince2 Foundation Certificate in Project Management

Computer skills

Advanced Zemax, LabView, MatLab
Intermediate C/C++ programming, WinLens, PreDesigner
Basic R, Simulink, CAD

Languages

Italian	Mothertongue
English	C1 level - TOEIC 990/990
French	Intermediate knowledge

Publications

C. Bonati, D. Loterie, T. Laforest, and C. Moser, *"Lock-in incoherent differential phase contrast imaging,"* Photon. Res. 10, 237-247 (2022)

C. Bonati, T. Laforest, M. Kunzi, and C. Moser, *"Phase sensitivity in differential phase contrast microscopy: limits and strategies to improve it,"* Opt. Express 28, 33767-33783 (2020)

Conferences

2022	**SPIE Photonics West**, *"Lock-In Amplified Differential Phase Contrast"*
2021	**Annual Meeting of the Biomedical Photonics Network**, *"Lock-In Amplified Differential Phase Contrast"*
	OSA Imaging and Applied Optics Congress, *"Lock-In Amplified Differential Phase Contrast"*
	SPIE Photonics West, *"Sensitivity in differential phase contrast - limits and strategies to improve it"*
2020	**OSA Imaging and Applied Optics Congress**, *"Sensitivity in DPC: Assessing the Limits"*

Volunteering

2019-2020	**EPFL Photonics Chapter Committee Member**, Lausanne, Switzerland
	Organisation of social events for the photonics community at EPFL
2010–2011	**Volunteering as tour guide**, *BergamoScienza scientific festival*, Bergamo, Italy

- Tour guide for the laboratory "La scienza dei giocattoli" ("The science of toys") organized by ForMath Association;
- Tour guide for the exhibition "Elements: the beauty of Chemistry" organized with the Science Gallery, Dublin.

Interests

Sports	Mountaineering, Hiking, Skiing, Snowshoeing, Climbing. Member of the Swiss Alpine Club (Diablerets section), formerly member of the Italian Alpine Club (Bergamo section);
Crafts	Sewing; I aim to entirely stop buying clothes as I learn new dress making techniques, including sportswear and the use of technical fabrics;
Reading	Any genre. I collect books and my library now counts nearly 300